Interannual middle-latitude atmosphere-ocean interactions

by

Jason C. Goodman

Submitted to the Department of Earth, Atmospheric, and Planetary Sciences
in partial fulfillment of the requirements for the degree of

Doctor of Philosophy

at the

MASSACHUSETTS INSTITUTE OF TECHNOLOGY

February 2001

Author .....
Department of Earth, Atmospheric, and Planetary Sciences
February 15, 2001

Certified by .....
John Marshall
Professor
Thesis Supervisor

Accepted by .....
Ronald Prinn
Department Head

Interannual middle-latitude atmosphere-ocean interactions

by

Jason C. Goodman

Submitted to the Department of Earth, Atmospheric, and Planetary Sciences
on February 15, 2001, in partial fulfillment of the
requirements for the degree of
Doctor of Philosophy

Abstract

This thesis discusses the interaction of atmosphere and ocean in midlatitudes on interannual and decadal timescales. We investigate the extent to which mutually-coupled atmosphere-ocean feedback can explain the observed coupled variability on these timescales, and look for preferred modes of atmospheric response to forcing by sea-surface temperature anomalies.

First, we formulate and study a very simple analytical model of the mutual interaction of the middle-latitude atmosphere and ocean. The model is found to support coupled modes in which oceanic baroclinic Rossby waves of decadal period grow through positive coupled feedback between the thermal forcing of the atmosphere induced by associated SST anomalies and the resulting windstress forcing of the ocean. Growth only occurs if the atmospheric response to thermal forcing is equivalent barotropic, with a particular phase relationship with the underlying SST anomalies. The dependence of the growth rate and structure of the modes on the nature of the assumed physics of air-sea interaction is explored, and their possible relation to observed phenomena discussed.

We then construct a numerical model with the same physics; this enables us to consider the effects of nontrivial boundary conditions and background flows within the model. We find that the finite fetch of a closed ocean basin reduces growth rate and can lead to decay. However, the coupled mode described above remains the least-damped, and is thus the pattern most easily energized by stochastic forcing. Using a non-uniform atmospheric background flow focuses perturbation energy into particular areas, so that the coupled mode's expression in the atmosphere becomes fixed in space, rather than propagating. This improves the mode's resemblance to observed patterns of variability, such as the North Atlantic Oscillation, which are generally stationary patterns which fluctuate in intensity.

The atmospheric component of the coupled mode exists in a balance between Rossby-wave propagation and vorticity advection. This is the same balance as the "neutral vectors" described by Marshall and Molteni (1993). Neutral vectors are the right singular vectors of the linearized atmospheric model's tendency matrix that have the smallest eigenvalues; they are also the patterns that exhibit the largest response to

forcing perturbations in the linear model. We explain how the coupled mode arises as the ocean excites atmospheric neutral vectors. Neutral vectors act as pattern-specific amplifiers of ocean SST anomalies.

We then proceed to study the neutral vectors of a quasigeostrophic model with realistic mean flow. We find a striking similarity between these patterns and the dominant patterns of variability observed in both the full nonlinear model and in the real world. We provide a mathematical explanation for this connection.

Investigation of the "optimal forcing patterns" - the left singular vectors - proves to be less fruitful. The neutral modes have equivalent barotropic vertical structure, but their optimal forcing patterns are baroclinic and seem to be associated with low-level heating. But the horizontal patterns of the forcing patterns are not robust, and are sensitive to the form of the inner product used in the SVD analysis. Additionally, applying "optimal" forcing patterns as perturbations to the full nonlinear model does not generate the response suggested by the linear model.

Thesis Supervisor: John Marshall
Title: Professor

Acknowledgments

I gratefully acknowledge the assistance of my advisor, John Marshall, for his collaboration and guidance in the work presented here. Without his continuing enthusiasm and optimism in the face of almost-insurmountable difficulties, this thesis would not have been possible. Since Chapter 2 is duplicated almost verbatim from our 1999 Journal of Climate paper, some of the text of that chapter was written by him.

My parents played a more important role in the creation of this thesis, though of course in a much broader sense. Without their unfailing encouragement and support of my education, I would never have entered graduate school in the first place.

I would like to thank the members of my thesis committee (Peter Stone, Alan Plumb, and Kerry Emanuel) for their insightful questions, useful suggestions, and their comments on and corrections to this thesis. Jochem Marotzke and Steve Meacham, as former members of my committee, provided similar assistance.

Many other scientists contributed useful comments and suggestions. These include Franco Molteni, Fabio d'Andrea, Arnaud Czaja, Claude Frankignoul, Grant Branstator, and Paul Van der Vaart. The advice of the anonymous reviewers of our Journal of Climate paper (Goodman and Marshall, 1999) was also useful.

Finally, I am endlessly grateful to my fiancée, Carolyn Smith, for her constant support and companionship, as well as for her patience during the completion of this thesis.

Contents

1 Introduction **11**

2 Analytical coupled model **17**

2.1 Model Formulation 18

2.1.1 Overview 18

2.1.2 Atmosphere 21

2.1.3 Ocean 25

2.1.4 Coupling mechanisms 27

2.1.5 Coupled equations 31

2.2 Dispersion relations and form of coupled modes 32

2.2.1 Plane wave solutions 33

2.2.2 Form and growth mechanism of coupled mode 38

2.3 Discussion of solutions: predictions and sensitivity 47

2.3.1 Frequency and scales 47

2.3.2 Coupling constants 48

2.3.3 Growth rates 51

2.3.4 Comparison with the Antarctic Circumpolar Wave 58

2.3.5 Sensitivity to parameters 61

2.3.6 Energetics of growth mechanism 62

2.4 Conclusion 64

3 Numerical coupled model **67**

3.1 Elaborations upon the analytical model 67

3.1.1 Model equations . . . 67
3.1.2 Discretization . . . 69
3.1.3 Time evolution and eigenspectrum . . . 71
3.1.4 Channel model . . . 72
3.1.5 Ocean basin . . . 76
3.1.6 Varicose atmospheric background flow . . . 79
3.1.7 Response to stochastic forcing . . . 80
3.1.8 Summary . . . 85
3.2 Neutral Vectors . . . 86
3.2.1 Coupled modes and neutral vectors . . . 88
3.2.2 Relevance of neutral vectors to coupled interaction . . . 89
3.3 Conclusions . . . 93

4 Neutral vectors in a 3-layer QG model 96
4.1 Molteni's 3-layer quasi-geostrophic model . . . 97
4.1.1 Computing neutral vectors . . . 100
4.2 Empirical orthogonal functions . . . 101
4.3 Neutral vectors . . . 103
4.3.1 Neutral vector structure . . . 104
4.3.2 Relationship between neutral vectors and EOFs . . . 109
4.4 Optimal forcing patterns . . . 113
4.4.1 Optimal forcing pattern structure . . . 113
4.4.2 Norm-sensitivity of optimal forcing patterns . . . 116
4.4.3 Response of the nonlinear model to "optimal" forcing . . . 118
4.5 Conclusions . . . 122

5 Summary and future projects 124
5.1 Summary . . . 124
5.2 Future work . . . 126

A Diffusion effects in the coupled model **130**

A.1 Changes to the GM99 model equations 131

A.2 Constraints on the values of the diffusion constants 133

A.3 Results 134

A.4 Conclusion 135

B EOFs and neutral vectors in restricted domains **136**

B.1 EOFs in restricted domains 136

B.2 Neutral vectors in restricted domains 140

B.3 Conclusion 143

List of Figures

1-1 The NAO pattern and its covarying SST anomaly. 13

2-1 Structure of the coupled model 21
2-2 Atmospheric response to thermal forcing (Shutts, 1987) 26
2-3 Diagram of entrainment process 30
2-4 Structure of coupled growing mode 40
2-5 Structure of damped SST-only mode 43
2-6 Generation of SST anomalies by advection of mean gradient 45
2-7 Contour plot of μ as a function of basic-state wind speed 49
2-8 Dependence of growth rate of coupled mode on wavelength 51
2-9 Frequency and growth rate of "heat flux mode" 54
2-10 As in figure 2-8(a,b), but with zero entrainment: $\gamma_e = 0$. 55
2-11 Dependence of growth rate on basic-state winds 57
2-12 Schematic diagram of Antarctic Circumpolar Wave 59

3-1 Snapshots and evolution of the numerical model (channel run) 74
3-2 Eigenvalues and eigenvectors of the model's tendency matrix (channel run) 75
3-3 Same as 3-2, but for a single ocean basin 6000 km wide 77
3-4 Basic-state streamfunction pattern used in the varicose background flow experiment. 80
3-5 Same as 3-1, but with varicose background flow 81
3-6 Same as 3-5, but with stochastic forcing. 83
3-7 EOFs of the stochastically-forced coupled model. 84

3-8 First three neutral vectors of model with varicose basic state 89
3-9 Projections of neutral vectors and optimal forcing patterns onto a forward model run. 91
3-10 Schematic representation of the mutually-coupled atmosphere-ocean hypothesis of interannual climate variability. 95

4-1 3-layer QG model mean climatology 99
4-2 EOFs of Molteni model 102
4-3 Neutral vector and optimal forcing pattern #1 105
4-4 Neutral vector and optimal forcing pattern #2 106
4-5 Neutral vector and optimal forcing pattern #3 107
4-6 Cross-correlations between EOFs and neutral vectors 108
4-7 Fractional variance explained by EOFs and neutral vectors 110
4-8 Neutral vector and optimal forcing pattern #1 for psi norm 115
4-9 Response of the nonlinear model to "optimal" forcing. 119

A-1 Dependence of coupled mode's growth rate on wavelength, diffusive model 134

B-1 Results of global and local EOF analyses on artificial data 139

List of Tables

2.1 Numeric parameter values 52

Chapter 1

Introduction

The existence of regionally-covarying "teleconnection" patterns in the atmosphere has been known for most of the past century (Walker & Bliss, 1932); Wallace & Gutzler (1981) provide an overview of the most prominent of these patterns. More recently, there has been a growing body of literature that documents the variability of these patterns on interannual and decadal timescales, and examines their covariance with oceanic fields.

One of these teleconnection patterns, the North Atlantic Oscillation, was identified by Walker & Bliss (1932), but has recently come to prominence through timeseries analysis conducted by Hurrell (1995) and others. Hurrell's NAO index is given by the normalized difference between sea-level pressure in Iceland and the Azores. This index captures the variability of the first EOF of monthly sea-level pressure changes over the North Atlantic (Cayan 1992a,b) – a dipole pattern with centers over the subpolar and the subtropical North Atlantic (see Figure 1-1). This pattern exhibits variability on all timescales, but has some interesting interannual behavior. This atmospheric pattern shows significant 1-year lag-correlations during the winter months, resulting in a reddened spectrum; this lag-correlation disappears in the summer. In light of the strong seasonal cycle, rapid fluctuation, and strong thermal damping of atmospheric anomalies, it is rather surprising that these anomalies persist from winter to winter. This has led many (see below) to propose a coupling between atmosphere and ocean to provide a long-term "memory" for the NAO pattern – but arguments to the contrary

(James & James 1989, discussed below) also exist.

Cayan (1992a,b), Deser & Blackmon (1993), and Sutton & Allen (1997) describe patterns covariant between atmosphere and ocean. A "tripole" pattern of sea surface temperature, with centers of action south of Greenland, west of the eastern U.S., and in the tropics, is found to covary with the NAO. (See Figure 1-1). Kushnir (1994) also discusses the structure of interannual atmospheric and SST variability in the Atlantic, and shows structural differences between interannual and interdecadal variability.

Responses to the NAO may extend deeper than the ocean mixed layer. Dickson *et al.* (1996), McCartney *et al.* (1997), and Curry & McCartney (1997) find coordinated changes in Labrador Sea Water thickness in the North Atlantic which appear to be connected with the state of the NAO.

Several authors have found evidence for enhanced interannual or decadal variability, or spectral peaks, in observations of mid-latitude variability patterns. Deser & Blackmon (1993) show an apparent enhancement of variability on timescales of about 12 years for an NAO-like atmospheric pattern and a covariant SST pattern. Hurrell's (1995) winter NAO index shows enhanced variability in the 6-10 year range. Latif *et al.* find a coupled mode with an NAO-like atmospheric expression and strong decadal variability in their ECHO-1 coupled model; the model shows a similar signal with longer period in the Pacific. Sutton & Allen (1997) claim to see a repetitive cycle of slow propagation of SST anomalies along the Gulf Stream. These SST anomalies covary with a dipolar atmospheric pattern, and a regular period of 12-14 years. It should be emphasized that many of these spectral peaks are uncomfortably near the level of statistical insignificance, and the observations of mutually coupled interaction on these timescales are a matter of debate (Bretherton & Battisti, 2000; Czaja & Mashall, 2000a). In newer work, Czaja & Marshall (2000b) find a coupled atmosphere-ocean pattern similar to but not identical to the NAO / SST tripole, which shows significantly enhanced variability in the 10-20 year band.

While most of the work on interannual midlatitude variability has been done in the northern hemisphere, interesting signals have been observed in the Southern Ocean. White & Peterson (1996) and Jacobs & Mitchell (1996) have observed an"Antarctic

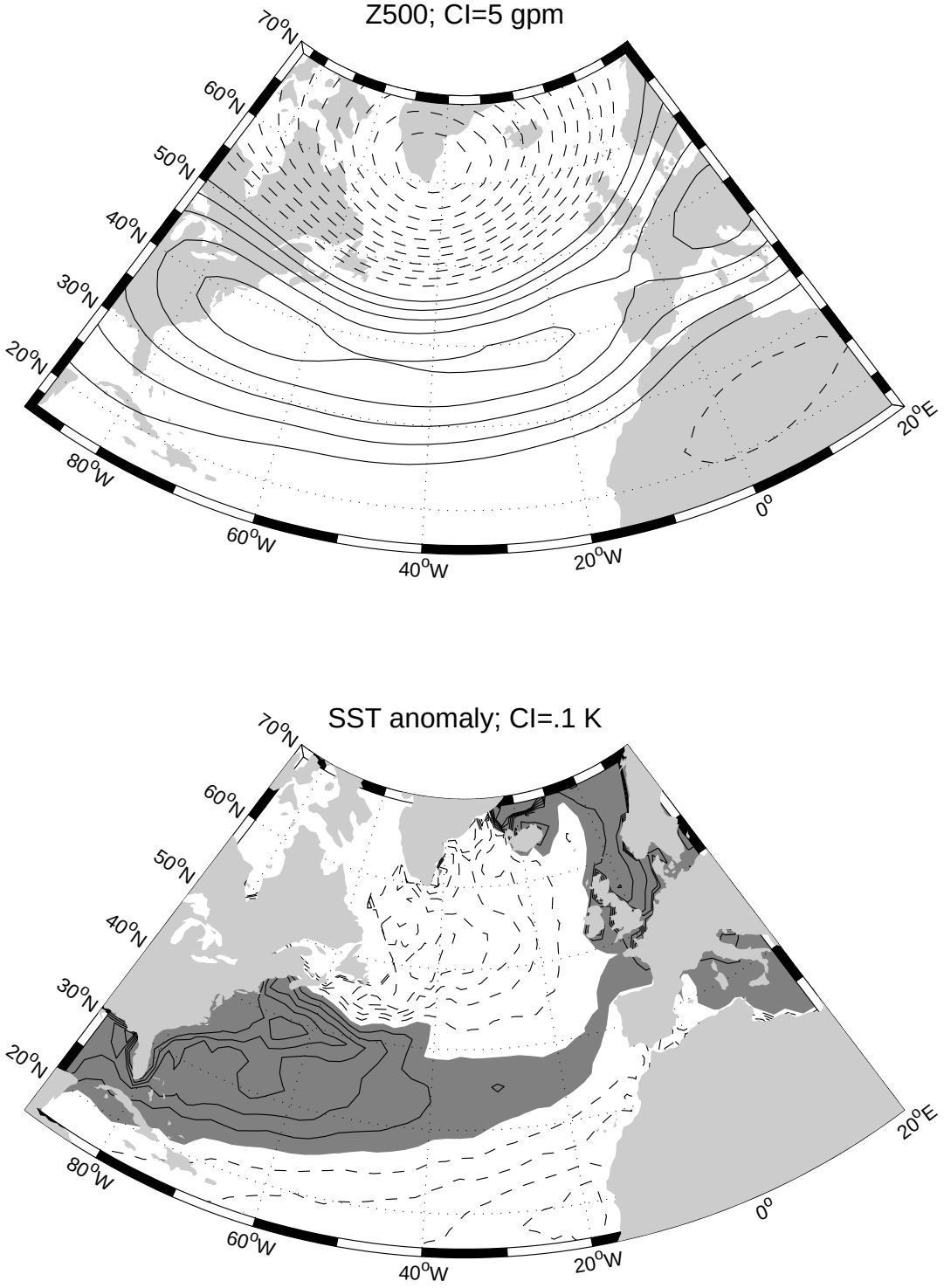

Figure 1-1: The dominant mode of Atlantic atmosphere/ocean variability. Data provided by A. Czaja. Top: Geopotential height anomaly (contour interval 5 gpm) at 500 mbar. Negative values dashed. Bottom: Covariant SST anomaly pattern. Contour interval 0.1 K, positive values shaded, negative values dashed.

Circumpolar Wave" (ACW), a wavenumber-2 pattern seen in atmospheric pressure, sea-surface height, and SST which propagates around Antarctica every 4-5 years. However, data in this region are sparse, and the available timeseries are rather short.

While observations of interannual variability in the midlatitude atmosphere and ocean are abundant, the underlying dynamical causes of this variability remain obscure. We do not yet know whether the dynamics are coupled or uncoupled, nor do we know the relative importance of the ocean and atmosphere on decadal time-scales. Does variability arise through internal instabilities in one component only, which communicates these changes to its passive partner, or does it arise through mutual interactions of the two systems? Useful review of these issues is given by Palmer (1996) and McCartney (1997). Frankignoul (1985) concisely reviews middle-latitude atmosphere-ocean interactions.

Many researchers suggest the atmosphere generates the climate variations on its own, and the ocean reacts passively to that stimulus. Some modeling studies (e.g., James & James, 1989) show that a model atmosphere is capable, in the presence of fixed surface boundary conditions (fixed ocean), of exhibiting long term persistent (climate) states, in clear contradiction to the usual assertion that the atmosphere has no memory longer than about one month. Atmospheric general circulation models, forced with temporally non-varying SSTs, display fluctuations that resemble the spatial structure of observed modes of variability such as the NAO (Barnett, 1985, Marshall & Molteni, 1993) but do not capture the reddening of observed spectra.

The idea that much of observed climate variability can be explained as the integral response of the slowly varying parts of the climate system to stochastic atmospheric variability was first proposed by Hasselmann (1976) and Frankignoul & Hasselmann (1977); see also Cayan (1992a,b), Battisti *et al.* (1995) and Hall & Manabe (1997). Frankignoul *et al.* (1996) have shown that decadal time-scales in a dynamical ocean can be generated through the response of oceanic baroclinic Rossby waves to stochastic wind stress forcing. Griffies & Tziperman (1995) attribute decadal fluctuations of the thermohaline circulation evident in coupled integrations to stochastic atmospheric forcing. But the purely stochastic model, in which the ocean responds to

stochastic atmospheric forcing without feedback, is inconsistent with the observed reddening of atmospheric spectra (see, for example, Deser & Blackmon; 1993), and with the observed lead-correlations between atmospheric and SST anomalies (Czaja & Frankignoul, 1999).

One possible mechanism which could account for a reddened atmospheric spectrum is that the ocean 'imprints' itself back on the atmosphere on longer time-scales. The atmospheric response could itself drive the ocean, resulting in an "actively coupled" mutual dynamic interaction between the fluids, or the feedback to the ocean could be unimportant, resulting in a "passively coupled" response. Passive coupling is a feature of the models studied by Saravanan & McWilliams (1997, 1998) and Weng & Neelin (1996). Latif & Barnett (1996) provide an example of active coupling: their model produces self-sustained decadal oscillations in the coupled atmosphere-ocean system. Rodwell *et al.* (1999) find that a large fraction of the variance of the NAO can be hindcast given knowledge of SST anomalies. This suggests a feedback of ocean onto atmosphere (of either an 'active' or 'passive' nature), but the utility and importance of this result is a matter of debate. (Bretherton & Battisti 2000, Czaja & Marshall, 2000a)

Several authors have published highly-simplified models which attempt to investigate coupled behavior from a theoretical point of view, isolating aspects of the physics of atmosphere-ocean coupling and demonstrating physical processes which can lead to coupled interaction. (Frankignoul *et al.* (1996), Cessi and Gallego (2000), Latif *et al.* (1996), Goodman and Marshall (1999), Marshall, Johnson, and Goodman (2000)) These studies invoke a variety of different and often incompatible mechanisms of air-sea transfer mechanisms atmospheric dynamics, but they share the idea that the propagation of oceanic baroclinic Rossby waves provide the "metronome" which regulates interannual-decadal oscillations. Such waves have decadal periods similar to the observed timescales of variability.

In the second chapter of this thesis, we present the work published in Goodman and Marshall (1999). We construct an analytical model of active coupling and study how a dynamical ocean in middle and high latitudes might actively couple to the

atmosphere. We formulate and analyze a simple coupled atmosphere-ocean model in which atmospheric planetary waves respond to SST. SST depends on ocean circulation, which is in turn driven by the wind-stress, leading to full-circle coupled interaction. Growing modes of decadal period are found; we study their form and dependence on the coupling physics assumed.

In Chapter 3, we elaborate the simple analytical model to study the behavior of the coupled mode in a restricted domain, and with more complicated basic states. This is achieved by developing a numerical model with the same physics as described in the previous chapter. This work points strongly to the importance of nearly-resonant atmospheric patterns, dubbed "neutral vectors" by Marshall & Molteni (1993), in setting the structure of the coupled mode.

In the fourth chapter, we take a closer look at these neutral vectors. First, we investigate the relationship between neutral vectors and the EOFs of a purely atmospheric model. Having established a connection between these patterns, we then attempt to identify the forcing patterns which will most strongly excite the neutral vectors. If the ocean SST projects strongly onto these optimal forcing patterns, a strong atmospheric response is likely, and an actively coupled atmosphere-ocean interaction is possible. One goal of this chapter is to answer the question, "what thermal forcing pattern generates the NAO pattern?"

Chapter 2

An analytical model of decadal middle-latitude atmosphere-ocean coupled modes

In this chapter, we discuss the analytical model of atmosphere-ocean interaction published by John Marshall and myself in 1999[1]. The goal of this chapter is to investigate a mechanism by which atmosphere and ocean can interact in midlatitudes to produce interannual variability. We analyze the model solutions, and compare the model's variability with observed patterns, especially the North Atlantic Oscillation.

In Section 2.1, the coupled model is formulated. In Section 2.2, the dispersion relation and structure of the coupled modes is derived. In Section 2.3, we discuss these solutions in the context of observations of observed phenomena such as the Antarctic Circumpolar Wave and the North Atlantic Oscillation, and their parameter

sensitivity. Conclusions are presented in Section 2.4.

2.1 Model Formulation

2.1.1 Overview

Our model comprises a quasi-geostrophic atmosphere overlying a quasi-geostrophic ocean, characterized by their respective potential vorticities (QGPV) and streamfunction distributions and governed by prognostic QGPV equations on a beta-plane.

The atmosphere, imagined to be bounded above by a lid and below by the ocean, is governed by the equation:

$$\frac{D}{Dt}q_a = f_o\frac{\partial}{\partial z}\left(\frac{Q_a}{\frac{\partial}{\partial z}\overline{\theta_a}}\right) - \epsilon\nabla^2\psi_{as} \qquad \text{ATMOSPHERE} \tag{2.1}$$

Here $\frac{D}{Dt}$ is the Lagrangian derivative and q_a is the quasi-geostrophic potential vorticity:

$$q_a = \nabla^2\psi_a + \beta y + f_o^2\frac{\partial}{\partial z}\left(\frac{1}{N_a^2}\frac{\partial}{\partial z}\psi_a\right)$$

expressed in terms of the atmospheric streamfunction ψ_a. f_o is a reference value of the Coriolis parameter f, the meridional gradient of f is β, $N_a^2 = \frac{1}{\theta_{a0}}\frac{\partial}{\partial z}\overline{\theta_a}$ is the atmospheric Brunt-Väisälä buoyancy frequency, θ_a the atmospheric potential temperature with θ_{a0} a typical value, and Q_a is the diabatic heating rate of the atmosphere defined by:

$$\frac{D}{Dt}\theta_a = Q_a \tag{2.2}$$

In (2.1), $\epsilon\nabla^2\psi_{as}$ represents frictional sinks of vorticity associated with Ekman layers at the surface with ϵ^{-1} a frictional spin-down time.

We suppose that a radiative-convective equilibrium temperature, θ_a^*, controls the thermal forcing of the atmosphere thus:

$$Q_a = -\gamma_a(\theta_a - \theta_a^*) \tag{2.3}$$

Here γ_a^{-1} is a time-scale set by the radiative-convective process; θ_a^* is a radiative-convective temperature profile to which θ_a relaxes, which is assumed to be a function of sea-surface temperature thus:

$$\theta_a^* = \theta_a^*(\mathrm{SST}) \tag{2.4}$$

The form, (2.3) and (2.4), makes sense as a simple and physically plausible representation of convective heating of the troposphere, permitting the heating field to be a function of the state of both the atmosphere and the ocean. That heating will initiate a dynamical response of the atmosphere and change the winds that blow over the ocean.

The equations governing the ocean are:

$$\frac{D}{Dt}q_o = f_o\frac{\partial}{\partial z}\left(\frac{Q_o}{\frac{\partial}{\partial z}\overline{\theta_o}}\right) + \frac{1}{\rho_o}\hat{k}\cdot\nabla\times\frac{\partial}{\partial z}\tau \qquad \text{OCEAN} \tag{2.5}$$

where q_o is the oceanic QGPV:

$$q_o = \nabla^2\psi_o + \beta y + f_o^2\frac{\partial}{\partial z}\left(\frac{1}{N_o^2}\frac{\partial}{\partial z}\psi_o\right)$$

ψ_o is an oceanic streamfunction, N_o^2 is an oceanic Brunt-Väisälä frequency, Q_o is the diabatic heating of the interior of the ocean and τ is the mechanical stress supplied by the surface wind. The stress at the ocean's surface is a function of the velocity of the wind at the surface:

$$\tau_s = \tau_s(\psi_s) \tag{2.6}$$

The evolution of the oceanic mixed-layer temperature, which we assume is synonymous with sea-surface temperature, is

$$\left(\frac{\partial}{\partial t} + v\cdot\nabla\right)\mathrm{SST} = Q_o \qquad \text{SEA SURFACE TEMPERATURE} \tag{2.7}$$

Here the horizontal velocity in the mixed layer is v, the sum of an Ekman and geostrophic components ($v = v_{\mathrm{ek}} + v_g$), and Q_o is the diabatic heating of the mixed

layer induced by air-sea interaction and entrainment fluxes through the mixed-layer base. There is no vertical advection in (2.7) because the mixed layer is assumed to be vertically homogeneous.

Note that:

1. (2.1) and (2.2) are the starting point of analytical studies of atmospheric planetary waves dating back to Charney and Eliassen (1949) and Smagorinski (1953).

2. If $v = 0$, then (2.7) reduces to a 'slab ocean', which responds on timescales of several months (primarily via surface heat exchange and entrainment), depending on the depth of the 'slab' - see, eg. Hasselman (1977); Frankignoul and Hasselman (1977). On decadal time-scales, however, advective processes may be important and SST changes may be dominated by gyre dynamics and subduction processes: see Hall and Manabe (1997).

3. If the wind-curl is assumed to be a stochastic process and $Q_o = 0$ in (2.5), then it reduces to the ocean model analyzed by Frankignoul *et al.* (1996) in their study of the response of the ocean to stochastic atmospheric forcing.

Clearly, (2.1) through (2.7) are highly simplified representations of the respective fluids and their interaction. But the philosophy of our approach is to build our intuition about the coupled problem in stages, by first fitting together simple pieces, and then increasing the complexity of the component parts and their coupling. Heating of the atmosphere depends, through (2.3) and (2.4), on the state of the ocean which, in turn, depends on its forcing from the atmosphere via (2.6). We shall now go on to study whether the above system supports coupled modes. Their existence will depend on the form assumed for (2.3), (2.4), (2.6) and (2.7) i.e. on the nature of the boundary layers of the two fluids and the manner in which they are assumed to interact with one-another and the 'free' atmosphere/ocean above/below. To make analytical progress our representations will, of necessity, be simple, but they are motivated by sound physical principles.

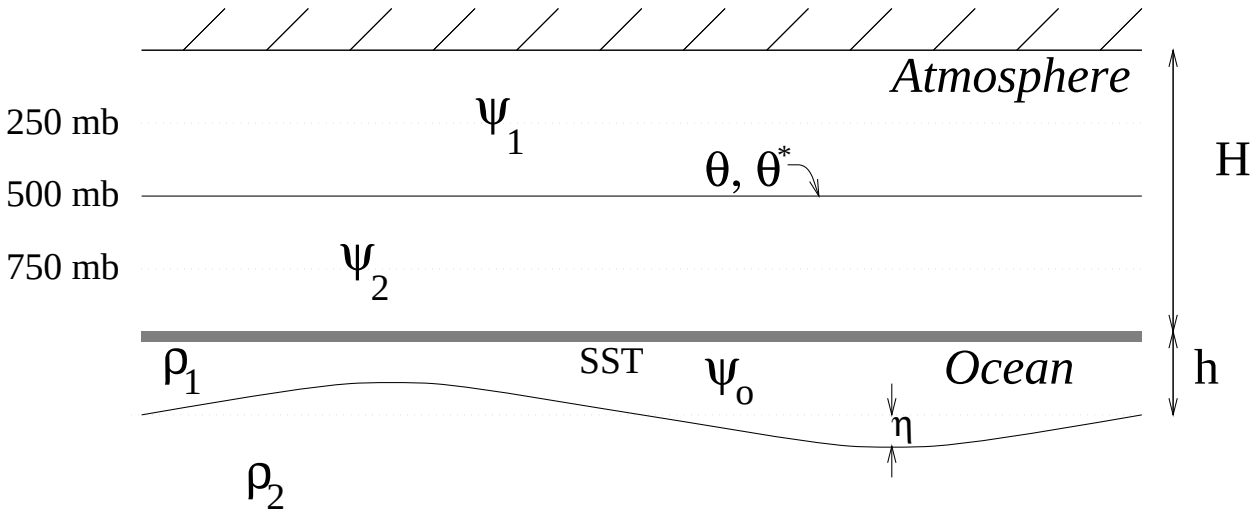

Figure 2-1: Vertical structure of the coupled model defining the key variables of the coupled ocean-atmosphere system

2.1.2 Atmosphere

We will adopt the simplest representation of the equation set described in Section 2.1.1 which captures the essential dynamics — a two-level quasi-geostrophic atmosphere, sketched schematically in Figure 2-1. This model is extremely simple and limited in scope (particularly in its ability to resolve the vertical structure of atmospheric heating) but it has been comprehensively studied and allows us to obtain analytical solutions.[2] Furthermore it is supposed that the atmosphere responds rapidly to thermal forcing associated with SST anomalies when compared to interannual-to-decadal time-scales, and so on these time-scales the atmosphere is assumed to be in steady state. We therefore neglect the local time-derivative terms in the prognostic equations for the atmosphere, thus slaving it to SST. No attempt is made to represent the rectified affects of high-frequency components on the steady circulation (the interaction of synoptic eddies with the planetary-wave pattern, for example). We recognize that this is an important process in nature, but one which is difficult to address in a simple model.

[2]Lindzen *et al.* (1968) have argued that spurious vertical trapping of waves by the "rigid lid" of this model may lead to false resonances. However, Panetta *et al.* (1987) show that for supercritical shear (as here), this model's response to forcing is actually quite accurate.

For simplicity we also set $\epsilon = 0$ in (2.1), thus obtaining the following the two-level, steady-state quasi-geostrophic equations for the atmosphere (using the nomenclature of Shutts, 1987)

$$J(\psi_2, q_2) = \frac{gHS}{2fL_a^2}; \qquad J(\psi_1, q_1) = -\frac{gHS}{2fL_a^2} \tag{2.8}$$

where S is the diabatic forcing, given by $S = \frac{Q_a}{\theta_{a0}}$, θ_{a0} is a typical atmospheric temperature, and

$$q_1 = \nabla^2\psi_1 - \frac{1}{L_a^2}(\psi_1 - \psi_2) + \beta y \qquad q_2 = \nabla^2\psi_2 + \frac{1}{L_a^2}(\psi_1 - \psi_2) + \beta y$$

are the QGPVs at each level with $L_a^2 = \frac{N_a^2 H^2}{4f^2}$ the square of the atmospheric baroclinic Rossby radius.

Taking the sum and difference of ψ and q to form the barotropic and baroclinic streamfunction and PV, and using the notation $\widehat{(:)} = (:)_2 + (:)_1$; $\widetilde{(:)} = (:)_1 - (:)_2$, equations for the barotropic and baroclinic PV can be written thus:

$$J(\widehat{\psi}, \widehat{q}) + J(\widetilde{\psi}, \widetilde{q}) = \quad 0 \qquad \text{(barotropic)} \tag{2.9}$$

$$J(\widetilde{\psi}, \widehat{q}) + J(\widehat{\psi}, \widetilde{q}) = \quad -\tfrac{2gHS}{fL_a^2} \qquad \text{(baroclinic)} \tag{2.10}$$

where

$$\widehat{q} = q_2 + q_1 = \nabla^2\widehat{\psi} + 2\beta y \qquad \widetilde{q} = q_1 - q_2 = \nabla^2\widetilde{\psi} - \frac{2}{L_a^2}\widetilde{\psi}$$

Planetary β appears only in the barotropic PV; the stretching term appears only in the baroclinic PV.

It should be noted that diabatic heating only directly forces the baroclinic PV equation. However, because the baroclinic fields drive the barotropic PV equation through (2.9), the atmosphere does not respond purely baroclinically. Thermal forcing can yield an 'equivalent barotropic' response (anomalies of constant sign throughout the atmosphere) and need not always result in first-baroclinic mode behavior. This turns out to be crucial to the existence of coupled modes in our simple model — see Section 2.2.

2.1.2.1 Linearized model

We linearize the atmospheric equations around the simplest realistic state: uniform zonal winds of differing magnitudes at levels 1 and 2. Again, defining barotropic and baroclinic components: $\widehat{U} = U_1 + U_2$; $\widetilde{U} = U_1 - U_2$ we have:

$$\widehat{\psi} = \widehat{\psi}' - \widehat{U}y \qquad \widetilde{\psi} = \widetilde{\psi}' - \widetilde{U}y$$

Substituting in to (2.9) and (2.10) and neglecting quadratic terms in the perturbation quantities, we have (after dropping the primes to simplify notation)

Barotropic PV equation:

$$\widehat{U}\frac{\partial}{\partial x}(\nabla^2\widehat{\psi} + \widehat{\beta}y) + \widehat{\beta}\frac{\partial}{\partial x}\widehat{\psi} + \widetilde{U}\frac{\partial}{\partial x}(\nabla^2\widetilde{\psi} + \widetilde{\beta}y) = 0 \tag{2.11}$$

Baroclinic PV equation:

$$\widetilde{U}\frac{\partial}{\partial x}(\nabla^2\widehat{\psi} + \widehat{\beta}y) + \widetilde{\beta}\frac{\partial}{\partial x}\widehat{\psi} + \widehat{U}\frac{\partial}{\partial x}(\nabla^2\widetilde{\psi} - \frac{2}{L_a^2}\widetilde{\psi} + \widetilde{\beta}y) + \widehat{\beta}\frac{\partial}{\partial x}\widetilde{\psi} = -\frac{2gHS}{fL_a^2} \tag{2.12}$$

where

$$\widehat{\beta} = 2\beta \tag{2.13}$$

enters as a beta-effect term in the barotropic PV [3] and

$$\widetilde{\beta} = \frac{2}{L_a^2}\widetilde{U} \tag{2.14}$$

plays the same role in the baroclinic PV. Note how two different mechanisms provide the same effect: $\widehat{\beta}$ arises from changes in planetary vorticity; $\widetilde{\beta}$ arises from vortex-stretching when fluid moves against the sloping interface generated by the zonal mean wind shear $\widetilde{U}$.

Following Shutts (1987), we specify a Newtonian relaxation of the temperature perturbation (at level $1\frac{1}{2}$) toward some equilibrium temperature anomaly $\delta\phi^*$ ($\phi =$

[3] The factor of 2 arises because we have defined the barotropic fields as vertical sums rather than averages.

$\ln\theta$; $\delta\phi = \frac{\delta\theta}{\theta_{a0}}$) on a radiative-convective equilibrium timescale $1/\gamma_a$:

$$S = -\gamma_a(\delta\phi - \delta\phi^*) = -\gamma_a\left(\frac{2f}{gH}\widetilde{\psi} - \frac{\theta_a^*}{\theta_{a0}}\right) \tag{2.15}$$

where we have expressed the temperature in the quasi-geostrophic model in terms of the baroclinic streamfunction by using $\delta\phi = \frac{2f}{gH}\widetilde{\psi}$, employing the thermal wind relation.

Inserting (2.15) into (2.12), we have

$$\widetilde{U}\frac{\partial}{\partial x}(\nabla^2\widehat{\psi}+\widehat{\beta}y)+\widetilde{\beta}\frac{\partial}{\partial x}\widehat{\psi}+\widehat{U}\frac{\partial}{\partial x}(\nabla^2\widetilde{\psi}-\frac{2}{L_a^2}\widetilde{\psi}+\widetilde{\beta}y)+\widehat{\beta}\frac{\partial}{\partial x}\widetilde{\psi} = \frac{4\gamma_a}{L_a^2}\left(\widetilde{\psi} - \frac{1}{r_a}\theta_a^*\right) \tag{2.16}$$

where

$$r_a \equiv \frac{2f\theta_{a0}}{gH}$$

has units of (temperature/streamfunction), and converts atmospheric temperature to baroclinic streamfunction through the thermal wind relation. Thus thermal forcing of the atmosphere drives it toward an equilibration streamfunction $\widetilde{\psi}^* = \theta_a^*/r_a$.

2.1.2.2 Thermally forced and equilibrated responses

The properties of the above system for a specified θ_a^* are described in detail by Shutts (1987) and Marshall and So (1990); see also Frankignoul (1985). Because of the form chosen for the forcing function (2.15), the driving of the atmosphere by diabatic heating depends on the response of the atmosphere to that heating. In more conventional forcing problems, S is prescribed as a fixed, and unchanging, function of space. Then the thermal response of the atmosphere is always 90° out of phase with the heating field (note the odd number of derivatives on the left side of (2.16), so that if S varies sinusoidally the response will vary co-sinusoidally), either up-stream or downstream depending on the strength of the wind relative to the free Rossby wave speed. Indeed in Figure 2-2a, in which the zonal winds are chosen to be considerably stronger than the free Rossby wave speed, we see lows at the surface, downstream of the warming and the vertical structure of the atmospheric response is baroclinic, with highs

above lows and *vice-versa*. This is the classical picture of direct thermal forcing of the atmosphere. However, Shutts (1987) shows that 'equilibration' can occur at the scale of free, stationary Rossby waves if the forcing is assumed to be a function of the atmosphere's response as in (2.3). At equilibration the left and right sides of (2.16) vanish independently. In this case (see Figure 2-2b), on a scale close to that at which Rossby waves are stationary with respect to the ground, the response is 'equivalent barotropic', with highs directly over warm θ_a^* and lows over cold θ_a^*. At this resonance scale, the response of the atmosphere is not infinite, however. Rather the diabatic heating rates become vanishingly small (equilibration occurs) as $\theta_a \rightarrow \theta_a^*$.

2.1.3 Ocean

We adopt quasi-geostrophic dynamics in a "1 1/2-layer" ocean, with a moving upper layer and a very deep lower layer which remains at rest; there is a a rigid lid at the surface (Pedlosky, 1987). Neglecting thermal PV sources ($Q_o = 0$ in (2.5)), the potential vorticity in the upper layer of ocean evolves according to (see Figure 2-1)

$$\frac{D}{Dt} q_o = \nabla \times \frac{\tau}{\rho_{o0} h}$$

where

$$q_o = \nabla^2 \psi_o - \frac{1}{L_o^2} \psi_o + \beta y$$

Here ψ_o is the oceanic streamfunction in the upper layer, $L_o^2 \equiv \frac{gh\Delta\rho/\rho_{o0}}{f^2}$ is the square of the oceanic baroclinic Rossby radius of deformation, with ρ_{o0} a constant reference value of density and $\Delta\rho$ the density difference between the two layers. Linearizing about a state of rest we have:

$$\frac{\partial}{\partial t} \left(\nabla^2 \psi_o - \frac{1}{L_o^2} \psi_o \right) + \beta \frac{\partial}{\partial x} \psi_o = \frac{1}{\rho_{o0}} \nabla \times \frac{\tau}{h}$$

We are interested in motions with spatial extents (L) of thousands of km. The Rossby radius in the ocean (L_o) is ∼50 km, so we may make the long-wave approximation and neglect the relative vorticity contribution to the PV, giving our final

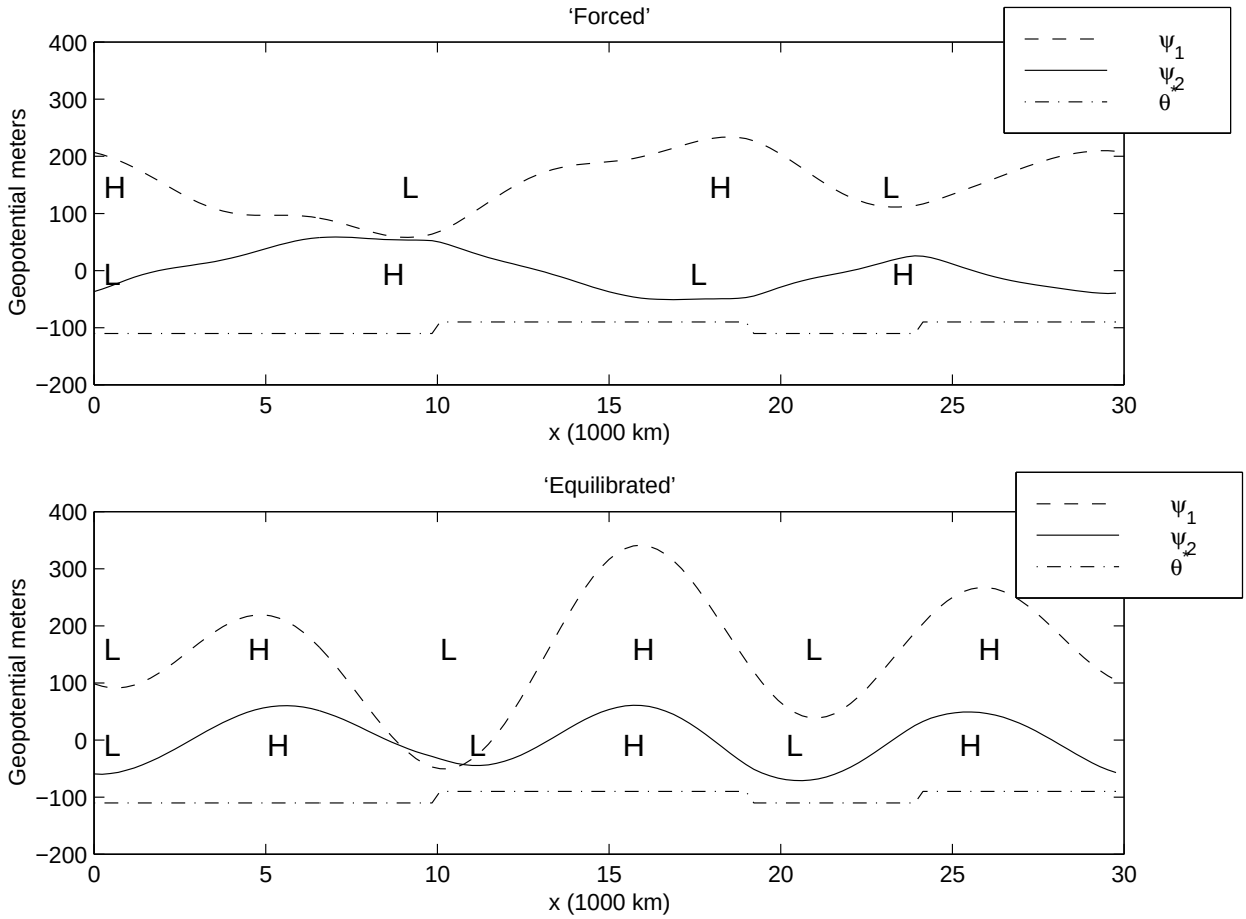

Figure 2-2: Steady-state atmospheric response to thermal forcing (reproduced from Shutts, 1987). Dashed curves: upper-level height anomaly, offset 150 gpm. Solid curves: lower-level height anomaly. Dash-dotted curve: equilibration temperature anomaly θ_a^*, (amplitude 10° C). Shutts' θ_a^* profile is chosen to broadly represent land-ocean differences in the wintertime northern hemisphere: θ_a^* is higher over oceans than land. a: Directly-forced response of atmospheric model to thermal forcing, with ($U_1 = 10$ m s^{-1}, $U_2 = 5$ m s^{-1}). For the dominant wavenumber 3, $\mu = +1/3$ from (2.32) and $\frac{\nu}{\Gamma} = 2.7$, from (2.33) and (2.34): the response is baroclinic and strongly phase-shifted. b: Equilibrated response, with ($U_1 = 20$ m s^{-1}, $U_2 = 7$ m s^{-1}). For wavenumber 3, $\mu = -3$, $\frac{\nu}{\Gamma} = .5$. Response is barotropic with ridges over warm θ_a^* and troughs over cold θ_a^*; the phase shift is small.

equation for the dynamic ocean:

$$-\frac{1}{L_o^2}\frac{\partial}{\partial t}\psi_o + \beta\frac{\partial}{\partial x}\psi_o = \frac{1}{\rho_{o0}}\nabla\times\frac{\tau}{h} \tag{2.17}$$

2.1.4 Coupling mechanisms

2.1.4.1 Windstress

With our simplified representations of atmosphere and ocean defined, we now specify the mutual forcing between them. The model ocean's circulation is forced by the stress generated by the surface wind field. We suppose that the wind-stress perturbation is proportional to the surface wind velocity perturbation, and set

$$\frac{1}{\rho_{o0}}\nabla\times\frac{\tau}{h} = \alpha\nabla^2\psi_s \tag{2.18}$$

Here $\psi_s = \psi_2 + 1/2(\psi_2 - \psi_1) = (1/2)\widehat{\psi} - \widetilde{\psi}$ is the atmospheric streamfunction extrapolated to the surface. The numerical values of the constant of proportionality, α, which depends on the air-sea drag coefficient, will be considered in Section 2.3.2.

2.1.4.2 Thermal Forcing

As in (2.4), we suppose that the atmosphere equilibrates to a temperature set by the sea surface. For simplicity, we set the equilibration temperature anomaly equal to SST′:

$$\theta_a^* = \mathrm{SST}' \tag{2.19}$$

How shall we determine the sea-surface temperature? Following Frankignoul (1985), we begin with the following equation for the evolution of mixed-layer temperature anomalies (assumed synonymous with SST):

$$h_{\mathrm{mix}}\frac{\partial}{\partial t}\mathrm{SST}' = -\frac{\lambda_o}{\rho C_p}(\mathrm{SST}' - \theta_a') - h_{\mathrm{mix}}\vec{u'}\cdot\nabla\overline{\mathrm{SST}} - w_e(\mathrm{SST}' - \theta_{\mathrm{sub}}) \tag{2.20}$$

where h_{mix} is the mixed-layer depth, SST' is the sea surface temperature anomaly,

θ'_a is the surface air temperature, λ_o is the linearized coefficient of combined latent, sensible, and longwave heat flux, u' is the anomaly in current in the mixed layer, $\nabla\overline{\mathrm{SST}}$ is the mean SST gradient, w_e is the entrainment velocity at the base of the mixed layer, and θ_{sub} is the temperature of the thermal anomaly being entrained.

If the θ'_a induced by the SST anomaly does not exceed the SST anomaly itself (a reasonable assumption on interannual and longer timescales) then the terms in our SST equation have the following magnitudes:

$$\sigma \sim \frac{\lambda_o}{C_o} + U\frac{\nabla\overline{\mathrm{SST}}}{\mathrm{SST}'} + \frac{w_e}{h_{\mathrm{mix}}}$$

where σ is the frequency at which SST is changing, $C_o = \rho c_p h_{\mathrm{mix}}$ is the heat capacity of the mixed layer of depth h_{mix}, and U is a measure of the strength of the current anomaly.

On interannual/decadal timescales $\sigma \sim \frac{2\pi}{10\ \mathrm{yr}} \sim 2 \cdot 10^{-8}\mathrm{s}^{-1}$. Estimates of the atmospheric heat flux feedback, λ_o, are given in Frankignoul *et al.* (1997) and Barsugli & Battisti (1997) and suggest a value of $\lambda_o \sim 20$ W m^{-2}K^{-1}. The heat capacity of a mixed layer of depth 100 m is $C_o \sim 4 \cdot 10^8$ J m^{-2}K^{-1} and so $\lambda_o/C_o \sim 5 \cdot 10^{-8}$ s^{-1}, of the same order as σ. In the advection term, a circulation anomaly associated with a 1° SST anomaly might be 2 cm/s, so given a 10° /3000 km mean meridional SST gradient, the advection term is $\sim 7 \cdot 10^{-8}$ s^{-1}. Finally, consider the entrainment term. During the summer w_e is close to zero, but w_e is large during the rapid deepening of the mixed layer in the winter. If the mixed-layer deepens to 200m during the six winter months (its thickness h averaging 100m over this period) then $w_e/h_{\mathrm{mix}} \sim \frac{1}{100}\frac{200}{.5\ \mathrm{yr}} = 1.3 \cdot 10^{-7}$ s^{-1}. The observed annual mean is roughly $7 \cdot 10^{-8}$ s^{-1} over most of the mid-latitude oceans, being zero during summer restratification and large during winter (Frankignoul, 1985).[4]

Our scaling suggests that each of the terms in the SST equation plays a non-negligible role on decadal timescales; other dynamics may be more relevant on shorter

[4]Note that w_e represents the downward velocity of the entraining base of the mixed layer through the underlying ocean: it is *not* related to the large-scale upwelling of fluid associated with the thermohaline overturning.

timescales. Thus, retaining all terms and defining the air-sea flux timescale $\gamma_o = \lambda_o/C_o$ and the entrainment timescale $\gamma_e = w_e/h_{\rm mix}$, our SST equation can be written:

$$\frac{\partial}{\partial t}\mathrm{SST}' = -\gamma_o(\mathrm{SST}' - \theta'_a) - \vec{u'} \cdot \nabla\overline{\mathrm{SST}} - \gamma_e(\mathrm{SST}' - \theta'_{\rm sub}) \tag{2.21}$$

We see that the mixed-layer temperature anomaly in our model is driven towards that of the atmosphere by surface fluxes, is driven towards that of the sub-surface thermal anomaly by the entrainment process, and is warmed and cooled by the advection of mean meridional SST gradient by ocean currents generated by a perturbed thermocline (see Figure 2-3). The longevity of the properties of the subsurface ocean is communicated to the SST by the entrainment and advection processes, providing memory from one year to the next.

Before going on it should be mentioned that the idea of entrainment-forcing of SST anomalies resembles that which is often employed in studies of equatorial coupled dynamics in which SST depends on the temperature of upwelled fluid — see Cane *et al.* (1990); Neelin *et al.* (1994). However, in the present context, there are some differences of interpretation. Here we interpret the relaxation term in (2.21) as representing the coupling of SST anomalies to deep thermal anomalies which are re-exposed to the surface every winter.

We now assume that $\theta'_{\rm sub}$ evolves via adiabatic undulation of isopycnal surfaces underlying the mixed layer: where the isopycnals are perturbed upward, cold water is brought toward the surface, lowering $\theta'_{\rm sub}$ (and thus SST), and *vice-versa* (see Figure 2-3):

$$\frac{\partial}{\partial t}\theta'_{\rm sub} + w\frac{\partial}{\partial z}\overline{\theta_o} = 0$$

where w is the vertical velocity and $\frac{\partial}{\partial z}\overline{\theta_o}$ is a measure of the stratification of the upper ocean. Setting $w = \frac{\partial \eta}{\partial t}$ and integrating both sides with respect to time, the deep thermal anomaly is

$$\theta'_{\rm sub} = -\eta\frac{\partial}{\partial z}\overline{\theta_o} = \eta\frac{N_o^2}{\varepsilon g} = \frac{1}{g\varepsilon}\frac{f}{h}\psi_o$$

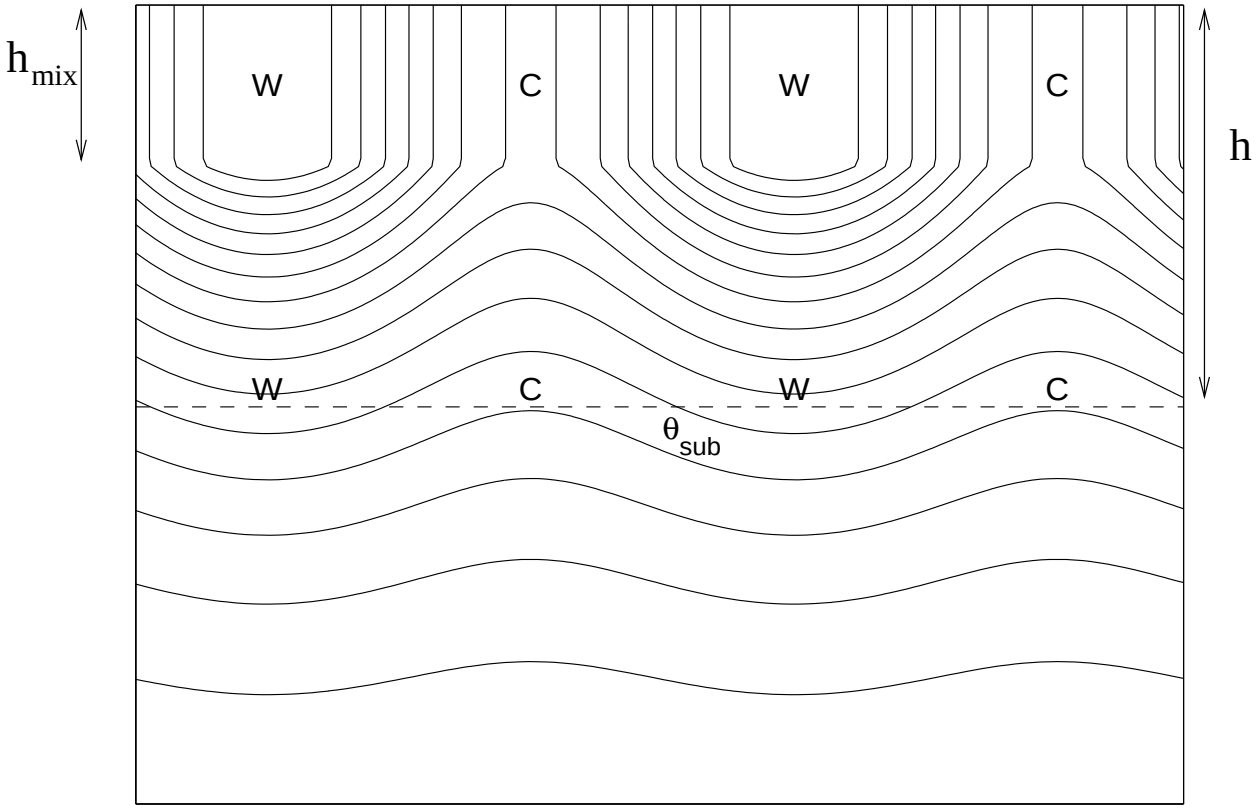

Figure 2-3: Schematic diagram showing the deepening of a mixed layer into subsurface thermal anomalies associated with an undulating thermocline. Note the resulting SST anomalies.

where η is a measure of the vertical excursion of isotherms, $N_o^2 = -\frac{g}{\rho_{o0}}\frac{\partial}{\partial z}\overline{\rho}$ is the Brunt-Väisälä frequency and $\varepsilon \equiv -\frac{1}{\rho_{o0}}\frac{\partial\overline{\rho}}{\partial\overline{\theta}}$ is the ratio of density change to temperature change. (If there are no salinity variations, ε is the coefficient of thermal expansion of water.) In the above η has been related to the baroclinic streamfunction via the thermal wind relation: $\eta = \frac{f}{hN_o^2}\psi_o$.

Since $v' = \frac{\partial}{\partial x}\psi_o$ in (2.21) and noting that $\theta_a' = r_a\widetilde{\psi}$, we can now write the evolution equation for SST in terms of the oceanic streamfunction and the atmospheric baroclinic streamfunction:

$$\frac{\partial}{\partial t}\mathrm{SST}' = -\gamma_o(\mathrm{SST}' - r_a\widetilde{\psi}) + ar_o\frac{\partial}{\partial x}\psi_o - \gamma_e(\mathrm{SST}' - r_o\psi_o) \tag{2.22}$$

where

$$r_o \equiv \frac{f}{g\varepsilon h} \qquad a \equiv -\frac{1}{r_o}\frac{\partial}{\partial y}\overline{\mathrm{SST}} = -\frac{g\varepsilon h}{f}\frac{\partial}{\partial y}\overline{\mathrm{SST}}$$

The parameter r_o is a scaling constant between an oceanic streamfunction anomaly and the temperature associated with it via thermal wind, analogous to r_a. The parameter a, which is generally positive, measures the strength of horizontal advection in the SST equation: for an SST anomaly of lateral scale L, advection dominates over entrainment when $a/L \gg \gamma_e$.

2.1.5 Coupled equations

finally we may now write a set of four coupled equations for the dynamic ocean, SST, and barotropic and baroclinic atmospheric components in closed form, by inserting the forcing relations (2.18, 2.15, and 2.19) into equations (2.17), (2.22), (2.11), and (2.16) to yield:

Dynamic Ocean:

$$-\frac{1}{L_o^2}\frac{\partial}{\partial t}\psi_o + \beta\frac{\partial}{\partial x}\psi_o = \alpha\nabla^2(1/2\widehat{\psi} - \widetilde{\psi}) \tag{2.23}$$

SST:

$$\frac{\partial}{\partial t}\mathrm{SST} = -\gamma_o(\mathrm{SST} - r_a\widetilde{\psi}) + ar_o\frac{\partial}{\partial x}\psi_o - \gamma_e(\mathrm{SST} - r_o\psi_o) \tag{2.24}$$

Barotropic Atmosphere:

$$\widehat{U}\frac{\partial}{\partial x}\nabla^2\widehat{\psi} + \widehat{\beta}\frac{\partial}{\partial x}\widehat{\psi} + \widetilde{U}\frac{\partial}{\partial x}\nabla^2\widetilde{\psi} = 0 \tag{2.25}$$

Baroclinic Atmosphere:

$$\widetilde{U}\frac{\partial}{\partial x}\nabla^2\widehat{\psi} + \widetilde{\beta}\frac{\partial}{\partial x}\widehat{\psi} + \widehat{U}\frac{\partial}{\partial x}(\nabla^2\widetilde{\psi} - \frac{2}{L_a^2}\widetilde{\psi}) + \widehat{\beta}\frac{\partial}{\partial x}\widetilde{\psi} = \frac{4}{L_a^2}\gamma_a(\widetilde{\psi} - \frac{1}{r_a}\mathrm{SST}') \tag{2.26}$$

where $\widehat{\beta}$ and $\widetilde{\beta}$ are defined in (2.13) and (2.14).

Before going on to study the properties of this coupled system it should be mentioned that the above model has some similarities with the early study of White & Barnett (1972), a paper which we found of great interest. However, they use a much simpler SST equation, and look for coupled growing modes on monthly time-scales and identify waves with periods near the *barotropic* ocean Rossby wave period. Their ocean model cannot capture the slow baroclinic evolution of the ocean. Moreover the atmosphere assumed by White and Barnett neglects mean zonal winds, is linearized about a state of rest and its thermal forcing is represented in an unusual way which is unclear to us. In the present model we shall see that the ability of the atmosphere to equilibrate to thermal forcing is vital to the presence of coupled modes, an aspect which is absent in the study of White and Barnett (1972). Our coupled system also has some aspects in common with that of Pedlosky (1975); however, Pedlosky focused on the effect of air-sea interaction on baroclinic instability, and thus retained time derivatives in the atmospheric dynamics. Finally, if the terms associated with ocean dynamics are neglected on the right side of (2.24), then (2.24-2.26) reduce to a set studied by Frankignoul (1985).

2.2 Dispersion relations and form of coupled modes

We now proceed to solve the coupled set of equations set out in Section 2.1, show that they support coupled modes and derive their dispersion relation. We then go on to discuss the physical mechanism behind the coupled behavior in the light of observed

phenomena.

2.2.1 Plane wave solutions

The coupled equations are linear and isotropic, and contain only even derivatives in y, so we look for plane wave solutions of the form:

$$\widehat{\psi} = \widehat{\psi}' e^{i(kx-\sigma t)} \sin ly \qquad \widetilde{\psi} = \widetilde{\psi}' e^{i(kx-\sigma t)} \sin ly$$

$$\psi_o = \psi_o' e^{i(kx-\sigma t)} \sin ly \qquad \mathrm{SST} = \mathrm{SST}' e^{i(kx-\sigma t)} \sin ly$$

These waves have the same spatial scale and frequency in both ocean and atmosphere; they move together in lock-step, with only amplitude differences and phase offsets. Inserting these wavelike forms, canceling a common factor of $e^{i(kx+ly-\sigma t)}$ and dropping the primes for notational convenience, (2.23) through (2.26) can be written:

$$\frac{i}{L_o^2}\sigma\psi_o + \beta ik\psi_o = -\alpha\kappa^2(\frac{1}{2}\widehat{\psi} - \widetilde{\psi}) \tag{2.27}$$

$$-i\sigma\mathrm{SST} = -\gamma_o(\mathrm{SST} - r_a\widetilde{\psi}) + ikar_o\psi_o - \gamma_e(\mathrm{SST} - r_o\psi_o) \tag{2.28}$$

$$-\widehat{U}ik\kappa^2\widehat{\psi} + \widehat{\beta}ik\widehat{\psi} - \widetilde{U}ik\kappa^2\widetilde{\psi} = 0 \tag{2.29}$$

$$-\widetilde{U}ik\kappa^2\widehat{\psi} + \widetilde{\beta}ik\widehat{\psi} - \widehat{U}ik\kappa_a^2\widetilde{\psi} + \widehat{\beta}ik\widetilde{\psi} = \frac{4}{L_a^2}\gamma_a(\widetilde{\psi} - \frac{1}{r_a}\mathrm{SST}) \tag{2.30}$$

where

$$\kappa^2 = k^2 + l^2$$

is the the total squared wavenumber, and

$$\kappa_a^2 = \kappa^2 + \frac{2}{L_a^2}$$

2.2.1.1 The atmosphere

Because of the simplicity of our atmospheric model, we may solve (2.29) to find the barotropic response $\widehat{\psi}$ in terms of the baroclinic flow $\widetilde{\psi}$ thus:

$$\widehat{\psi} = -\mu\widetilde{\psi} \tag{2.31}$$

where:

$$\mu \equiv \frac{\widetilde{U}}{\widehat{U} - \widehat{\beta}/\kappa^2} \tag{2.32}$$

The relative strength of the barotropic and baroclinic modes is controlled by μ, a measure of the ratio of vertical wind shear to the barotropic Rossby wave speed, Doppler-shifted by the barotropic mean wind. On scales close to that of stationary barotropic Rossby waves, $|\mu|$ is large and atmospheric perturbations are 'equivalent barotropic'. When $|\mu|$ is small, perturbations change sign between levels 1 and 2. As described in detail in Section 2.2.1.2, the vertical structure of the atmospheric response to thermal forcing plays a key role in the coupled mode.

Turning now to the baroclinic response of the atmosphere, let us first imagine that the SST (and hence, in view of (2.19), $\delta\phi^*$) is fixed in space and time and consider the response of the atmosphere to a fixed SST anomaly. Equation (2.31) may be used to eliminate $\widehat{\psi}$ from (2.30) to yield, after dividing by $i\kappa^2$:

$$\left(\widetilde{U}k\mu - \frac{\widetilde{\beta}k}{\kappa^2}\mu - \widehat{U}k\frac{\kappa_a^2}{\kappa^2} + \frac{\widehat{\beta}k}{\kappa^2} + \frac{4i\gamma_a}{\kappa^2 L_a^2}\right)\widetilde{\psi} = \frac{4i\gamma_a}{\kappa^2 L_a^2}\frac{1}{r_a}\mathrm{SST}$$

Let us identify the terms in the above. The Newtonian relaxation process can be viewed as a balance between constant external forcing and linear damping: the terminal velocity of a falling object is a useful analog. The damping (radiative heat loss) is the imaginary term on the left, the forcing (heating from the surface) is the term on the right. The (inverse) thermal damping time scale of a PV anomaly of scale κ^2 is clearly:

$$\Gamma \equiv \frac{4\gamma_a}{\kappa^2 L_a^2} \tag{2.33}$$

This should be compared with an advective-propagation time-scale over the same distance (stemming from the left side of 2.30) given by:

$$\nu \equiv -\widetilde{U}k\mu + \frac{\widetilde{\beta}k}{\kappa^2}\mu + \widehat{U}k\frac{\kappa_a^2}{\kappa^2} - \frac{\widehat{\beta}k}{\kappa^2} \tag{2.34}$$

This is a measure of the frequency of free Rossby waves in the atmosphere, Doppler-shifted by the mean zonal wind. It can be interpreted as a timescale for a free atmospheric Rossby wave to travel across the heating anomaly. In terms of ν and Γ the baroclinic response can be expressed succinctly thus:

$$\left(1 + i\frac{\nu}{\Gamma}\right)\widetilde{\psi} = \frac{1}{r_a}\text{SST} \tag{2.35}$$

yielding information about the phase and amplitude of the atmospheric response relative to the forcing. It says that warm SST must heat the atmosphere generating atmospheric pressure anomalies which increase with height ($\widetilde{\psi} > 0$) with a phase shift $< 90°$. Evidently, if the thermal equilibration timescale is much faster than the advective-propagation time-scale on the scale k of the thermal anomaly, then $\Gamma \gg |\nu|$, so $\widetilde{\psi}$ is large and is in phase with SST. Applying our formulae to Shutts' experiment (Figure 2-2), the equilibrated response, plotted in Figure 2-2b, has $\frac{\nu}{\Gamma} = 0.5$; $\mu = -3$ for the dominant wavenumber 3 response. However, if the advective-propagation times-scales are short compared to the time-scale of the radiative 'spring' pulling θ back to θ^*, then $|\nu| \gg \Gamma$ so the atmospheric response is weaker and out of phase with ψ_o. This is the 'forced' response shown in Figure 2-2a) in which $\frac{\nu}{\Gamma} = 2.7$; $\mu = +\frac{1}{3}$.

It is interesting to note that even though we have sought the *stationary forced* atmospheric response, $\widetilde{\psi}$, its form is sensitive to ν because of (2.35) and hence to the properties of the *traveling free* waves of the system.

2.2.1.2 The coupled mode

We now consider the dynamic response of the ocean: SST is no longer fixed but evolves according to (2.28), driven by the ocean equation (2.27).

We may write (2.35) as

$$(\mathrm{SST} - r_a\widetilde{\psi}) = (\nu/\Gamma)\frac{i+\nu/\Gamma}{1+(\nu/\Gamma)^2}\mathrm{SST} \equiv m\mathrm{SST} \tag{2.36}$$

where m is complex. Note that when the atmosphere is in the "equilibrated mode" ($\nu/\Gamma \to 0$), the air-sea temperature difference (and thus the surface heat flux) is zero.

Now we may use (2.36) to eliminate $(\mathrm{SST} - r_a\widetilde{\psi})$ from (2.28), solving it for SST in terms of ψ_o:

$$\mathrm{SST} = \left(\frac{ika+\gamma_e}{-i\sigma+\gamma_e+m\gamma_o}\right) r_o\psi_o \tag{2.37}$$

Next, we eliminate SST by inserting (2.37) into (2.35):

$$\left(1+i\frac{\nu}{\Gamma}\right)\widetilde{\psi} = \left(\frac{ika+\gamma_e}{-i\sigma+\gamma_e+m\gamma_o}\right) r\psi_o \tag{2.38}$$

where we have defined

$$r \equiv \frac{r_o}{r_a} = \frac{H}{2\varepsilon\theta_{a0}h} \tag{2.39}$$

The scaling term r sets the scale between oceanic and atmospheric streamfunction through their mutual connection to temperature.

From (2.38), the forcing of the atmospheric streamfunction by the oceanic streamfunction is mediated by the processes which set SST in the model. The parameter γ_e is a measure of the strength of the entrainment process, the parameter ak (which has units of 1/time) is a measure of the strength of advection of SST gradients, and $m\gamma_o$ measures the influence of air-sea flux on SST. In the entrainment process, low streamfunction implies a raised thermocline, which means the mixed layer is entraining cool water, reducing SST and so cooling the atmosphere. In the advection process, meridional currents advect warm or cool SST, which also forces the atmosphere.

Equation (2.38) is a relation between $\widetilde{\psi}$ and ψ_o. Another is provided by (2.27),

which can be written, using (2.31):

$$(\sigma - \omega_r)\,\psi_o = -i\alpha\kappa^2 L_o^2 \left(\frac{\mu}{2} + 1\right)\widetilde{\psi} \tag{2.40}$$

where ω_r is the oceanic baroclinic Rossby wave frequency

$$\omega_r \equiv -\beta k L_o^2$$

For (2.40) to be consistent with (2.38), either $\widetilde{\psi} = \widetilde{\psi}_o = 0$ or

$$\left(\frac{-i\sigma + \gamma_e + m\gamma_o}{iak + \gamma_e}\right)(\sigma - \omega_r)\,(-\nu + i\Gamma) = r\Gamma\alpha\kappa^2 L_o^2 \left(\frac{\mu}{2} + 1\right) \tag{2.41}$$

This is a quadratic dispersion relation for waves in our coupled system. The left side of (2.41) is comprised of the product of three terms. The first describes the response of SST to ocean dynamics and air-sea interaction. The second describes the propagation of thermocline anomalies as Rossby waves (note the term ω_r) and the third describes the quasi-stationary response of the atmosphere to SST anomalies. The right-hand side involves the feedback forcing of atmospheric windstress back onto the ocean dynamics (note the presence of α). The solutions of (2.41) are:

$$\sigma = \frac{1}{2}\left(\omega_r - i\gamma_e - im\gamma_o\right) \pm i\sqrt{-\frac{1}{4}\left(\omega_r + i\gamma_e + im\gamma_o\right)^2 + r\left(-ak + i\gamma_e\right)\left[\alpha\kappa^2 L_o^2\left(\frac{\mu}{2} + 1\right)\frac{\frac{\nu}{\Gamma} + i}{\left(\frac{\nu}{\Gamma}\right)^2 + 1}\right]} \tag{2.42}$$

We note immediately that the presence of imaginary terms indicates the possibility of growth or decay of the wave. The possibility of a growing coupled mode is the centerpiece of the model because infinitesimal perturbations of the system can then grow to large amplitude. If growing coupled modes exist, then they can be self-starting and sustain themselves against dissipative effects which will become more and more important as the coupled mode reaches finite amplitude.

2.2.2 Form and growth mechanism of coupled mode

The complexity of (2.42) stems from the several different processes that play a role in the SST equation (2.21). To gain an understanding of the physics of the coupling, we must simplify the dispersion relation (2.42). We will now consider several different cases, including only one or two terms in the SST equation in turn to study their influence in isolation. We will begin with the simplest case which illustrates the coupled interaction, and then consider other processes which modify this underlying mechanism.

2.2.2.1 SST Case 1: Entrainment

The simplest case is the one where entrainment dominates the SST equation, and advection, air-sea flux, and tendency are small. Then (2.21) reduces to

$$0 = -\gamma_e(\mathrm{SST} - \theta_{\mathrm{sub}})$$

$$\mathrm{SST} = \theta_{\mathrm{sub}} = r_o\psi_o \tag{2.43}$$

implying perfect communication between thermocline perturbations and SST. Dominance of entrainment requires that $\gamma_e \gg ak$, $\gamma_e \gg \sigma$, $\gamma_e \gg m\gamma_o$ (numerical values are considered in Section 2.3). Then the first term on the left side of (2.41) reduces to 1, and there is only one solution to the now linear equation for σ:

$$\sigma = \omega_r - r\left[\alpha\kappa^2 L_o^2\left(\frac{\mu}{2}+1\right)\frac{\frac{\nu}{\Gamma}+i}{\left(\frac{\nu}{\Gamma}\right)^2+1}\right] \tag{2.44}$$

The waves of our system move in a phase-locked fashion through the ocean and atmosphere. Because the dynamical ocean is the only prognostic field (the SST tendency term has been neglected), from one perspective the fluctuations exist fundamentally in the ocean. They are manifest in the atmosphere because it responds to the modification of SST (and hence thermal forcing) induced by the ocean. But the ocean only moves because the atmosphere blows over it — thus our mode is a

coupled one.

We see the ocean connection by the presence of the oceanic Rossby wave frequency ω_r in (2.44). The second term in (2.44) contains a real part created by air-sea interaction which (slightly) slows down or speeds up the oceanic Rossby waves. But σ also has an imaginary part:

$$Im(\sigma) = -r\alpha\kappa^2 L_o^2(\frac{\mu}{2}+1)\frac{1}{\left(\frac{\nu}{\Gamma}\right)^2+1} \tag{2.45}$$

Since the waves have the form $e^{i(kx-\sigma t)}\sin ly$, then $Im(\sigma)$ must be positive for growth. All the variables in (2.45) are positive-definite except $(\frac{\mu}{2}+1)$. For $Im(\sigma) > 0$, we need $\mu/2 + 1 < 0$. What is the physical meaning of this condition on μ? It arose from the "surface windstress" term in the oceanic forcing (2.18). Since

$$\psi_s = \frac{1}{2}\widehat{\psi} - \widetilde{\psi} = -(\frac{\mu}{2}+1)\widetilde{\psi}$$

surface streamfunction anomalies have the same sign as the vertical shear $\widetilde{\psi}$ when $\mu < -2$: *i.e.* the waves are then 'equivalent barotropic'.

Waves near barotropic resonance ($\widehat{U} \approx \frac{\widehat{\beta}}{\kappa^2}$, with $|\mu|$ large) exhibit the strongest barotropic response, and therefore grow the fastest. But the growth rates also depend on the size of the equilibration term Γ relative to the advection-propagation parameter ν; ν depends on $\widehat{U}$, $\widetilde{U}$, and the wave size. When $|\nu| \ll \Gamma$, the wave has time to equilibrate with the oceanic forcing (i.e., the left- and right-hand sides of (2.26) independently approach zero). A large response will be excited, enhancing the coupling. But if advection-propagation is much more rapid than equilibration ($|\nu| \gg \Gamma$), the response of the atmosphere is smaller and shifted away from the oceanic SST anomaly, and growth of the coupled mode is slowed. These effects are encapsulated in the factor $\left(\left(\frac{\nu}{\Gamma}\right)^2+1\right)^{-1}$ in (2.45). It is the equilibrated atmospheric modes that couple most efficiently and grow most rapidly.

The structure of the fastest-growing mode for the entrainment-dominated SST case is sketched in Figure 2-4. As described above, any mode with positive growth

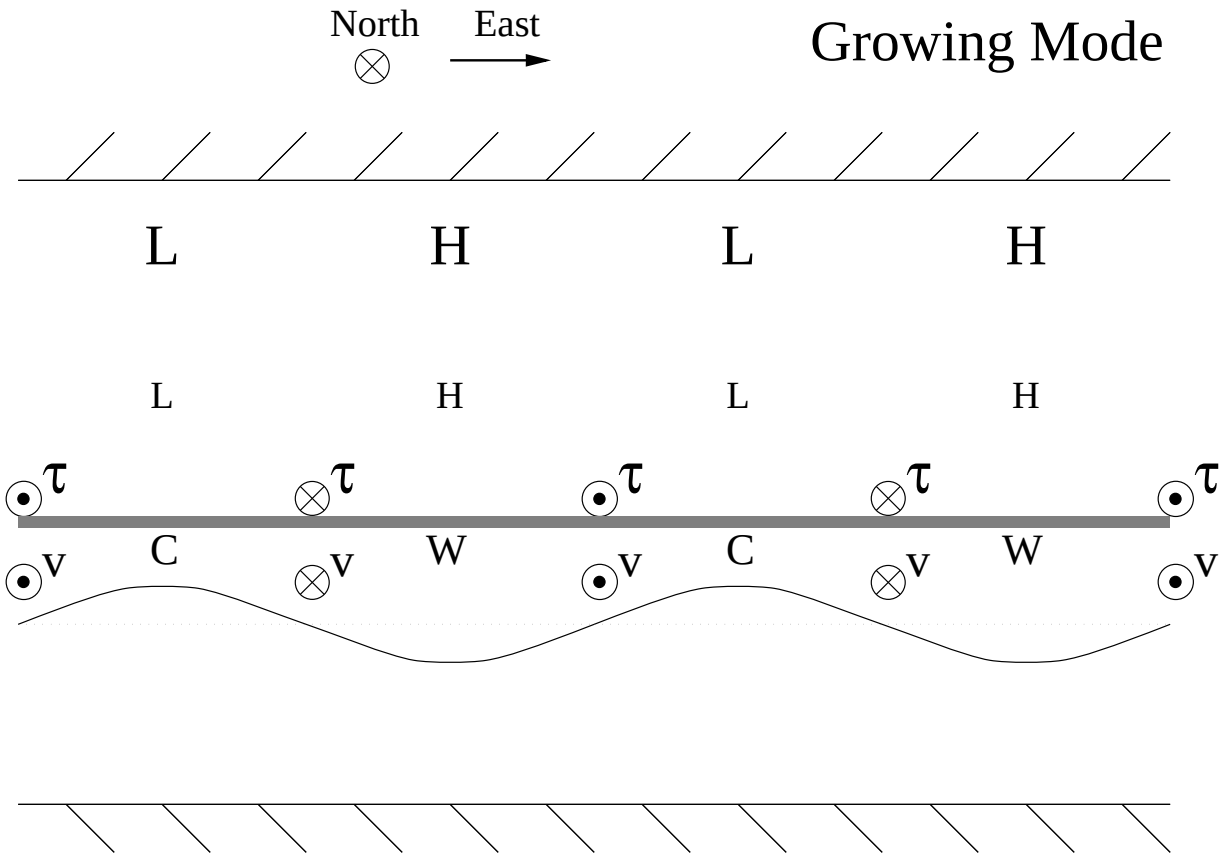

Figure 2-4: Phase relationships between ocean and atmosphere for the fastest growing coupled mode. The symbols H and L denote highs and lows of atmospheric pressure, with the amplitude of the pressure anomaly increasing with height. The atmospheric response is 'equilibrated', as in figure 2b. The symbols W and C denote warm and cold SST, and the undulating line indicates the depth of the thermocline. Note the high (low) pressure above warm (cold) water, and the phase match between wind stress and current.

rate must have $\mu < -2$, so the atmospheric response is equivalent barotropic ($|\psi_1| > |\psi_2| > |\psi_s|$ and each has the same sign), weakest at the surface and strongest aloft. If the surface pressure anomaly is positive, the resultant anticyclonic surface winds will cause downward Ekman pumping in the ocean which deepens the already-deep thermocline leading (see (2.43)) to a warmer surface and a positive feedback. If the surface pressure anomaly is negative, Ekman dynamics will suck up the thermocline resulting in anomalously cold winter SST, again a positive feedback. For the coupling physics adopted here, coupled growth will occur whenever the atmospheric response is equivalent barotropic.

The atmospheric and oceanic wave components need not be in phase with one another, and the degree of phase-matching determines the rate at which the coupled mode grows. Growth is fastest when ν/Γ is small in (2.45), which (from (2.35) and (2.43)) occurs when the atmosphere equilibrates completely with the underlying ocean, and high pressures occur directly over warm, deep-thermocline water ($\widetilde{\psi} \propto$ SST $\propto \psi_o$). Then the Ekman pumping acts directly to increase the amplitude of thermocline perturbations; the wind applies torque to the ocean to reinforce the existing circulation. As the advection/propagation term $|\nu|$ increases, the atmospheric perturbation is "blown away" from the oceanic anomaly which generates it, resulting in a phase lead or lag; the Ekman pumping no longer perfectly matches the location of greatest anomaly, so growth is slower. When $|\nu|$ completely dominates Γ, the phase shift is 90° ($\widetilde{\psi} \propto i$SST; $\widetilde{\psi} \propto i\psi_o$). In this case, the Ekman pumping does not increase the thermocline anomalies at all because the wind forcing is in quadrature with the ocean response. These two cases (zero lag and quadrature) correspond to the equilibrated and directly-forced modes shown in Figure 2-2. More specifically, the atmospheric wave lies westward of the oceanic wave by a phase angle:

$$\theta = \mathrm{Tan}^{-1}\left(\frac{\nu}{\Gamma}\right) \tag{2.46}$$

If $\nu > 0$, atmospheric pressure crests lie eastward of SST maxima, and vice versa for $\nu < 0$.

For atmosphere-ocean phase shifts between 90° and -90° , in the growing mode the circulation induced by oceanic thermal forcing yields a windstress which reinforces the sense of the pre-existing circulation. If the waves are able to equilibrate with their energy source ($|\nu| \ll |\Gamma|$), growth is rapid and the atmospheric geopotential anomalies lie directly over their SST sources. But if the waves in the atmosphere propagate away from the energy source more rapidly than that source can be renewed ($|\nu| \gg |\Gamma|$), the coupled phenomenon grows slowly, with atmospheric waves shifted downstream from their SST sources (see (2.35)). In all cases of growth, though, the atmospheric anomaly hovers near the SST heat source.

It is useful to draw an analogy with a burning candle. The heat of the flame melts and vaporizes the wax directly below it, which then provides chemical energy to allow the flame to grow and maintain itself. If we blow gently on the candle flame, we may transport it away from its fuel source faster than the fuel is renewed: the flame weakens, and may die if we blow hard enough. In all cases, though, the flame hovers above or beside the wick.

2.2.2.2 SST Case 2: Entrainment & Tendency

What happens if we include the SST tendency term in equation (2.21), but still neglect meridional advection (and therefore ak in (2.42))? In the limit where $ak \ll \gamma_e$, (2.42) reduces to

$$\sigma = \frac{1}{2}\left(\omega_r - i\gamma_e\right) \pm i\sqrt{-\frac{1}{4}\left(\omega_r - i\gamma_e\right)^2 - i\gamma_e\omega_r + i\gamma_e r\left[\alpha\kappa^2 L_o^2\left(\frac{\mu}{2}+1\right)\frac{\frac{\nu}{\Gamma}+i}{\left(\frac{\nu}{\Gamma}\right)^2+1}\right]} \tag{2.47}$$

In the case where entrainment is much faster than Rossby propagation ($\gamma_e \gg \omega_r$) and is also faster than the air-sea coupling ($\gamma_e \gg r[\,]$), we may use the approximation $\sqrt{1+x} \approx 1 + x/2$ to find the approximate solutions:

$$\sigma_1 \approx \omega_r - r\alpha\kappa^2 L_o^2\left(\frac{\mu}{2}+1\right)\frac{\frac{\nu}{\Gamma}+i}{\left(\frac{\nu}{\Gamma}\right)^2+1} \tag{2.48}$$

$$\sigma_2 \approx -i\gamma_e + r\alpha\kappa^2 L_o^2\left(\frac{\mu}{2}+1\right)\frac{\frac{\nu}{\Gamma}+i}{\left(\frac{\nu}{\Gamma}\right)^2+1} \tag{2.49}$$

The first solution is identical to the entrainment solution without the tendency term (2.44), described in detail in Section 2.2.2.1. The second solution is dominated by rapid SST damping through entrainment (*i.e.*, by the $-i\gamma_e$ term). The Rossby wave propagation term canceled in the expression for σ_2: the solution does not propagate as a Rossby wave, and is, in fact, decoupled from the dynamic ocean: therefore we call it an "SST-only" mode. The second term, describing the air-sea interaction, has the opposite sign in the SST-only mode as in the "entrainment mode" discussed

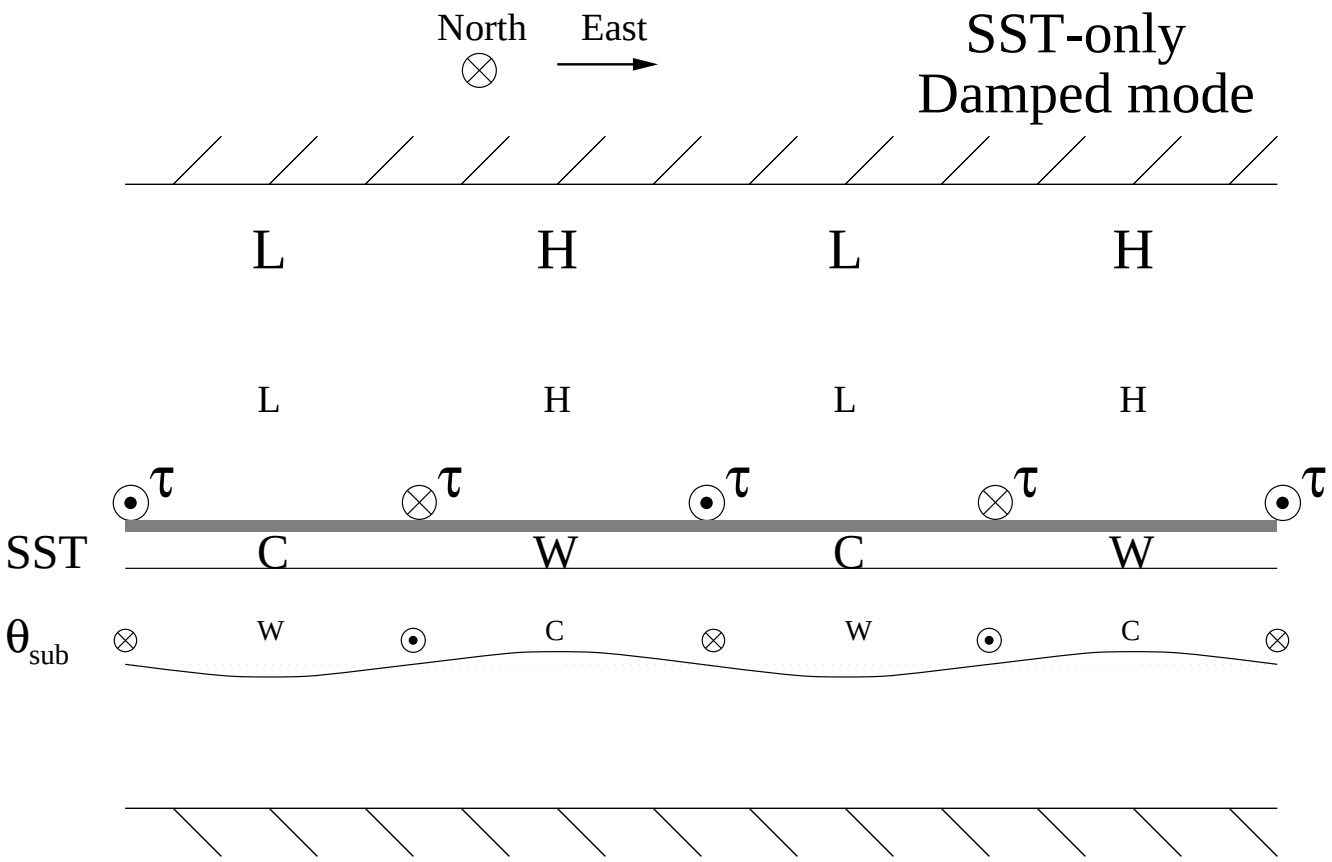

Figure 2-5: Configuration of the rapidly-damped SST-only mode (equation (2.49)). SST is out of phase with the very small subsurface thermal anomalies, leading to rapid damping of SST.

in Section 2.2.2.1, suggesting that the conditions for growth discussed there cause enhanced decay in this mode.

The structure of the SST-only mode is quite simple, and is depicted in Figure 2-5. We begin with a warm patch of SST, but with only a slightly perturbed thermocline having the opposite sign as SST. The SST patch generates an atmospheric response above or downstream from it (depending on ν/Γ), but the patch is rapidly damped by the $\gamma_e(\mathrm{SST} - \theta_{\mathrm{sub}})$ term in (2.21), and decays in a short time $1/\gamma_e$. The slight Ekman pumping supplied by the wind during that time acts only to diminish the initial thermocline anomaly; thus all fields decay to zero rapidly.

The two solutions span the range of possible initial conditions for SST and ψ_o. If we begin with an arbitrary pattern of SST and ψ_o, the component which has SST and ψ_o in phase will grow and propagate as described in Section 2.2.2.1 (assuming

conditions for growth are met), while the out-of-phase component will decay rapidly via the process described here, until only the in-phase component is observed.

2.2.2.3 SST Case 3: Advection & Tendency

Even though our SST scaling analysis suggests that entrainment is at least as important as advection in winter months, it is useful to consider the advection mechanism in isolation. Accordingly, we consider the form of the SST equation (2.21) with $\gamma_e \to 0$ and $\gamma_o \to 0$.

$$\frac{\partial}{\partial t}\mathrm{SST}' = -\vec{u'} \cdot \nabla\overline{\mathrm{SST}}$$

In the same limit, the dispersion relation (2.42) becomes

$$\sigma = \frac{1}{2}\omega_r \pm i\sqrt{-\frac{1}{4}\omega_r^2 - rak\left[\alpha\kappa^2 L_o^2\left(\frac{\mu}{2}+1\right)\frac{\frac{\nu}{\Gamma}+i}{\left(\frac{\nu}{\Gamma}\right)^2+1}\right]} \tag{2.50}$$

As before, we consider the case where the coupling term $rak[\ ]$ is smaller than the Rossby wave propagation term ω_r, in which case we get the following two approximate solutions:

$$\sigma_1 = \omega_r - \frac{rak}{\omega_r}\left[\alpha\kappa^2 L_o^2\left(\frac{\mu}{2}+1\right)\frac{\frac{\nu}{\Gamma}+i}{\left(\frac{\nu}{\Gamma}\right)^2+1}\right] \tag{2.51}$$

$$\sigma_2 = \frac{rak}{\omega_r}\left[\alpha\kappa^2 L_o^2\left(\frac{\mu}{2}+1\right)\frac{\frac{\nu}{\Gamma}+i}{\left(\frac{\nu}{\Gamma}\right)^2+1}\right] \tag{2.52}$$

The solution σ_1 has exactly the same structure as the entrainment mode described in Section 2.2.2.1, with r replaced by rak/ω_r. Growth occurs in this "advection mode" when the atmosphere responds with barotropic highs over warm water, exactly as in Section 2.2.2.1.

Like the entrainment mode, the advection mode has warm SST where ψ_o is large (see Figure 2-4), but for an entirely different reason, illustrated in Figure 2-6. Oceanic streamfunction anomalies will propagate from east to west. A streamfunction high (depressed thermocline) will generate a northward flow to its west, advecting warm

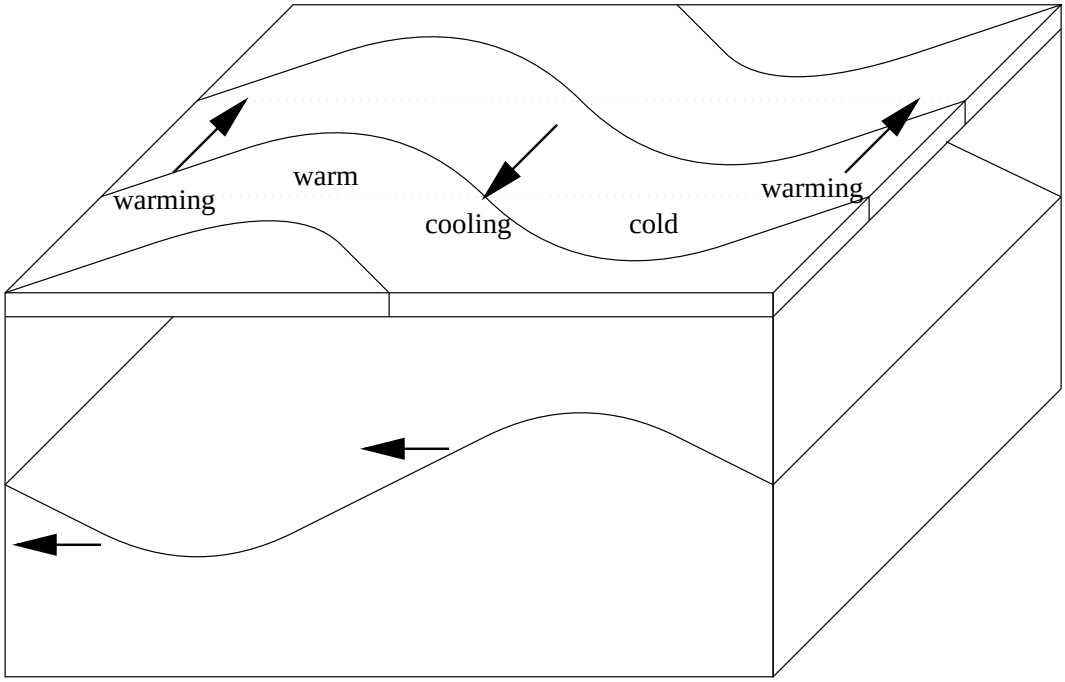

Figure 2-6: The process by which advection of mean meridional SST gradient leads to warm SST anomalies over deep-thermocline water. See text for full description.

water from the south and creating a warming trend there. When the ψ_o anomaly propagates to that spot, the advection ceases, and so does the warming. When the ψ_o anomaly continues on to the west, it generates southward flow, bringing cold water which cools the SST patch. Therefore, a maximum in SST is observed at the maximum in ψ_o, and appears to follow that maximum as it propagates westward. SST and ψ_o are in phase, and waves which propagate more slowly have more time to build up larger SST anomalies: this is why the Rossby-wave propagation term occurs in the denominator of the second term in σ_1.

The second solution has no Rossby-wave propagation, and SST and ψ_o are out of phase. The solution is most strongly damped when air-sea coupling is strong.

2.2.2.4 SST Case 4: Air-sea flux, entrainment, and tendency

The inclusion of the surface flux term into the SST equation should reduce the growth of the coupled mode: after all, if a warm patch of SST is losing heat to the atmosphere at a rate comparable to the rate of heating by entrainment or advection, the anomaly

will have smaller magnitude and thus generate a less powerful atmospheric circulation. However, the most rapidly growing mode from the previous three cases is unaffected by the air-sea flux term. Our fastest-growing mode has $\nu/\Gamma = 0$, so m=0 in (2.36): SST $= \theta_a = r_a\widetilde{\psi}$: there is no air-sea temperature difference (complete equilibration), so the surface heat flux shuts off. In fact, by setting m=0 in (2.41), we get (2.47) when advection is small.

We now consider the case where m is nonzero, but for convenience we assume advection is small ($ak \ll \gamma_e$); our results will also hold for non-negligible ak. In the limit $m\gamma_o \gg \omega_r$ and $m\gamma_o \gg r[\ ]$, (2.42) can be approximated by:

$$\sigma_1 \approx \omega_r - \frac{\gamma_e}{\gamma_e + m\gamma_o} r\alpha\kappa^2 L_o^2 \left(\frac{\mu}{2} + 1\right) \frac{\frac{\nu}{\Gamma} + i}{\left(\frac{\nu}{\Gamma}\right)^2 + 1} \tag{2.53}$$

$$\sigma_2 \approx -i\gamma_e - im\gamma_o + \frac{\gamma_e}{\gamma_e + m\gamma_o} r\alpha\kappa^2 L_o^2 \left(\frac{\mu}{2} + 1\right) \frac{\frac{\nu}{\Gamma} + i}{\left(\frac{\nu}{\Gamma}\right)^2 + 1} \tag{2.54}$$

These two modes closely resemble the entrainment modes discussed in Section 2.2.2.2; however, the coupled growth term of the coupled solution (σ_1) is multiplied by the factor $\gamma_e/(\gamma_e + m\gamma_o)$, and damping of the "SST-only" solution (σ_2) is enhanced by the air-sea flux. If $\gamma_e \approx \gamma_o$ (typical of the annual average), growth off-resonance (where $||m|| \sim 1$) is reduced by about a factor of two. During the winter, when γ_e is larger than γ_o, growth will not be significantly affected. During the summer, when $\gamma_e \sim 0$, (2.53) and (2.54) reduce to

$$\sigma_1 \approx \omega_r \qquad \sigma_2 \approx -im\gamma_o = \frac{\nu/\Gamma - i(\nu/\Gamma)^2}{1 + (\nu/\Gamma)^2}\gamma_o \tag{2.55}$$

Coupling between the geostrophic ocean and the mixed layer has ceased entirely; the first solution takes the form of uncoupled propagating oceanic Rossby waves with no expression in the mixed layer or atmosphere; the second equation shows the effect of a 2-layer QG atmosphere over a "swamp" mixed layer. This mode resembles the "QG atmosphere over a copper plate" discussed by Frankignoul (1985): it is characterized by rapidly-damped patterns in SST and atmosphere which propagate eastward or

westward depending on the phase of the atmosphere's response to SST. If warm SST produces warm air to the east of the SST anomaly ($\nu/\Gamma > 0$), this warmth results in a heat flux back into the ocean farther east than it originated, resulting in eastward phase propagation, and vice versa for westward phase shifts. However, since this "heat flux" mode is always damped on a timescale of order $\gamma_o^{-1} \sim 8$ months, it is unlikely to play a role in decadal variability.

Allowing air-sea flux to affect the mixed layer cannot destroy our growing mode, because the fastest-growing mode has vanishingly small air-sea flux. However, it may reduce growth rates somewhat when conditions are slightly off-resonance. When air-sea flux dominates over entrainment (as might happen in summer), the mixed layer decouples from the dynamic ocean; Rossby waves continue to propagate in the thermocline while the mixed layer exhibits rapidly-damped air-sea interaction as described by Frankignoul (1985).

2.3 Discussion of solutions: predictions and sensitivity

We now discuss the numerical values of the various parameters that characterize our model and go on to consider its relevance to middle-latitude air-sea coupling. Comparisons of our model with observed variability patterns are also made.

2.3.1 Frequency and scales

Oceanic Rossby waves with a frequency of $\omega_r = 2 \cdot 10^{-8}$ s^{-1} have a wave period of 10 years or so and thus could be implicated in decadal variability. This then implies a zonal wavenumber of $k = \pi/5500$ km (for $L_o = 45$ km and $\beta = 1.8 \cdot 10^{-11}$ s^{-1} m^{-1}), a scale comparable to that of an ocean basin, and commensurate with, for example, the scales of the leading modes of variability found by Deser & Blackmon (1993) and Cayan (1992). It turns out that the modification of the real part of the phase speed associated with coupling (the second term in (2.44)) is comparatively small (see

below) and does not make a significant difference to the phase speed. Our advection and entrainment coupled modes propagate at essentially the speed of internal oceanic Rossby waves.

In Figure 2-7, μ is plotted as a function of $\widehat{U}$ and $\widetilde{U}$ for a wave of size comparable to the NAO; $k = \pi/5500$ km and $l = \pi/3200$ km. For $\widehat{U} > \frac{\widehat{\beta}}{\kappa^2} = 28$ m/s, μ is positive, implying an atmospheric response which switches sign between upper and lower levels, leading to a decaying mode. In the lower left part of the Figure, $0 > \mu > -2$, again implying damping. An equivalent barotropic response (and therefore a growing mode) will occur if the zonal winds fall in the central triangular region. This can readily be achieved by typical middle-latitude tropospheric winds.

2.3.2 Coupling constants

2.3.2.1 Mechanical

Let α' scale the stress of the wind, τ, to the surface wind speed u_s thus:

$$\tau' = \alpha' {u_s}' \tag{2.56}$$

To deduce a value for α', consider the bulk aerodynamic drag law for the total (mean + anomaly) windstress (see Gill, 1982):

$$\overline{\tau} + \tau' = c_{_D} \rho_a (\overline{u_s} + {u_s}')^2$$

where $c_{_D}$ is the drag coefficient. After linearizing about the mean $\overline{u_s}$, we obtain

$$\tau' = 2 c_{_D} \rho_a \overline{u_s} \cdot {u_s}' \tag{2.57}$$

allowing us to identify:

$$\alpha' = 2 c_{_D} \rho_a \overline{u_s}$$

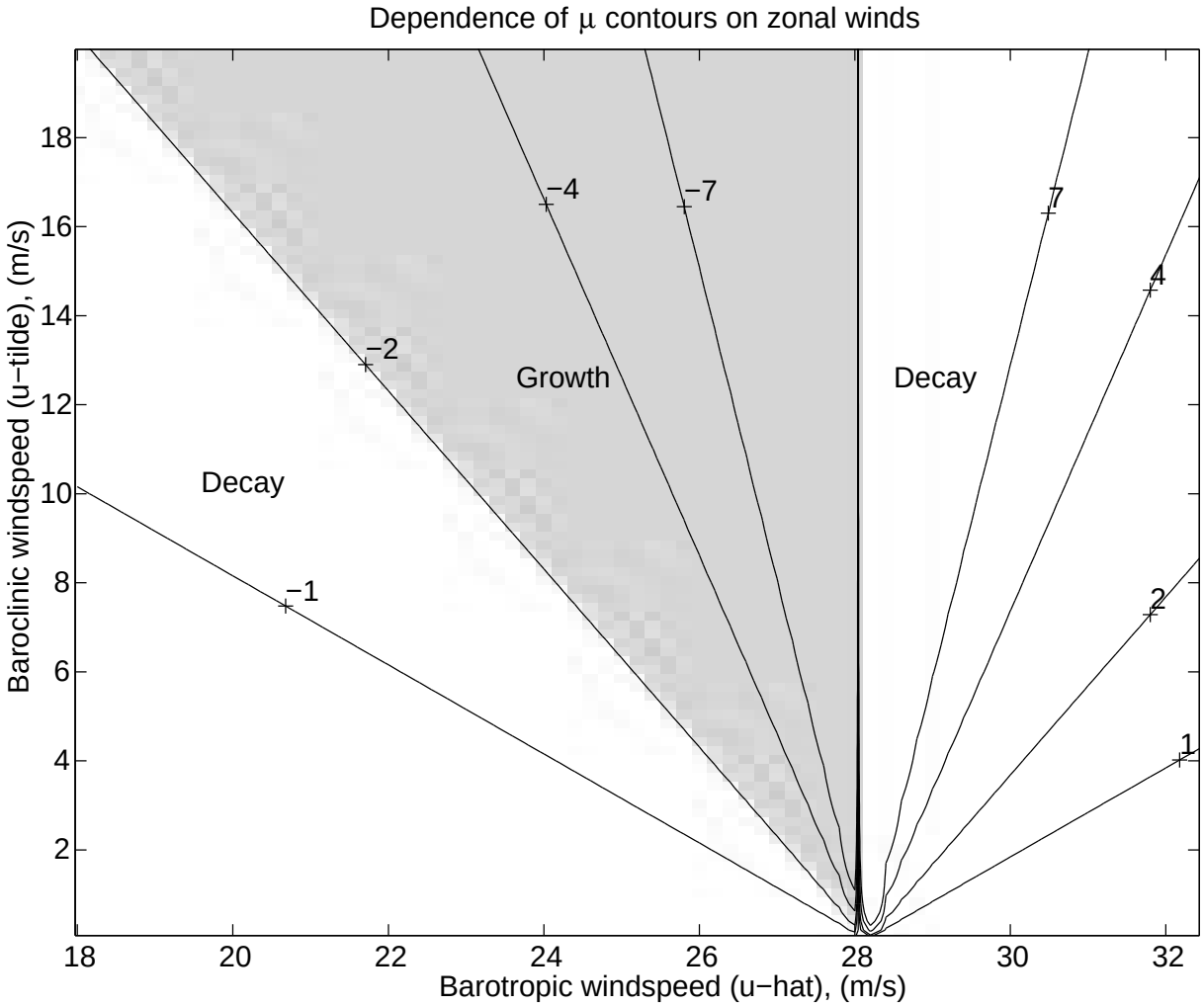

Figure 2-7: Contours of μ from equation (2.32) as a function of barotropic ($\widehat{U} = u_1+u_2$) and baroclinic ($\widetilde{U} = u_1-u_2$) wind speed, for a particular choice of wavenumber ($k = \frac{\pi}{5500\text{km}}$, $l = \frac{\pi}{3200\text{km}}$.) A growing coupled mode is possible when $\mu < -2$ (the shaded region of the figure).

Comparing (2.18), (2.56) and (2.57), we see that:

$$\alpha = \frac{\alpha'}{\rho_{o0} h} = \frac{2 c_{_D} \rho_a \overline{u_s}}{\rho_{o0} h}$$

In accord with observations, for $\overline{u_s} = 5$ m/s, $h = 500$ m, we find that $\alpha \approx \frac{2 \times 1.3 \cdot 10^{-3} \times 1 \times 5}{10^3 \times 500} = 3 \cdot 10^{-8}\ s^{-1} = \frac{1}{1.1 \text{ years}}$ if $c_{_D} = 1.3 \cdot 10^{-3}$.

2.3.2.2 Thermal Equilibration

The inverse damping time-scale of a PV anomaly, $\Gamma \equiv \frac{4\gamma_a}{\kappa^2 L_a^2}$, (2.33), depends on the scale of the anomaly relative to the deformation radius and the radiative-convective restoring time-scale. Inserting typical numbers we find

$$\Gamma \equiv \left[4 \frac{1}{14 \text{ days}} \left(\frac{1}{660 \text{ km}} \right)^2 \right] \left[10^{-12} \text{ m}^{-2} \right]^{-1} = 7.7 \cdot 10^{-6} \text{ s}^{-1} = \frac{1}{1.5 \text{ days}}$$

This time-scale becomes shorter the greater the scale of the anomaly relative to the deformation radius.

2.3.2.3 SST

By putting numbers into (2.39) we find that the SST coupling parameter $r \equiv H/(2\varepsilon\theta_{a0} h) \approx 10^4 \left(2 \cdot 10^{-4} \cdot 290 \cdot 500\right)^{-1} \approx 340$. A reasonable value for a is $a \equiv (gh\varepsilon/f) \frac{\partial}{\partial y} \overline{\text{SST}} = 10 \cdot 500 \cdot 10^{-4}/10^{-4}) \cdot 3 \cdot 10^{-6} = 0.015$ m s^{-1}. With $k = 5 \cdot 10^{-7}$ m^{-1}, the advection timescale is $ak = 7.5 \cdot 10^{-9}$ s^{-1}. In Section 2.1.4.2, we established the entrainment parameter $\gamma_e = 1.3 \cdot 10^{-7}$s^{-1} and the air-sea flux parameter $\gamma_o = 5 \cdot 10^{-8}$s^{-1}. If $\sigma \sim \omega_r \sim 2 \cdot 10^{-8}$ s^{-1}, then for this choice of parameters $\gamma_e \gg \sigma$, $\gamma_e \gg ak$, $\gamma_e > \gamma_o$, so the entrainment solution should dominate in the full dispersion relation (2.41), perhaps with some contribution from air-sea flux. Furthermore, the second and third terms beneath the radical in (2.42) are smaller than the first, so the approximation leading to (2.48) and (2.49) should be valid. We now compute growth rates as a function of wavelength and other parameters to see if this is indeed the case.

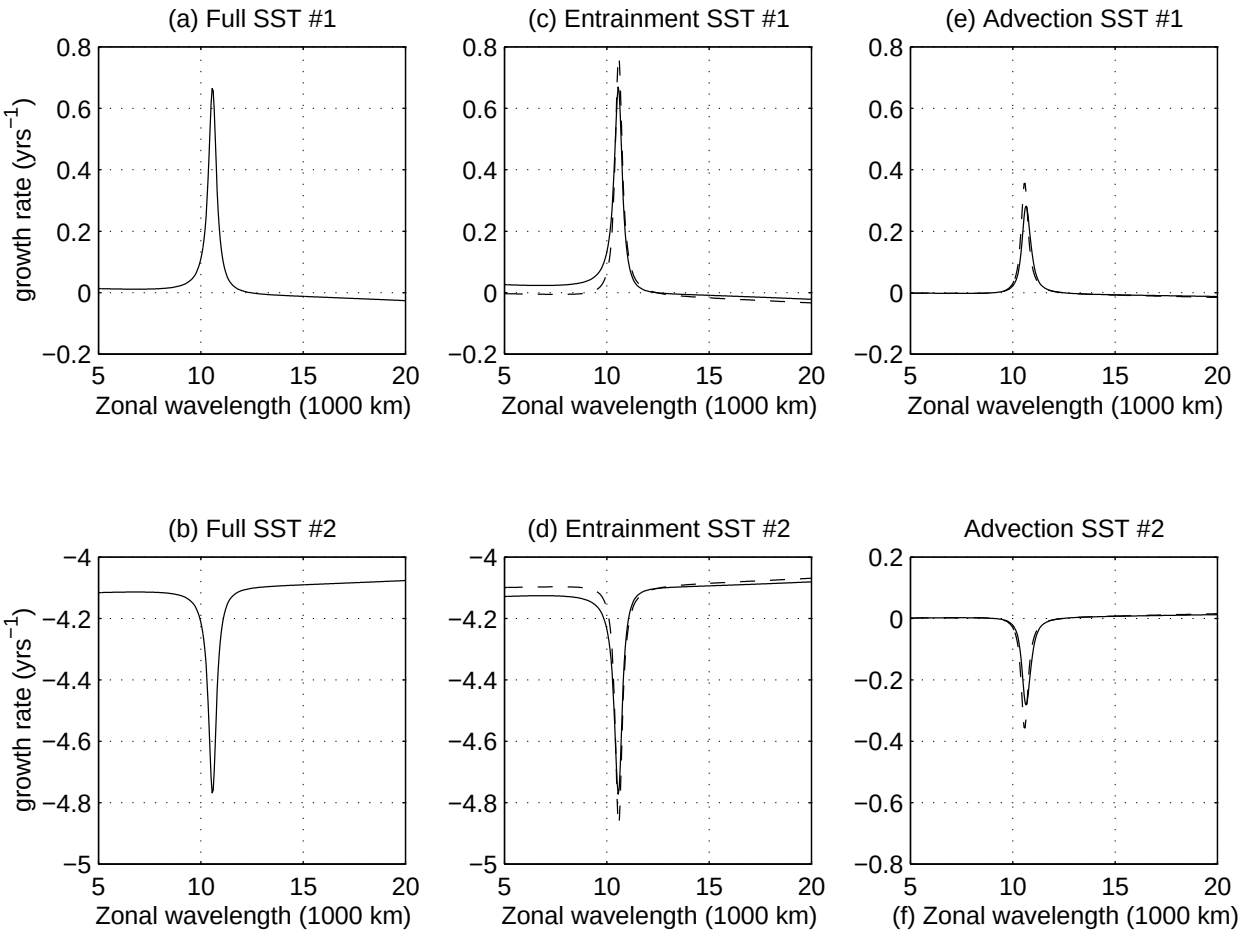

Figure 2-8: Graph of growth rate ($Im(\sigma)$) as a function of wavelength for the coupled dispersion relation (2.42) and its simplified forms. (a) and (b) are the two solutions to (2.42) given the parameters in Table 2.1. Solid lines in (c) and (d) are for (2.47), which neglects SST advection and air-sea flux; dashed lines are for the simplified forms (2.48) and (2.49). (e) and (f) are for (2.50), which neglects entrainment; dashed lines are for the simplified forms (2.51) and (2.52).

2.3.3 Growth rates

In Figure 2-8, growth rate is plotted as a function of zonal wavelength, using the values for mean winds and coupling constants given in Table 2.1. These parameters are for a "winter" simulation, in which the entrainment term is large. In (a) and (b), we show the two solutions to (2.42), which includes all terms in the SST equation. Figures (c) and (d) show the two solutions to (2.47), which includes SST entrainment and tendency, along with their approximate solutions (that is, (2.48)=(2.44) and (2.49)). Graphs (e) and (f) show the two solutions for the advection-only mode (2.50) along

Quantity	Variable	Value
Coriolis parameter	f	$1 \cdot 10^{-4}$ s^{-1}
Beta	β	$1.8 \cdot 10^{-11}$(m s)$^{-1}$
Meridional wavenumber	l	$\pi/3200$ km
Atmospheric scale height	H	10 km
Upper-layer mean wind	U_1	17 m/s
Lower-layer mean wind	U_2	8 m/s
Ocean upper layer thickness	h	500 m
Mixed layer thickness	h_{mix}	100 m
Oceanic Rossby radius	L_o	45 km
Atmospheric Rossby radius	L_a	660 km
Windstress coupling constant	α	$3 \cdot 10^{-8}$ s^{-1}
Ocean density-temperature scale factor	ε	10^{-4} K^{-1}
SST advection parameter	a	0.015 m/s
Atmospheric air-sea flux parameter	γ_a	$8 \cdot 10^{-7}$s^{-1} = 1/(14 days)
Oceanic air-sea flux parameter	γ_o	$5 \cdot 10^{-8}$s^{-1} = 1/(8 months)
Mixed-layer entrainment parameter	γ_e	$1.3 \cdot 10^{-7}$s^{-1} = 1/(3 months)

Table 2.1: Numeric parameter values

with their approximations (2.51) and (2.52).

We observe a highly scale selective growing mode with an e-folding time of 1-2 years. Only those wavelengths which allow nearly-stationary free waves to exist (i.e., $\nu \approx 0$) produce the phase matching between atmosphere and ocean and the equivalent barotropic atmospheric response necessary for the coupled growing mode. Even though the entrainment timescale $(\gamma_e)^{-1}$ is only 2.5 times faster than the air-sea interaction timescale $(\gamma_o)^{-1}$, the solution including only entrainment and tendency (solid line in (c)) or even entrainment alone (dashed line in (c)) provides a good approximation to the growth rate of the full SST equation. This latter approximation is based on the incredibly simple entrainment-dominated SST equation SST = $r_o\psi_o$ (Section 2.2.2.1).

Note that, as expected from Section 2.2.2.3, the advection-tendency SST equation exhibits growth under the same conditions as the entrainment SST equation. The entrainment mode and the advection mode are completely compatible and non-interfering, and are, in fact, nearly indistinguishable in their SST, dynamic ocean, and atmospheric patterns.

For both entrainment and advection solutions, growth is most rapid for high (low) pressure anomalies above warm (cold) water, in accord with observations of the correlation between SST and surface pressure anomalies seen in the observations and models on interannual-to-decadal timescales (see Deser & Blackmon, 1992 and Latif & Barnett, 1996).

The growth rate and phase speed of the "SST-only" mode dominated by surface heat flux (σ_2 in (2.55)) is shown in Figure 2-9. The wave propagation direction changes from eastward to westward as we cross over the wavelength of stationary free atmospheric waves, and the damping reduces to zero (because $m = 0$ when $\nu/\Gamma = 0$). We can explain the reduced damping at resonance of the SST-only mode of the full SST equation (part (b) of Figure 2-8) by noting that both entrainment and air-sea flux tend to damp SST when the system is off-resonance, but the air-sea flux shuts off at resonance.

We see, then, that both the entrainment and the advection process generate coupled growing modes with similar growth rates and nearly-identical wavelength dependence and structure (*i.e.*, Figure 2-4 applies to both). The largest term in the SST equation (the entrainment process) appears to dominate the behavior of the coupled mode for the parameters chosen here, but if we decrease γ_e (as might happen when summer begins) advection begins to dominate the growing mode. In Figure 2-10, we show the dispersion relation when $\gamma_e = 0$. The air-sea flux term does not affect the fastest growing mode (again, because m=0 there), but it does reduce off-peak growth rates, narrowing the peak width. There is a region of weak damping for wavelengths shorter than the wavelength of maximum growth: when air-sea flux is large, the phase shift between wind stress and subsurface streamfunction can be greater than 90° , so the wind torque opposes the subsurface vorticity. However, note that "wintertime" growth at this wavelength (Figure 2-8) outweighs the damping, and the solutions for an annual-average value of γ_e ($7 \cdot 10^{-8}$ s^{-1}) (not shown) show no damping region.

As one might expect, growth rates also depend on the strength of the mean zonal winds. Figure 2-11 shows contours of the growth rate of the entrainment-only solution (2.45) for $k = \pi/(5500$ km)basin-scale modes (other parameters are as in Table 2.1)

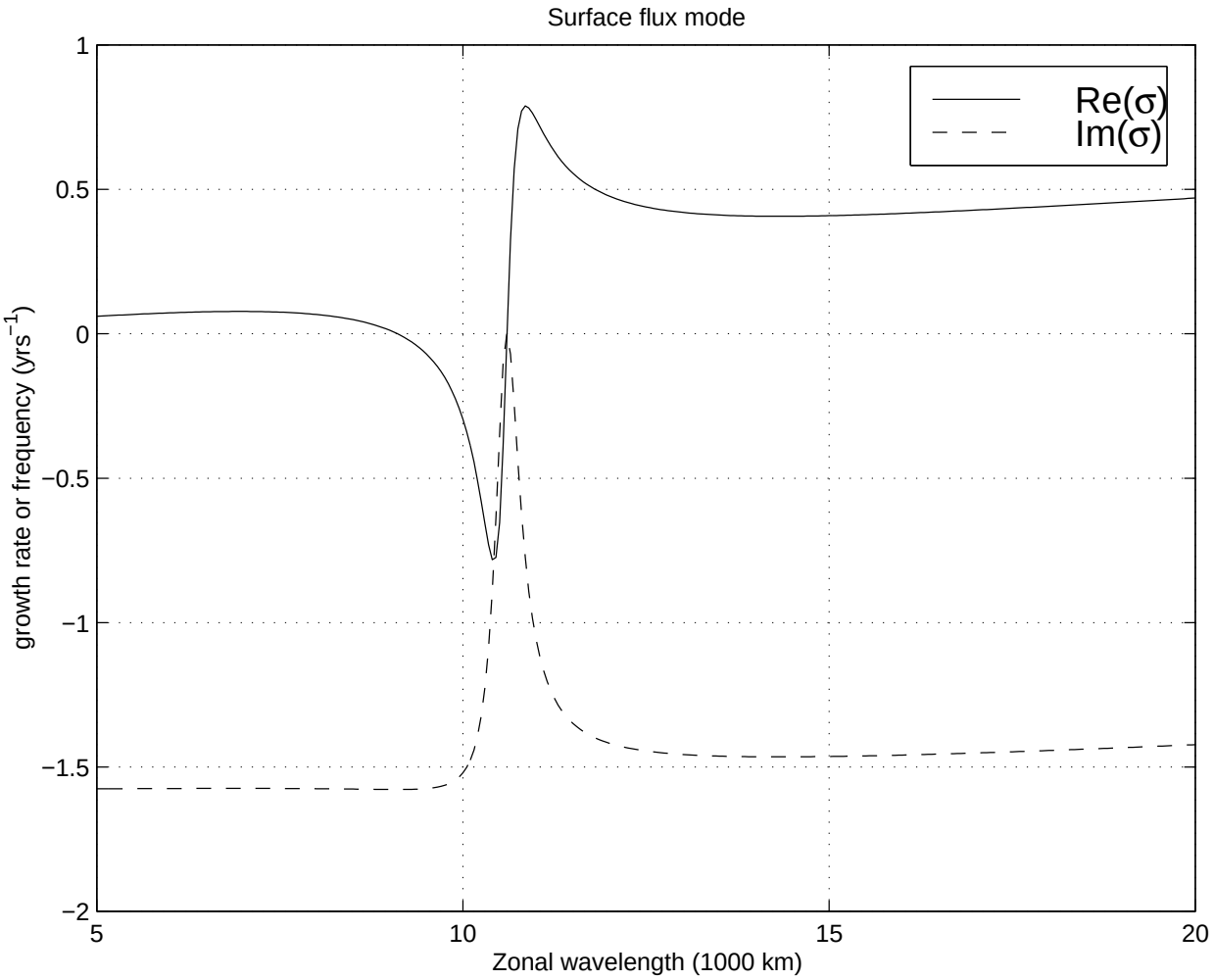

Figure 2-9: Real and imaginary parts of frequency for the "heat flux" mode discussed in Section 2.2.2.4. Note change in propagation direction and cessation of damping at resonance.

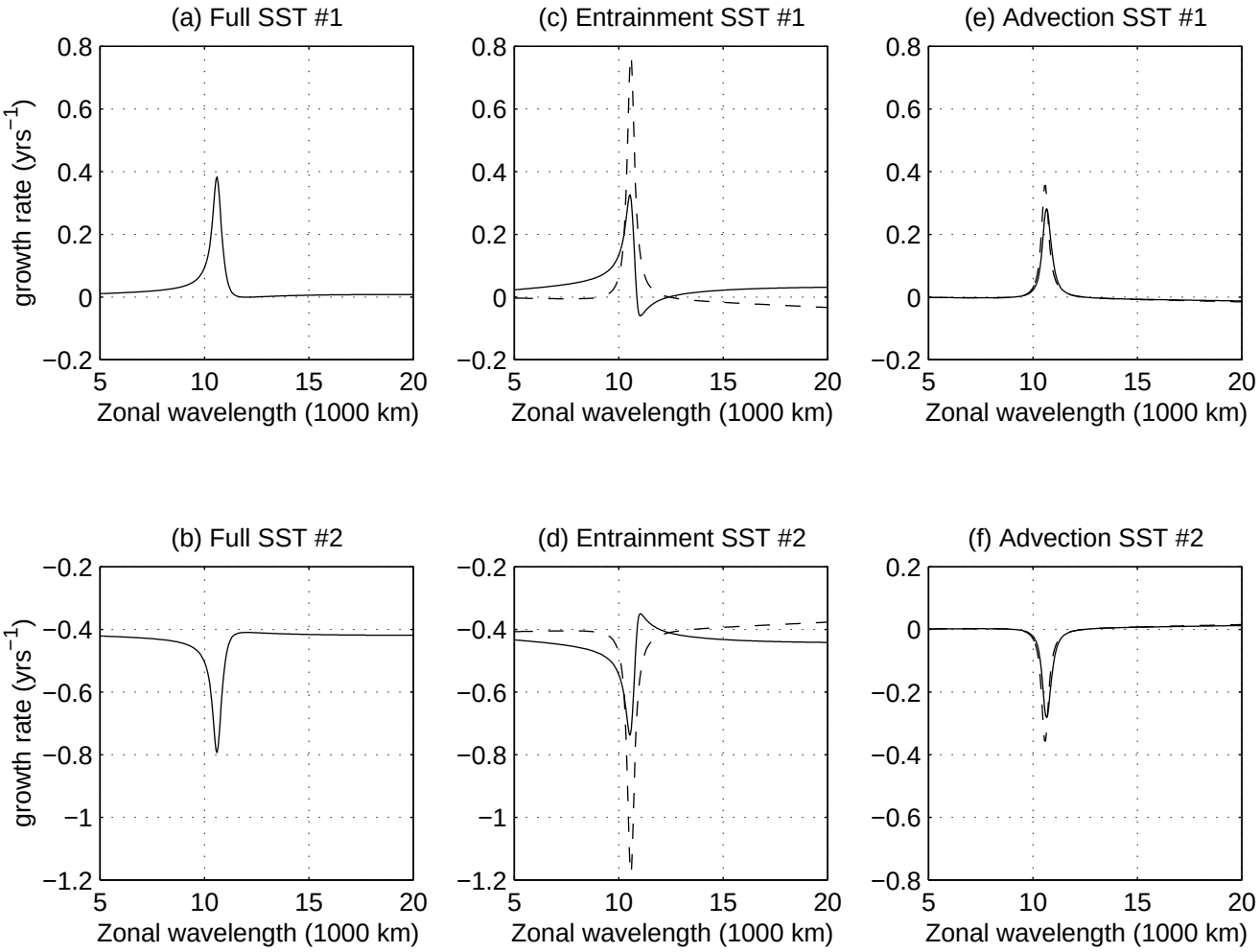

Figure 2-10: As in figure 2-8(a,b), but with zero entrainment: $\gamma_e = 0$.

as a function of baroclinic and barotropic winds. The growth rates range from years to decades for a broad range of atmospheric winds. Growth only occurs in the shaded triangle, where $\mu < -2$ (see Figure 2-7). The winds needed to fall in the growth region are consistent with those over the midlatitude oceans.

From these figures, we see that atmosphere-ocean anomalies the size of the midlatitude North Pacific or North Atlantic (commensurate with the scales of the NAO and PNA) can exhibit fluctuations of decadal period and exponential growth in our model for reasonable choice of basic state. The growth and surface expressions of these modes appear strongest in the winter, when entrainment tightly couples SST with the thermocline's structure. The model predicts equivalent barotropic atmospheric highs over warm SST, similar to that seen in observations of decadal variability (for example, Kushnir, 1994).

The largest growth rate of the coupled mode is quite rapid, with an e-folding timescale of 1.3 years. This is almost certainly fast enough to maintain the wave against dissipative processes which have not been modeled here. One might feel that growth is, in fact, *too* rapid: after all, this model suggests an increase in amplitude of $e^5 \sim 150$ in a single Rossby-wave period. However, numerous unmodeled processes will conspire to limit the growth. For example, the real coupled system certainly has important dissipative processes unmodeled here. The real ocean has time-mean currents which will try to rip the coherent Rossby waves apart before they reach large amplitude. The presence of meridional walls will limit the lifetime and therefore growth of an individual Rossby wave. Finally, in nature there are strong seasonal changes: the terms composing the SST equation vary strongly with season, as does the zonal wind pattern. The seasonal cycle is unlikely to affect the existence and propagation of the thermocline perturbations which form the "memory" of our system (since the cessation of entrainment in the summer tends to decouple the thermocline from the mixed layer), but the mode might only be expressed in the SST and atmosphere during the wintertime, restricting the growth to 6 months out of the year.

In addition to inducing growth, the coupled physics also modifies the phase-speed

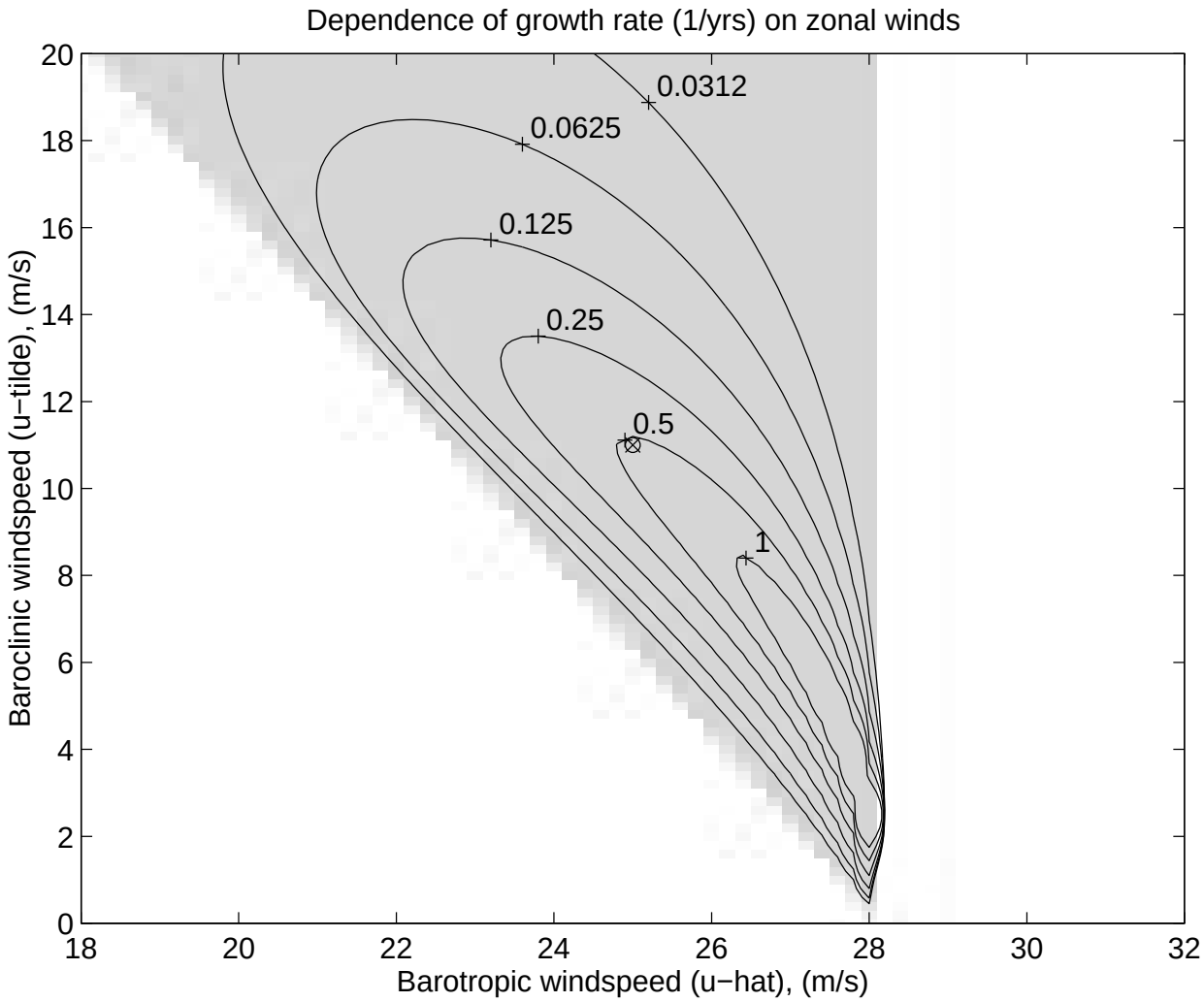

Figure 2-11: Contours of growth rate ($Im(\sigma)$) from equation (43) in years^{-1} as a function of baroclinic ($\widetilde{U} = u_1 - u_2$)and barotropic ($\widehat{U} = u_1 + u_2$) zonal mean wind speed for a particular choice of wavenumber ($k = \frac{\pi}{5500\ \mathrm{km}}$, $l = \frac{\pi}{3200\ \mathrm{km}}$.) The zonal winds used to produce Figure 2-8 are marked here with a $\otimes$.

of oceanic Rossby waves through the real part of the coupling term — see (2.42). When the atmospheric response is slightly westward, the windstress accelerates the waves toward the west, and vice versa for an eastward atmospheric response. This wave frequency shift measures only 20% of the Rossby wave speed for the parameters chosen here. Note, however that the phase speed of the fastest-growing mode is not affected at all.

2.3.4 Comparison with the Antarctic Circumpolar Wave

The Antarctic Ocean circles the globe without continents and is periodic in the zonal direction. Here the progress of oceanic Rossby waves are less impeded by meridional boundaries than in the gyre regimes of ocean basins, so perhaps the unbounded model described above is more directly applicable here than elsewhere. Let us see whether the present model can support coupled oscillations in the Antarctic Ocean.

Our previous discussions show that conditions for growth depend crucially on the sign of r and a. However, these quantities remain positive definite in the southern hemisphere despite changes in the sign of f and $\frac{\partial}{\partial y}\overline{\mathrm{SST}}$. All the results of Section 2.2 still apply. According to our model, growth of decadal-scale coupled waves could occur in the Southern Ocean if the atmospheric response to SST forcing is equivalent barotropic and if highs are located above warm water.

Recently, White & Peterson (1996) and Jacobs & Mitchell (1996) described an "Antarctic Circumpolar Wave" (ACW) which takes the form of a wavenumber-2 perturbation of SST, surface air pressure, sea-surface height, windstress, and sea ice extent, circling eastward around Antarctica with a period of around 4 years. Jacobs & Mitchell report that sea-surface height (a proxy for oceanic streamfunction ψ_o) is coincident with SST. Both White & Peterson and Jacobs & Mitchell report that windstress curl (and hence, to the extent that the geostrophic approximation is appropriate at the surface, surface air pressure anomaly) appears to lead SST by 90° phase in the observations. This configuration is summarized in Figure 2-12.

By using parameters appropriate to the Antarctic Ocean ($U_1 = 15$ m/s, $U_2 = 5$ m/s, $l = \pi/3100$ km, $\beta = 1.6 \cdot 10^{-11}(\mathrm{m\ s})^{-1}$, other parameters as in Table 2.1), we

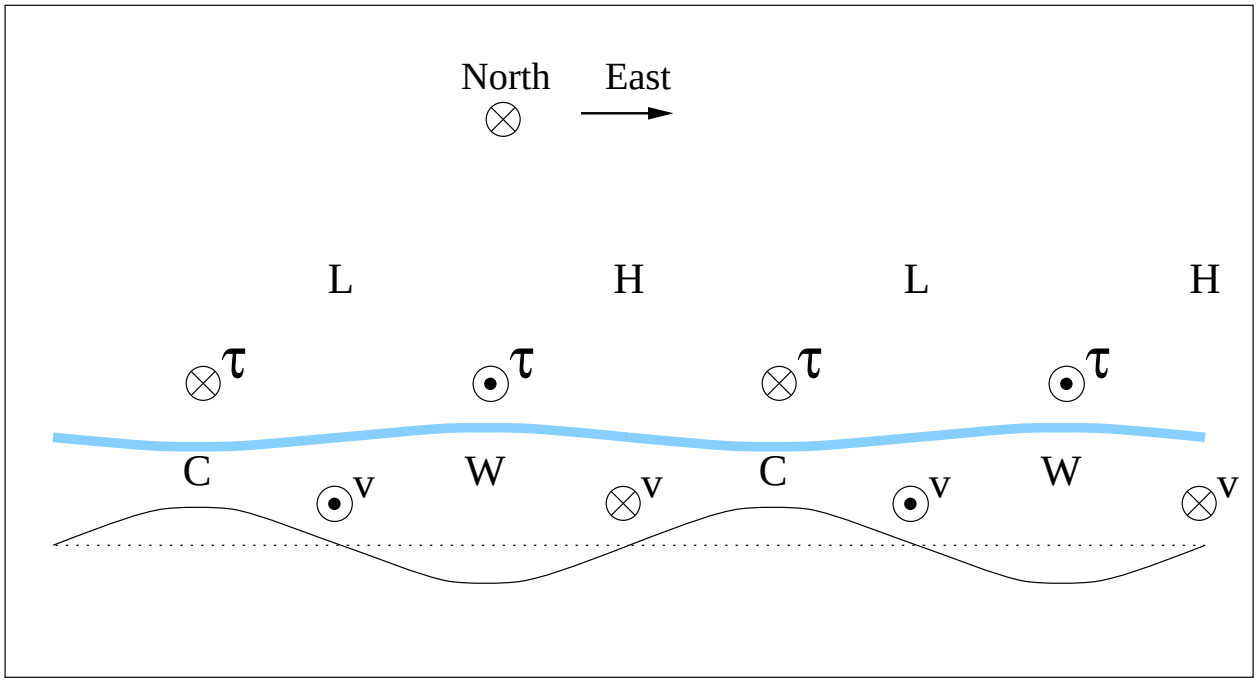

Figure 2-12: Schematic summary of the Antarctic Circumpolar Wave based on observed correlations between SST (W=warm, C=cold), atmospheric sea-level pressure (H=high, L=low),meridional wind stress (τ), and sea-surface height observed by White & Peterson and Jacobs & Mitchell. The wave encircles Antarctica with wavenumber 2, and travels eastward at 10 cm/s.

obtain a growing mode of wavenumber 2 around the globe, a growth rate of 0.35 yrs^{-1} and a westward phase speed of 4 cm/s. Our model assumes an ocean at rest: to adapt it to the Antarctic Ocean, we simply suppose our model dynamics occur in a frame moving eastward with the Antarctic Circumpolar Current at 10-15 cm/s: the resultant phase speed "over ground" for our waves is 5-10 cm/s eastward. SST, ψ_o, and $\widehat{\psi}$ are all approximately in phase.

This wave has some similarity to the ACW, but also some important differences. Phase speed and wavelength are in good agreement, as is the phase match between SST and ψ_o. However, our model predicts that the surface air pressure (and therefore wind-stress curl) should be in phase with SST. Observations of the ACW show a 90° phase shift.

Our model can produce phase-shifted growing modes in two ways. An off-resonant wave would have a significant phase shift (since $\nu/\Gamma \neq 0$) between atmosphere and ocean; such an off-resonant wave might be demanded by periodicity constraints. Furthermore, the tendency term in the SST equation (2.21) can allow the SST response to lag behind the forcing produced by the dynamic ocean. Moreover the requirement that the amplitude of SST grow over time means some phase-shifting must occur to allow the dynamic ocean to supply additional warmth to regions where SST is already large.

The model can support growing modes with phase shifts, but it is difficult to generate phase shifts much larger than 45° . In addition, we note that if the atmosphere-ocean phase shift is truly 90° , we must have $\nu/\Gamma \to \infty$ (see (2.46)), which means that the atmospheric response to SST anomalies (see (2.35)) is zero, and growth does not occur (see 2.45). While this could be an artifact of the atmospheric model chosen, we note that a 90° lag between wind-stress curl and ψ_o implies that the windstress cannot increase the amplitude of the oceanic streamfunction. The windstress is zero when the currents are maximum and vice versa, so no work is done on the current, again making growth impossible. We conclude that either the phase relationships in nature are not as the presently-available observations suggest, or the Antarctic Circumpolar Wave does not grow through windstress feedback coupling.

While preparing this paper for submission, we became aware of a study by Qiu and Jin (1997) which applies a model similar to ours to the Antarctic Circumpolar Wave. Their SST equation resembles that of Section 2.2.2.3, but allows cooling of SST anomalies by air-sea flux. They employ a greatly simplified atmosphere which ignores β-effects and Rossby waves (essentially a thermodynamic equation plus thermal wind), in which the response is assumed *a priori* to be equivalent barotropic. Their ocean dynamics and coupling assumptions are similar to ours, but with two oceanic levels and a mean zonal current. A coupled growing mode and a damped uncoupled mode are found, just as in this study. However, our use of a more dynamically-based, albeit still highly simplified, description of the atmosphere leads to differences that cannot be ignored. The meridional wavelength and zonal wind speeds chosen by Qiu and Jin are so small that any reasonable choice of the baroclinic component of the mean winds (a factor not part of their model) generates a baroclinic response in our model, with $\mu > 0$ (see (2.32)). This leads to a decaying mode in our equations. Their assumption that the atmosphere responds barotropically agrees with observations of the ACW, but it is not trivial to explain or generate such a response through atmospheric dynamics. Most importantly, however, our model and that of Qiu & Jin adopt the same mechanical forcing of the ocean by wind stress, and so theirs, like ours, must prohibit growth when wind stress curl leads oceanic streamfunction by 90° .

The model described here, that of Qiu & Jin, and the observations have their limitations. We note that Christoph and Barnett (1996) have observed an ACW in their ECHAM4 + OPYC3 coupled numerical model. Because the model may provide a continuous record of all relevant fields over many decades (particularly wind and surface air pressure fields, which are difficult to measure remotely) it may be fruitful to test our analytical model against this numerically simulated ACW.

2.3.5 Sensitivity to parameters

The parameters of our model are rather schematic and grossly represent a myriad of processes. However, in the entrainment-tendency and advection-tendency limits,

α, r, γ_e, and a, which are perhaps the most uncertain of the external parameters, appear only as multipliers to the coupled growth terms in (2.48)=(2.44) and (2.51), approximations to (2.42). As such, changing their values causes a proportional change in the growth rate of the coupled wave, but not its structure or existence. Likewise, Γ changes only the width of the peaks in Figure 2-8, which is relatively unimportant. Larger Γ implies more rapid equilibration, allowing a wider range of atmospheric waves to be in the equilibrated state.

The structure and existence of a growing coupled mode depends on μ and ν, and therefore on U_1, U_2, β, k, and l. Experimentation has shown that most reasonable midlatitude values of U_1 , U_2, l, and β result in growth at some zonal wavelength k: however, the wavelength of the fastest-growing mode is rather sensitive to the choice of these variables. By changing the zonal winds or meridional wavenumber by 20%, can change the wavelength of maximum growth in Figure 2-8 by 50% or more. Frankignoul (1985) also noticed the ease in which a 2-layer QG model can be "tuned" using the meridional wavenumber. Growing coupled modes are thus a robust feature of this model, but their precise sizes and shapes are not. This is to be expected of a simple model intended to illustrate a process rather than to simulate reality.

2.3.6 Energetics of growth mechanism

Where does the energy for growth come from? While our model does not rigorously conserve energy, we may still consider the energetics of the natural system with true mechanical and thermal energy fluxes in both air and sea, closing the energy budget. The atmosphere gains energy from the ocean through surface heat flux and loses energy through surface windstress drag. The storage of energy in the atmosphere is small, so these two processes approximately balance. The ocean therefore "sees" the atmosphere as a device which converts thermal energy (from surface heat flux) into mechanical energy (via windstress).

Consider the entrainment-dominated SST parameterization of Section 2.2.2.1. If the interface between two ocean layers with temperature difference ΔT is anomalously low by an amount Δh, that column of water has an extra amount of heat (thermal

energy) per unit area of magnitude

$$E_{th} = C_p \rho \Delta h \Delta T$$

This heat is tied to an SST anomaly and so is accessible to the atmosphere through air-sea interaction. If a nearby column has the opposite perturbation $-\Delta h$, the atmosphere can be thought of as a heat engine which removes heat from the warm patch and supplies it to the cold patch, diverting some of that heat flux to do "useful work" (i.e., generate a windstress). This windstress can increase the kinetic (E_k) and gravitational potential energy (E_p) of the ocean. Since our anomalies are much larger than the oceanic Rossby radius, $E_p \gg E_k$ (Gill, 1982). The gravitational potential energy density of the above configuration, *i.e.*, the amount of energy per unit area that must be imparted by the wind to lift an interface between fluids of density difference $\Delta\rho$ a height Δh is

$$E_p = \frac{g}{2}\Delta\rho(\Delta h)^2 = \frac{g}{2}\varepsilon\rho\Delta T(\Delta h)^2$$

where $\varepsilon = \frac{\Delta\rho}{\rho\Delta T}$, equivalent to the coefficient of thermal expansion if salinity is constant. The thermal energy contained in this anomaly is much, much greater than the energy required to make it available:

$$\frac{E_{th}}{E_p} = \frac{C_p}{(g/2)\varepsilon\Delta h} \approx 1.6 \cdot 10^5$$

for $\Delta h = 50$ m, $C_p = 4000$ J kg^{-1}K^{-1}, and $\varepsilon = 10^{-4}$K^{-1}. So if the atmospheric heat engine is just .0006% efficient at converting the lateral thermal energy difference into windstress which further lifts the interface, the coupled wave can replenish its energy store.

We thus see that the energy for growth comes from the huge amount of thermal energy stored in the thermocline, which is usually unavailable to the ocean dynamics. But the application of windstress tilts the thermocline, turning vertical thermal gradients into horizontal gradients which the atmosphere can use in a heat-engine

fashion to create a windstress which further tilts the thermocline. The atmosphere is a 'catalyst', allowing the ocean to extract energy from the vertical stratification. An identical argument holds for the meridional-advection SST equation: the energy for growth is now extracted from the mean meridional SST gradient.

2.4 Conclusion

We have described and analyzed a simple atmosphere-ocean model which supports growing coupled modes and exhibits decadal oscillations in SST, air pressure, and oceanic streamfunction. Moreover, the growth rate and form of the coupled modes have aspects in common with observations of natural variability in the North Atlantic, the North Pacific and the Antarctic Circumpolar Wave. The 'clock' of the coupled model is provided by oceanic baroclinic Rossby waves (in this manner, it resembles the model of Latif and Barnett (1994). Undulations of the sub-surface thermal field, associated with the westward-propagating baroclinic Rossby waves, exposed to the surface by wintertime mixed-layer deepening, induce SST anomalies which change the diabatic heating rates of the atmosphere and hence its circulation. The resulting anomalous winds blow over the ocean and exert a stress on it: in the growing mode, this anomalous windstress acts to amplify sub-surface undulations, leading to larger deep thermal anomalies and magnified SST anomalies, resulting in a positive feedback.

We find that the vertical structure of the atmospheric response to thermal forcing is central to the coupling mechanism. In order to support a growing mode the response *must* be equivalent barotropic, with highs above warm water. If the Doppler-shifted atmospheric Rossby wave speed is sufficiently slow, so that the time it takes to cross an SST anomaly is long compared to the thermal equilibration timescale, ($|\nu|/\Gamma \ll 1$), then thermal equilibration will occur and coupled modes grow rapidly enough to maintain themselves against dissipative processes.

Two approaches to the specification of SST were considered. In the first, SST was tied to subsurface thermal anomalies associated with vertical undulations in isotherms. In the second SST was determined by horizontal circulation across a

specified large-scale meridional SST gradient. Both 'recipes' yield growing modes with very similar structure. The former model exhibits more rapid growth for the parameters chosen in this study, and (at least for the parameters chosen here) the limit where entrainment completely dominates SST provides an excellent, simpler approximation to the full dispersion relation. Air-sea heat flux, the third important influence on SST, acts to reduce the growth rate, but does not affect the fastest-growing mode at all, because that mode has negligible air-sea temperature difference. The coupling mechanism is most active during periods of rapid entrainment (winter); the mode may become less strongly coupled and therefore "dormant" during the summer, though subsurface Rossby waves will continue to propagate during dormancy.

Comparisons of such a simple model with observations must be rather tentative. There is evidence that the response of the atmosphere to SST anomalies on interannual timescales is equivalent barotropic with highs over warm surface anomalies — see, for example, Kushnir (1994). Moreover, we find that the structure and growth rate of the fastest growing coupled mode is broadly consistent with what is known of the spatial scale, and low-frequency variability of the North Atlantic Oscillation. Our mode will be much more strongly coupled in the winter, in agreement with Hurrell & Van Loon's (1997) and others' observation that the NAO is strongest and shows greatest persistence in winter. There are also some aspects that resemble the Antarctic Circumpolar Wave, although observed air-sea phase relationships appear to differ from this model's predictions.

However, in relating this simple model to phenomena in the atmosphere and ocean, one must proceed with care. The coupling parameters α and r are poorly known, the true barotropic and baroclinic modes of the atmosphere are complicated pressure-weighted averages of vertical quantities rather than the simple two-level sum and difference used here, and quasi-geostrophy and the β-plane approximation give only qualitative guidance on such large scales, particularly near resonance. Any of the these factors could significantly change the numerical values of μ, ν and Γ.

Our use of a two-level QG atmosphere can easily be criticized. The behavior of planetary wave models is is sensitive to the upper boundary conditions. A rigid lid was

assumed here, which may overemphasize the downstream stationary-wave response by prohibiting upward transmission of wave energy (Lindzen *et al.* 1968). However, (Panetta *et al.* 1987) demonstrates that these deficiencies are not a major concern for the flows considered here. Planetary wave models are also sensitive to the vertical profile of heating (which is trivial in a 2-layer model). Our model may also be suspect near resonance, as other dynamics may become important.

Of even more importance, perhaps, are the lack of zonal asymmetries in our model. The model ocean has no meridional boundaries (there are no land masses!) and the mean flow of the atmosphere is not purely zonal. However, nearly-stationary atmospheric waves also exist in non-uniform flows. For example, Marshall & Molteni (1993) seek "neutral vectors" of the free atmosphere, and find free, almost-stationary waves that can co-exist with climatological winds. Moreover, there is a strong resemblance between some of their neutral vectors and some of the EOFs computed from ECMWF analyzed fields. One of these patterns closely resembles the NAO. In the real atmosphere, neutral vectors may take the place of the linear nearly-stationary Rossby waves that can efficiently couple with the ocean in this model. We investigate this possibility more carefully in Chapter 4.

We christen this growth mechanism a "candle instability" by analogy with a burning candle. The candle's flame feeds on the energy in the molten wax while melting more wax, ensuring a constant fuel supply, in the same way that our atmospheric model feeds on the SST anomalies, while driving a circulation which replenishes those anomalies. The candle flame and our growing mode's atmosphere also react similarly to strong atmospheric advection.

Chapter 3

Elaborations on the coupled model; the role of neutral vectors

In order to allow solution by hand, the analytical model of Chapter 2 is oversimplified in many ways. Among these are its constant zonal basic-state winds, the lack of a re-entrant atmospheric geometry, the use of only two levels in the atmosphere, the lack of coastal boundaries in the ocean, and the absence of basic-state currents in the ocean. In this chapter, we develop a model which is capable of addressing some of these problems. If we are to believe that the essential physics described in Chapter 2 operates in the real world, including these extra factors should not destroy the coupled mode. In fact, we'll see that some of these factors actually improve the model's agreement with observations. We conclude with a discussion of the atmospheric dynamics of the coupled mode, showing their connections with the resonant patterns termed "neutral vectors" by Marshall & Molteni (1993).

3.1 Elaborations upon the analytical model

3.1.1 Model equations

We restate here for convenience the system of coupled equations studied in the previous chapter:

Dynamic Ocean:

$$\frac{\partial}{\partial t}q_o + \beta\frac{\partial}{\partial x}\psi_o = \alpha\nabla^2(\frac{3}{2}\psi_2 - \frac{1}{2}\psi_1) \tag{3.1}$$

Atmosphere (upper level)

$$J(\psi_1, Q_1) + J(\Psi_1, q_1) = \frac{\gamma_a}{L_a^2}\left((\psi_1 - \psi_2) - \mathrm{SST}/r_a\right) \tag{3.2}$$

Atmosphere (lower level)

$$J(\psi_2, Q_2) + J(\Psi_2, q_2) = -\frac{\gamma_a}{L_a^2}\left((\psi_1 - \psi_2) - \mathrm{SST}/r_a\right) \tag{3.3}$$

SST

$$\frac{\partial}{\partial t}\mathrm{SST} = -\gamma_o(\mathrm{SST} - r_a(\psi_1 - \psi_2)) - J(\psi_o, \overline{\mathrm{SST}}) - \gamma_e(\mathrm{SST} - r_o\psi_o) \tag{3.4}$$

In the above, Ψ_1 and Ψ_2 are the basic-state atmospheric streamfunctions; ψ_1, ψ_2, ψ_o are the streamfunction anomalies in the upper and lower atmospheric layers and in the ocean; Q_1 and Q_2 are the basic-state atmospheric PV fields; and q_1, q_2, and q_o are the QG potential vorticity anomalies in the same layers. $\overline{\mathrm{SST}}$ and SST are the unperturbed and anomalous sea-surface temperature; the forcing term on the right side of equation (3.1) is the mechanical forcing of the ocean by the winds extrapolated down to the surface (α is a drag coefficient); the right-hand sides of equations (3.2) and (3.3) represent a baroclinic thermal forcing via relaxation of the atmospheric temperature anomaly (expressed using $\psi_1 - \psi_2$ through the thermal wind equation) to a value set by SST; and the forcing terms for SST represent air-sea heat flux, advection of the mean SST gradient, and entrainment, in that order. The parameters r_a and r_o are conversion constants for translating streamfunctions into temperatures via the thermal wind equation, in the atmosphere and ocean respectively.

This is a coupled system in four unknowns (ψ_1, ψ_2, ψ_o, and SST) and four equations. In the previous chapter,, we assumed that Ψ_1, Ψ_2, Q_1, and Q_2 were linear functions of the meridional coordinate (i.e., the basic-state flows were constant and

purely zonal). This makes the system linear and constant-coefficient, allowing plane-wave solutions in an unbounded domain.

We now attempt to generalize these solutions to a periodic atmosphere domain with a possibly-restricted ocean basin, allowing nonuniform atmospheric flows. We will not consider here the important case of nonzero basic-state ocean currents.

3.1.2 Discretization

For arbitrary basic states, this equation must be solved numerically. We do this by forming finite-difference forms of the equations above. There are a couple of caveats in doing so, though.

First, in the ocean equation, we must disallow flow through the ocean boundaries; we do this by specifying that $\psi_o = 0$ everywhere on the boundary.[1] But equation (3.1) is first-order in space, and so cannot satisfy this condition; we must introduce a term which allows a frictional boundary layer on the western edge of the basin. We're not much interested in the detailed boundary layer structure, so we choose a Stommel (1948) frictional term as the simplest possible choice:

$$\frac{\partial}{\partial t} q_o + \beta \frac{\partial}{\partial x} \psi_o = \alpha \nabla^2 (\frac{3}{2}\psi_2 - \frac{1}{2}\psi_1) - \epsilon \nabla^2 \psi_o$$

Second, we must be very careful to conserve PV exactly in the discretized atmospheric equations. We write the left-hand-side advection operators in "flux form":

Atmosphere (upper level)

$$\nabla \cdot (\mathbf{v_1} Q_1) + \nabla \cdot (\mathbf{V_1} q_1) = \frac{\gamma_a}{L_a^2} ((\psi_1 - \psi_2) - \mathrm{SST}/r_a) \tag{3.5}$$

[1] ψ_o =constant is sufficient to disallow flow through boundaries. Technically, since streamfunction is proportional to layer thickness, the constant should be chosen at each timestep to conserve upper-layer fluid volume globally. We sidestep this detail by setting the meridional width of the model equal to one full wavelength of the coupled mode described in Chapter 2. A meridionally antisymmetric layer thickness perturbation does not change the volume within the layer, since for every high there's a corresponding low. Thus, the boundary constant can remain zero at each timestep, and in practice we find that the mean layer thickness remains nearly constant.

Atmosphere (lower level)

$$\nabla \cdot (\mathbf{v_2} Q_2) + \nabla \cdot (\mathbf{V_2} q_2) = -\frac{\gamma_a}{L_a^2} \left((\psi_1 - \psi_2) - \mathrm{SST}/r_a \right) \tag{3.6}$$

These equations are differenced in such a way that the flux entering through each face of a square box of area $4dxdy$ equals the flux leaving the adjoining box.

We must also add a small amount of vorticity diffusion and dissipation of PV anomalies into the model atmosphere for numerical stability.

The model is discretized using a standard finite-difference scheme, with ψ- and q-points coincident, and using a centered difference scheme for first derivatives. We specify a periodic channel geometry in the atmosphere whose zonal and meridional extents are 25,000 km and 7,200 km respectively. The north and south boundary conditions in the atmosphere are designed to allow no PV flux through the walls. The meridional grid spacing is 360 km; the zonal grid spacing is 550 km in the atmosphere and 275 km in the ocean.[2]

Upon discretization, the SST and ocean streamfunction equations can be written in the form

$$\frac{\partial}{\partial t} \begin{bmatrix} \mathbf{SST} \\ \mathbf{\Psi_o} \end{bmatrix} = \mathsf{P} \begin{bmatrix} \mathbf{\Psi_1} \\ \mathbf{\Psi_2} \\ \mathbf{SST} \\ \mathbf{\Psi_o} \end{bmatrix} \tag{3.7}$$

where $\mathbf{SST}$, $\mathbf{\Psi_o}$, $\mathbf{\Psi_1}$, and $\mathbf{\Psi_2}$ are vectors containing the discretized elements of the SST, ocean streamfunction, and atmospheric upper- and lower-layer streamfunction anomaly fields. The matrix P is a sparse matrix representing the finite-differenced forms of the differential operators in (3.1) and (3.4). We must find $\mathbf{\Psi_1}$ and $\mathbf{\Psi_2}$ using

[2]To ensure numerical stability, the western boundary current must be resolved. To do this without using a gigantic drag coefficient ϵ, we must increase the resolution in the ocean beyond what is required by the atmosphere. A simple two-point averaging/interpolation scheme is used to switch between the coarse and fine grids. Calculation of the ocean parts of the equations is cheap compared to the inversion required to solve for the atmospheric state, so this increase in ocean resolution is gained at negligible computational cost.

the side constraints provided by (3.5) and (3.6):

$$\mathbf{M}\begin{bmatrix} \mathbf{\Psi_1} \\ \mathbf{\Psi_2} \end{bmatrix} = \frac{\gamma_a}{L_a^2 r_a}\begin{bmatrix} -\mathbf{SST} \\ \mathbf{SST} \end{bmatrix} \tag{3.8}$$

where $\mathbf{M}$ is a matrix incorporating discretized forms of the advection and dissipation operators acting on the atmospheric state vectors.

3.1.3 Time evolution and eigenspectrum

We can step the system forward in time by inverting (3.8) to find $\mathbf{\Psi_1}$ and $\mathbf{\Psi_2}$ at each timestep from **SST**, then plugging those into (3.7) to get the rate of change of **SST** and $\mathbf{\Psi_o}$, which can then be advanced to the next timestep using a simple Euler forward scheme.

We can also solve for the eigenvectors of the system; this allows us to compute frequencies and growth/decay rates for the coupled mode, as done in the previous chapter. Conceptually, we imagine inverting (3.8) for $\mathbf{\Psi_1}$ and $\mathbf{\Psi_2}$, and then plugging the result into (3.7). The result is

$$\frac{\partial}{\partial t}\begin{bmatrix} \mathbf{SST} \\ \mathbf{\Psi_o} \end{bmatrix} = \mathbf{P}\begin{bmatrix} \frac{\gamma}{L_a^2 r_a}\mathbf{M}^{-1}\begin{Bmatrix} -\mathbf{I} & 0 \\ \mathbf{I} & 0 \end{Bmatrix} \\ \begin{Bmatrix} \mathbf{I} & 0 \\ 0 & \mathbf{I} \end{Bmatrix} \end{bmatrix}\begin{bmatrix} \mathbf{SST} \\ \mathbf{\Psi_o} \end{bmatrix} \equiv \mathbf{R}\begin{bmatrix} \mathbf{SST} \\ \mathbf{\Psi_o} \end{bmatrix}$$

This gives the tendency of the model state as a linear function of the model state. The eigenvectors of the $\mathbf{R}$ matrix are the exact analogues of the modes in Chapter 2, and the associated complex eigenvalues give frequencies and growth rates of each mode.

In practice, the inverse of $\mathbf{M}$ is a large dense matrix, and is thus expensive to compute and store. Instead of computing $\mathbf{R}$ explicitly, we can write a subroutine to perform the algorithm described previously: Input a (**SST**,$\mathbf{\Psi_o}$) vector, solve (3.8) for ($\mathbf{\Psi_1}$, $\mathbf{\Psi_2}$), then plug that into (3.7) to find the tendency of (**SST**, $\mathbf{\Psi_o}$). This

algorithm comprises a linear operator which does exactly what the explicit matrix **R** does. The Arnoldi (Lehoucq *et al.* 1998) algorithm is an efficient way of computing the eigenvectors and eigenvalues of a linear operator; that operator need not be an explicit matrix, but can be specified as a "black-box" algorithm of the sort outlined above.

In addition, the Arnoldi technique can solve for a *small number* of eigenvalues of desired characteristics, rather than finding the entire eigenspectrum. In our case, coupled modes which are rapidly damped are uninteresting: they will disappear rapidly from the natural system and not be observed. Growing or very slowly damped modes, however, will tend to persist in nature. Thus, we should look for the eigenvalues with most positive real part.

By never computing the inverse of the **M** matrix and by looking only for the eigenvalues of interest, this computation becomes soluble in a few minutes on a desktop Linux workstation running Matlab.

3.1.4 Channel model

We begin by running the model with a zonally-periodic channel ocean (no continents) and uniform zonal winds in the upper and lower levels of 5 and 14 m/s, respectively. This situation is similar to the analytically-soluble model in Chapter 2, except for the channel geometry and a slightly different value of basic-state winds – this allows us to compare the models. If a meridional wavelength the width of the channel is assumed, the analytical model predicts a fastest-growing mode with a growth rate of .37/year, a period of 7 years, and a zonal wavenumber of 3.1.

Figure 3-1 shows the time-evolution of the model. The model is initialized with random numbers for the ψ_o and SST fields, and integrated forward with a 30-day timestep for 55 years. The upper four panels of Figure 3-1 show a snapshot of anomalies of upper and lower layer atmospheric streamfunction, SST, and ocean streamfunction. A wavenumber 3 mode is readily apparent; atmospheric pressure and SST are only slightly out of phase (we will explain this shortly), and pressure anomalies are equivalent barotropic. The Hovmoeller diagrams in the lower left show westward

propagation of SST anomalies and of lower-level atmospheric perturbations. The lower right panel shows a local 6-year oscillation caused by the model's propagating Rossby waves, and a growth rate of about .17 per year.

Why are atmospheric anomalies not perfectly in phase with SST, as predicted by the analytical model? Why are growth rates smaller than the maximum predicted? The ideal growing mode of the analytical model has a wavenumber of 3.1. This will not satisfy the numerical channel model's periodic boundary conditions. At wavenumber 3 (the nearest integral wavenumber to the ideal mode), the results of Chapter 2 predict a growth rate of .13 per year, and a small phase offset between atmosphere and ocean – the atmosphere no longer perfectly demonstrates equilibrated mode behavior.

Thus, when the effects of a periodic channel are considered, agreement between the analytical model and the numerical model is nearly perfect; this validates the numerical code.

We note in passing that, as we speculated in the previous chapter, this phase-shift caused by the integer-wavenumber constraint enables the model to come close to success in simulating the "Antarctic Circumpolar Wave", or ACW (White & Peterson, 1996; Jacobs & Mitchell (1996)), a wavenumber-2 pattern of interannual variability in the Southern Ocean which displays a 90-degree phase shift between sea-level pressure and SST. However, as noted previously, a truly 90-degree phase shift is inconsistent with growth in this model; either the phase shift in nature must be somewhat less than 90 degrees, or our coupling mechanism is not active in ACW dynamics.

Next, we display the eigenvalues and eigenvectors of the tendency matrix (Figure 3-2). Each pair of eigenvalues has a pair of eigenvectors which are identical but for a 90° phase shift; phase propagation is always westward. There is exactly one complex-conjugate pair of eigenvalues with positive real part (implying growth) in this model. The structure of one of the eigenvectors associated with this pair is shown in the figure: it has the structure seen in the forward model run. The damping rates of the other eigenmodes are determined by the vorticity dissipation in the ocean model: mutual atmosphere-ocean feedback is relatively unimportant to their evolution.

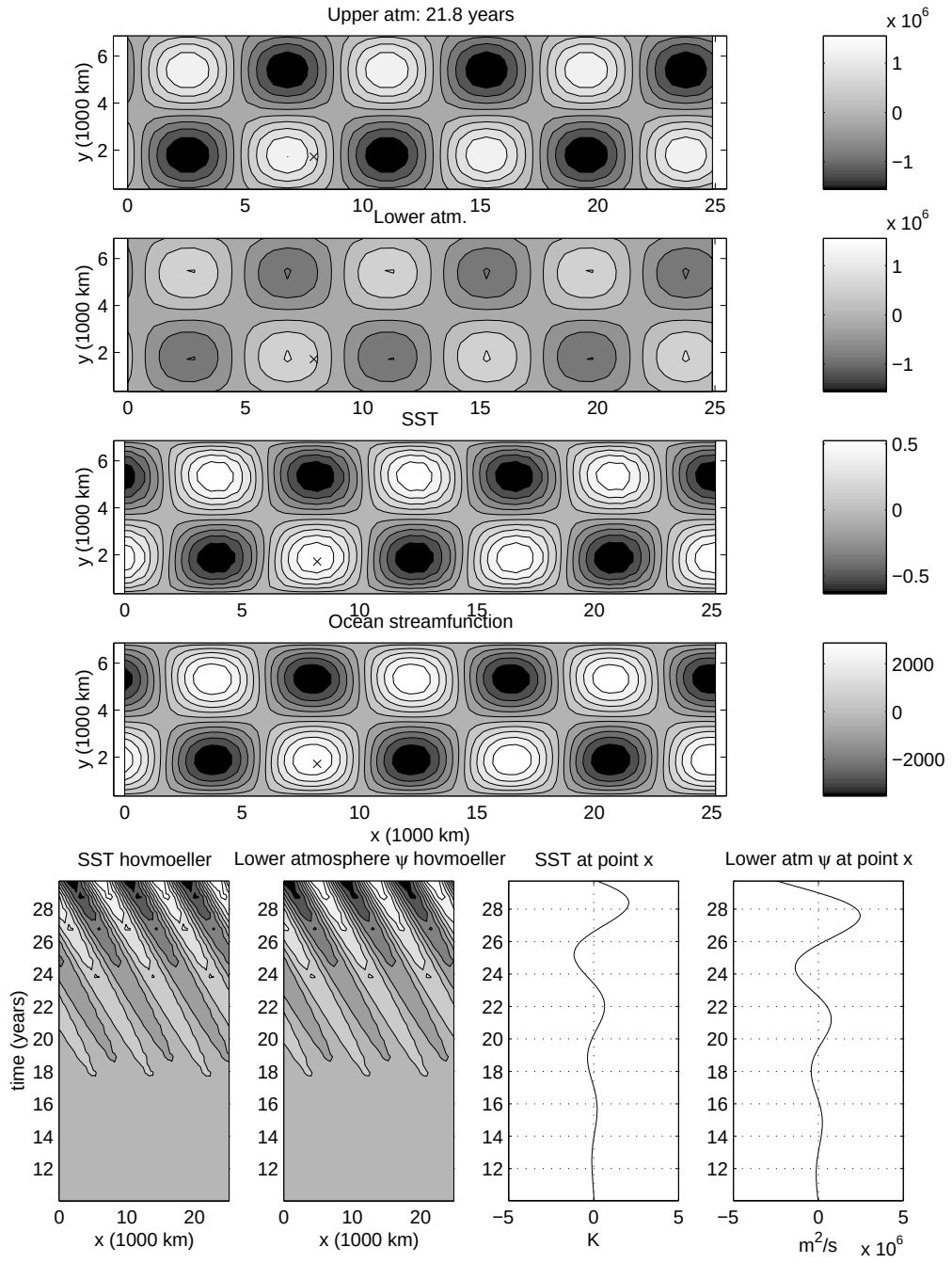

Figure 3-1: Snapshots and evolution of the numerical model, run in channel configuration. The upper two frames show the upper and lower atmospheric streamfunction anomalies (ψ_1,ψ_2) in m^2/s, with identical contour spacing in both frames. Below them are the SST anomalies, in K, and ocean streamfunction anomalies, in m^2/s. The lower left pair of panels show time-longitude sections of SST and ψ_2, taken at the latitude of the small "×" in the upper panels. The bottom right figure shows a timeseries of SST and ψ_2, taken at the ×.

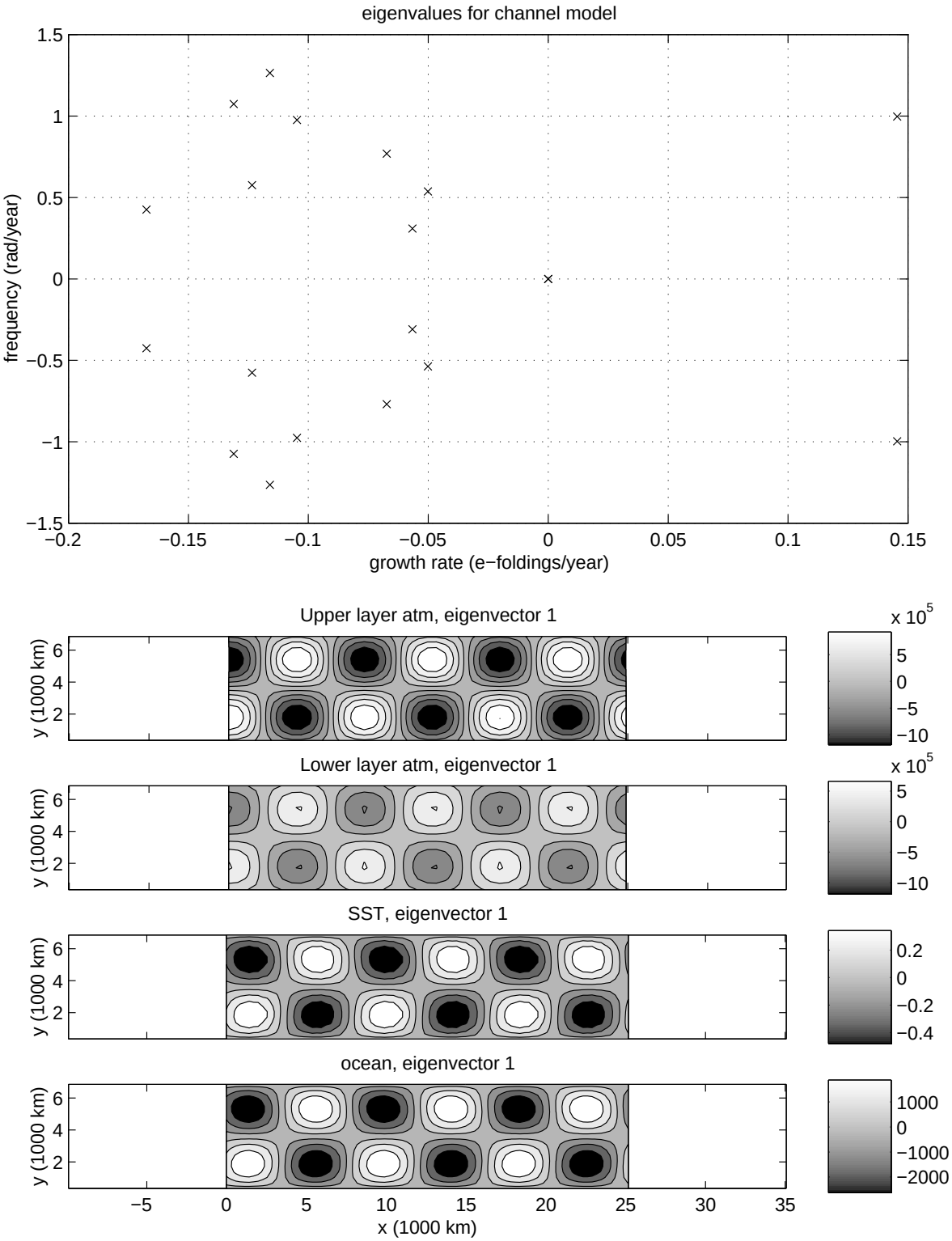

Figure 3-2: Upper panel: Eigenvalues of the coupled model's tendency matrix. Model parameters are identical to Figure 3-1. Lower panels: Real part of eigenvector associated with the eigenvalue with largest real part.

3.1.5 Ocean basin

For our first attempt at extending the model beyond the constraints of the analytical model, we restrict the ocean domain to a basin 6000 km wide. The atmosphere is still a 25,000 km zonally-reentrant channel. We define the surface temperature anomaly which forces the atmosphere to be zero for land points: only the ocean induces coupled variability. We refer to this setup as the "single-basin model".

We expect the coupled mode to be weaker for two reasons: first, only 1/4 of the surface area of the model is generating a coupled feedback; and second, the western ocean boundary strongly damps the propagating Rossby waves which embody the memory of the coupled system.

Figure 3-3 shows the eigenvalues of the single-basin model, along with the eigenvector corresponding to the rightmost eigenvalue pair. We see clearly that all eigenvalues have been shifted leftward, signifying damping. This leftward shift corresponds to a damping rate of roughly 1/(2.5 years). There is no longer a coupled growing mode, due to the strong damping caused by western boundary dissipation. However, observe the structure of the rightmost, "least-damped" mode. It displays barotropic wavenumber-3 structure in the atmosphere with matching wavelengths in the ocean, and high pressure over warm water – precisely the arrangement which grows most quickly in the analytical model.

The process by which damping occurs is easy to understand. A warm SST patch at the western side of the basin will generate the wavenumber-3 pattern characteristic of the atmosphere's equilibrated mode. This pattern will provide a windstress forcing at the eastern side of the basin which creates a cool "child" SST anomaly to the west of the "parent". For a growing mode to occur, the parent must bring the amplitude of the child up to its own amplitude before the parent is destroyed at the western boundary. This condition cannot be met with the choice of so narrow a basin (we have found that the critical basin width for these parameters is about 15,000 km), and so each parent produces a child weaker than itself, and the mode gradually dies away.

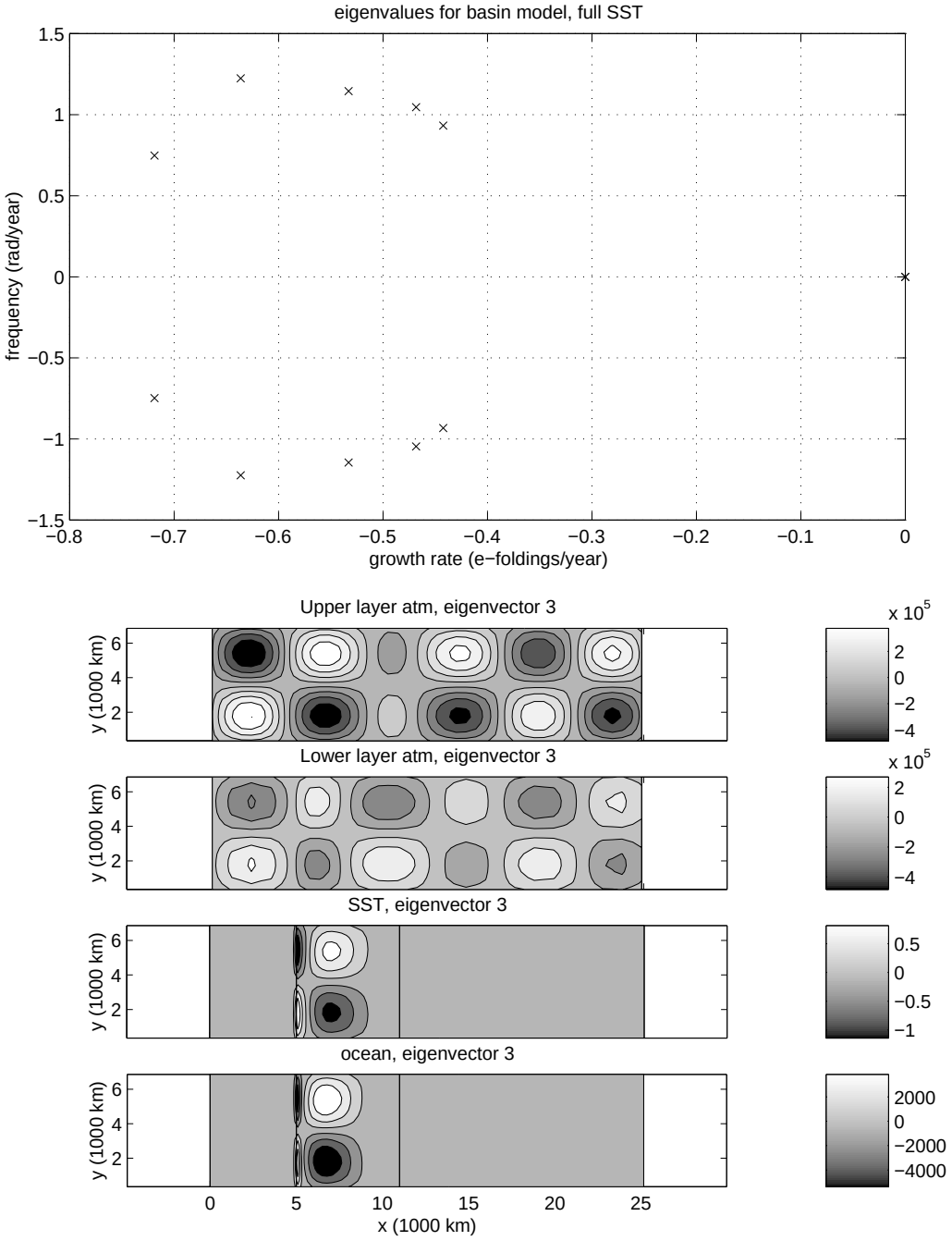

Figure 3-3: Same as 3-2, but for a single ocean basin 6000 km wide

There are now no growing modes in this system; it is universally damped. However, if this system is excited with white stochastic forcing (as from atmospheric synoptic eddies), the least-damped mode should retain the most energy, and be the most prominent. Thus the physical interaction described in Chapter 2 remains important in understanding the behavior of the present system. We will test this claim in section 3.1.7.

The NAO and other observed patterns do not exhibit rapid growth and pure-tone oscillations; instead, the NAO's timeseries spectrum (Hurrell & Van Loon, 1997) is predominantly reddish, with some apparent enhancement of power at interannual frequencies, similar to what would be produced by the present model when stochastically forced. In the previous chapter, we noted the unrealistically rapid growth, and speculated that unmodeled damping processes would counteract it. Here, we find that this is indeed the case.

One thing to note is that localization of anomalous SST forcing does not localize the atmospheric response, which remains global. This is in apparent contradiction to the identification of NAO and PNA patterns in the real atmosphere, which appear to be confined to ocean basins, or at least hemispheres. However, most papers which identify the NAO and PNA (Hurrell, 1995, Cayan, 1992) identify them as patterns of correlation with one or two points in an ocean basin, or else as EOFs of variability over an ocean basin or the eastern/western hemisphere. Global-scale EOF analysis (Wallace and Thomson, 1998) produces less restricted patterns – see Appendix B for a comparison of EOF computations in global and sectorial domains. Alternatively, the uniformity of our atmospheric background flow may incorrectly allow atmospheric Rossby waves to circle the planet without impediment.

This global influence leads to a rather unusual result when *two* ocean basins are placed within the domain (figure not shown). The same wavenumber-3 pattern appears in the atmosphere; the Rossby wave and SST patterns in the two ocean basins vary *synchronously*, since both are forced to couple to the same atmospheric pattern. It seems unlikely that such large-scale synchronous evolution should occur in reality. However, Meehl & Arblaster (1998) and White & Cayan (1998) find decadal fluctu-

ations in SST and surface pressure which vary in sync between Pacific and Atlantic in observations and coupled models.

3.1.6 Varicose atmospheric background flow

Next, we attempt to study the effect of a more realistic atmospheric background flow on the model physics. One possible way to do this would be to simply insert an observed basic-state flow in for the two atmospheric levels. However, the state used would be dependent on the map projection used to place the data in a cylindrical channel; the extremely simple geometry of the model atmosphere (especially the use of only two vertical levels and the use of solid walls to north and south) would probably negate any accuracy of simulation gained by using a realistic flow; and most important, it would be difficult to identify which of the various wiggles in the atmospheric state was causing a particular effect. Thus, we proceed with a schematic formulation for the atmospheric stationary wave pattern.

In general, the midlatitude atmospheric flow at intermediate height exhibits a jet which constricts over the western shores of the Atlantic and Pacific, and is spread out over the eastern shores of the basins. We schematize this pattern by specifying a basic-state wind field which looks like Figure 3-4. The zonally- or meridionally-averaged wind speed is constant and identical to the values used in the previous experiments.

Figure 3-5 shows the evolution of the model with an ocean basin identical to that in Section 3.1.5, and with basic-state winds as shown in Figure 3-4. Perturbations decay to zero, as before, due to the destruction of oceanic anomalies at the western boundary. Oscillation and damping rates are similar the single-basin model, and the atmospheric wave pattern again generally shows barotropic wavenumber-3 behavior, although there are now some more complicated details to the atmospheric response. The atmospheric wave no longer propagates westward in phase with SST anomalies; instead, it remains more or less fixed at a particular longitude, and fluctuates in sign. The non-uniform background flow locks the atmospheric response to a particular longitude – intriguingly, its maxima lie just eastward of the basin's center, which is

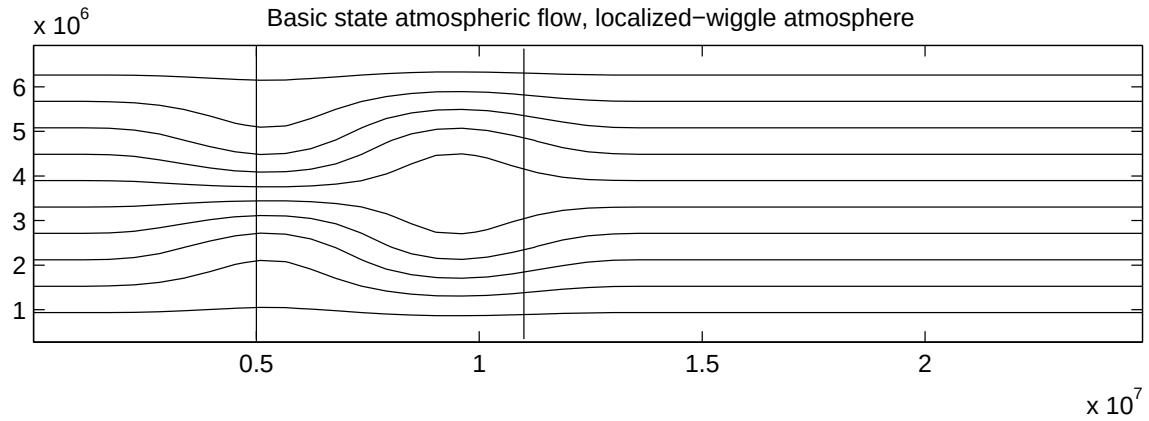

Figure 3-4: Basic-state streamfunction pattern used in the varicose background flow experiment. The basic-state streamfunction is given by the relation $\psi = U_0 y + 0.1 \cdot U_O(L_y/2)F(x,y)$, where $F(x,y) = \sin(2\pi y/L_y)\sin^2(\pi y/L_y)\sin(4\pi(x - x_0)/L_x)\sin^2(2\pi(x - x_0)/L_x)$ when $x > x_0$ and $x < (L_x/2 + x_0)$, and $F(x,y) = 0$ elsewhere. U_O is the wind velocity in either level from the uniform-flow experiment, x_0 is 10^6 m, and L_x and L_y are the zonal and meridional extents of the channel.

just where the NAO's centers of action lie.

The SST pattern of this system is more complex than the simple propagating wave pattern of previous experiments, but generally shows westward-propagating patches of warm and cool water.

3.1.7 Response to stochastic forcing

In Section 3.1.5, we noted that when confined to a basin, the coupled mode was no longer growing, but remained the least-damped mode. We stated that the least-damped mode would be most susceptible to excitation by stochastic forcing. In this section, we verify this claim.

We consider the case of a varicose background atmospheric flow over an ocean basin, as in Section 3.1.6, and compute a long forward evolution of the model, as in Figure 3-5. But now, at each timestep, after computing the atmospheric response to SST (ψ_1, ψ_2), we randomly generate an additional stochastic streamfunction component (ψ_{1s}, ψ_{2s}), add it to the response, and use the result to force the dynamic ocean and SST parts of the coupled model (3.1, 3.4).

The stochastic component of the atmospheric fields are chosen to very roughly

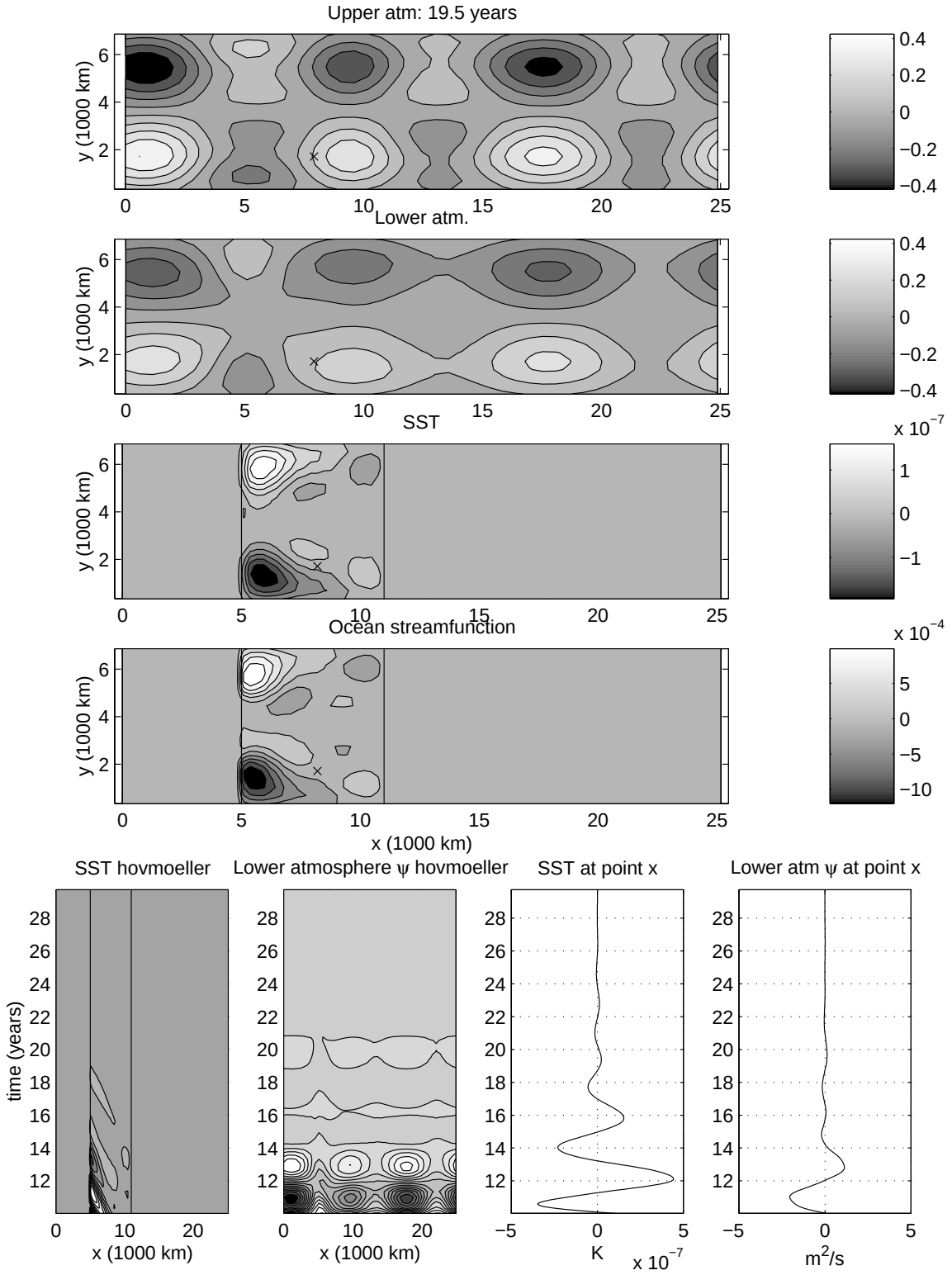

Figure 3-5: Same as for Figure 3-1, but with a varicose atmospheric background flow as pictured in Figure 3-4. The small amplitude of the wave in all fields is of no consequence, since the model is linear.

mimic the structure and amplitude of transient eddies in the atmosphere. At each model timestep (Δt =1 month) we generate a Gaussian random streamfunction field, spectrally truncated to zonal wavenumber 8 and meridional wavenumber 3. Thus the smallest wavelengths are around 3000 km. We multiply this by $\sin(\pi y/L_y)^{0.7}$ to bring the eddy amplitude to zero at the northern and southern walls, thus avoiding boundary condition problems. We multiply this field by an amplitude factor of 180 geopotential meters in the upper layer and 120 geopotential meters in the lower layer, to create an equivalent barotropic streamfunction pattern. These fields drive the ocean through air-sea heat flux term and wind-stress curl.

In Figure 3-6, we show snapshots of the model state, and its evolution through time. The atmospheric components plotted here are only the deterministic responses to SST; the additional random component is not shown in these figures.

As we would expect, the stochastic model's evolution is much less orderly. However, the patterns of atmospheric response show the wavenumber-3 by wavenumber-1 mode previously identified as a coupled mode, though the resemblance is not always as strong as in this snapshot. SST anomalies show westward propagation, and both atmospheric and oceanic variables show strong interannual variability. The amplitude of SST anomalies is of order a degree or so, with atmospheric responses of a few tens of geopotential meters; these amplitudes are very similar to the amplitudes of observed coupled interannual Atlantic variability (Czaja & Marshall, 2000b).

To more clearly isolate the dominant patterns of variability, we perform an EOF analysis on the upper atmospheric streamfunction field. The first two EOFs are shown in Figure 3-7. The first EOF explains 55% of the *non-stochastic part* of the atmospheric variability; the second EOF explains 35%. The first EOF shows a predominantly zonally-symmetric pattern, with no clear temporal structure and only a weak covarying oceanic pattern (not shown). This mode reacts strongly to SST anomalies, but is unable to excite a mutually-coupled interaction. We will revisit this pattern in Section 3.2. The second EOF is much more interesting. It shows a wavenumber-3 structure identical to the least-damped coupled mode, as well as fairly regular oscillations with a period of about 5 years. The amplitude of this mode is

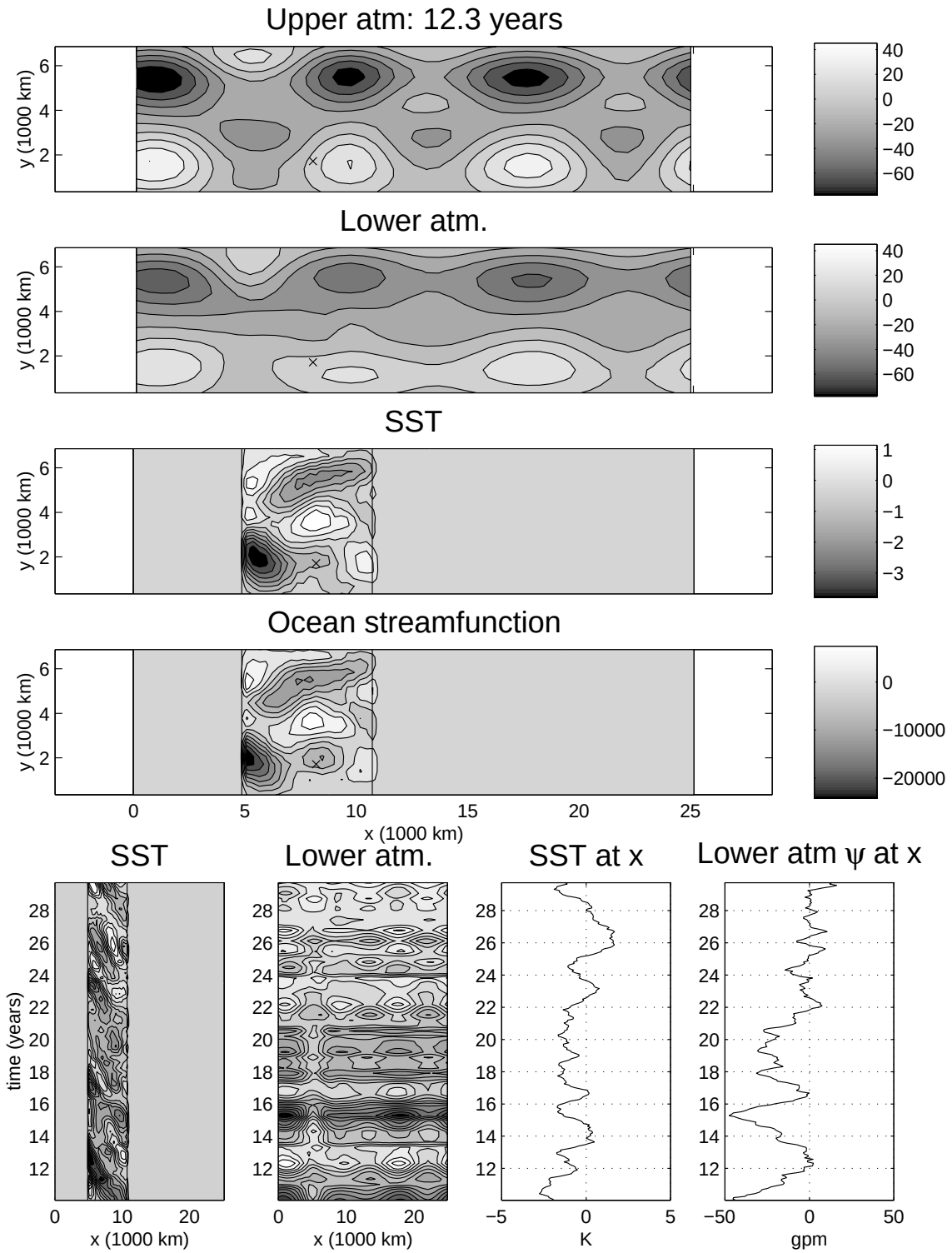

Figure 3-6: Same as Figure 3-5, but with stochastic forcing added. Amplitude of stochastic atmospheric perturbations is 180 geopotential meters in upper layer, 120 gpm in lower layer. Only the deterministic part of the atmospheric perturbation is shown here. Units of atmospheric perturbations are gpm; units of SST are K, units of ocean streamfunction are m^2/s.

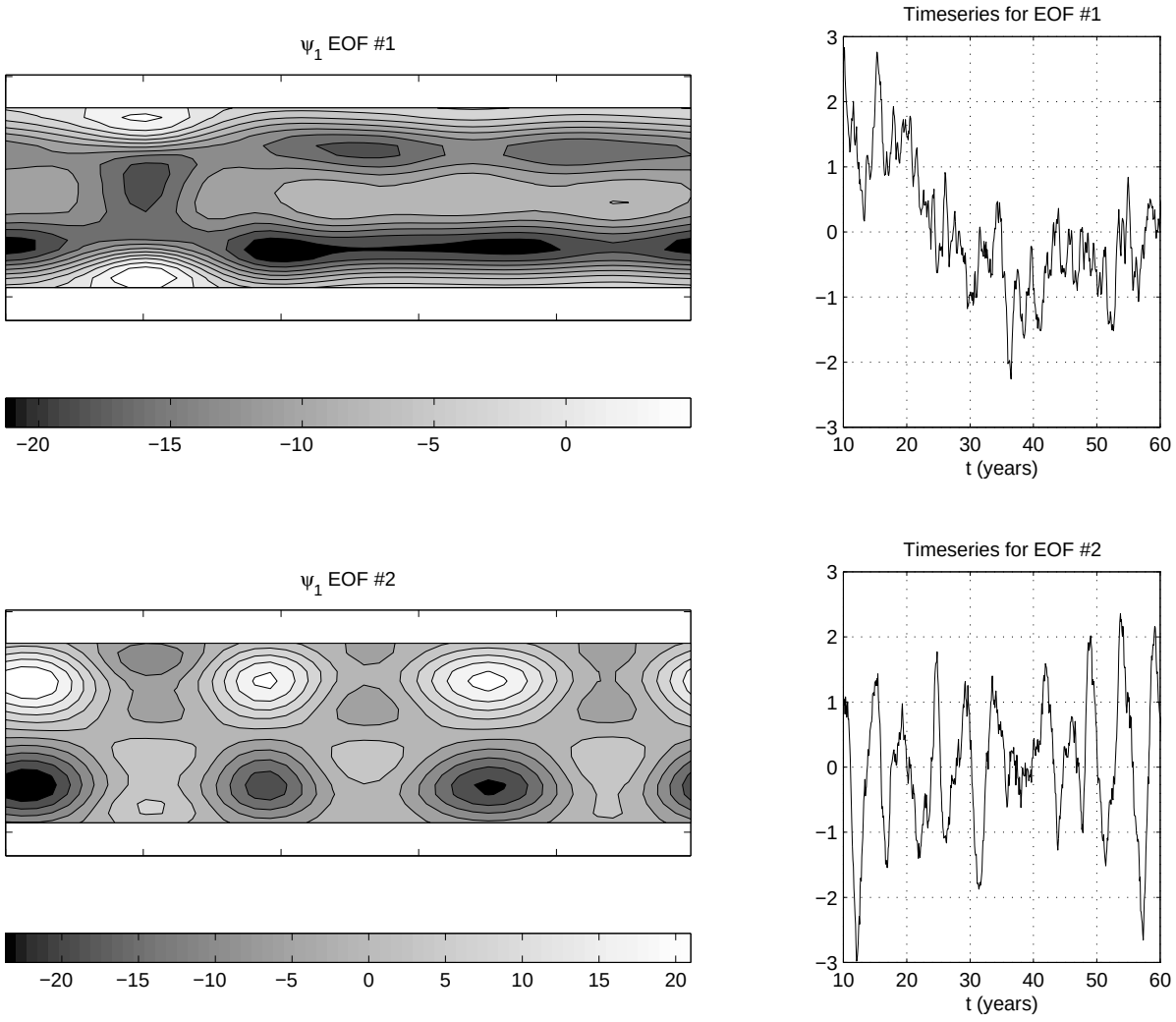

Figure 3-7: EOFs of the upper-layer atmospheric streamfunction for the stochastically-forced coupled model run depicted in Figure 3-6. Top: Pattern (left) and timeseries (right) of the first EOF, which explains 55% of the deterministic variability. Bottom: Pattern (left) and timeseries (right) of the second EOF, which explains 35% of the deterministic variability.

about 10% of the total atmospheric amplitude including both stochastic and deterministic contributions. As we predicted, the least-damped coupled mode previously discussed does, in fact, explain a large amount of the stochastic model's variability.

3.1.8 Summary

This series of experiments shows that eliminating some of the simplifications made in Chapter 2 does change the results in significant ways. A re-entrant geometry imposes an integer-wavenumber constraint on the coupling, which cannot always be satisfied by the coupled mode. Introducing coastlines in the model generates a strong damping tendency, as oceanic Rossby waves destroy themselves against the western boundary. Introducing a spatially-varying background atmospheric flow modifies the atmospheric wave pattern and locks the wave maxima to particular longitudes, where oscillate in a standing pattern. Adding stochastic forcing preferentially excites the coupled mode, and produces coupled interannual variability of reasonable amplitude.

These changes do not invalidate the essential physical process described in Chapter 2. In fact, in general, they improve the model's resemblance to observations of the NAO and (to a lesser extent) the Antarctic Circumpolar Wave. This improves our confidence in the model as a plausible mechanism for exciting interannual variability.

The one remarkably persistent result of these experiments is that the atmospheric response is characterized by a wavenumber-3, equivalent-barotropic pattern. In the plane-parallel flow of the analytic model, this pattern is the equilibrated mode, in which the Rossby wave phase speed nearly balances the downstream advection speed; this allows PV to accumulate over the forcing region, until the atmosphere comes into equilibrium with its forcing.

For the varicose background flow experiment, the complicated background flow and basic-state PV field prohibits us from easily verifying that the above description remains true. Thus, we move now into a discussion of "neutral vectors", which provide a way for us to identify equilibrated flows, even in very complex simulations.

3.2 Neutral Vectors

In Chapter 2, we noted briefly a connection between the dynamics of the atmospheric component of the analytic model and the "neutral vectors" discussed by Marshall and Molteni (1993). We observed that the coupled mode's atmospheric behavior was characterized by an approximate balance between westward Rossby wave propagation and eastward PV advection by the mean flow; the approximate balance of these terms allows PV in the model to accumulate and come into equilibrium with the thermal forcing.

Marshall and Molteni (MM, hereafter) were interested in atmospheric wave patterns which tended to persist in a given state for long periods of time. They attempted to compute patterns of maximum persistence by beginning with a forced three-layer QGPV model, which we schematize as:

$$\frac{\partial}{\partial t}\mathbf{q} = \mathcal{M}(\mathbf{\Psi}) + \mathbf{f}$$

where $\mathbf{\Psi}$ is a vector representing the model streamfunction, $\mathbf{q}$ is the model potential vorticity, $\mathcal{M}$ is a nonlinear tendency operator, and $\mathbf{f}$ is a PV source term. Linearizing this model about some basic state gives

$$\frac{\partial}{\partial t}\mathbf{q} = \mathsf{M}\mathbf{\Psi} + \mathbf{f} \tag{3.9}$$

The use of the same matrix label M in both (3.9) and (3.8) is deliberate: they are essentially the same thing. MM were interested in the free, unforced perturbations which displayed the smallest time tendency. Free, unforced waves obey

$$\frac{\partial}{\partial t}\mathbf{q} = \mathsf{M}\mathbf{\Psi} \tag{3.10}$$

To find the modes with the smallest time tendency, MM attempted to minimize the expression[3]

[3]Actually, MM wrote their equations as streamfunction tendencies, and minimized

$$\lambda^2 = \frac{\left\langle \frac{\partial}{\partial t}\mathbf{q}, \frac{\partial}{\partial t}\mathbf{q} \right\rangle}{\langle \mathbf{\Psi}, \mathbf{\Psi} \rangle} \tag{3.11}$$

where $\langle \mathbf{a}, \mathbf{b} \rangle$ is the inner product of $\mathbf{a}$ and $\mathbf{b}$. This expression minimizes the size of the mode's tendency, normalized by the magnitude of the mode itself. Inserting (3.10) into (3.11), we seek to minimize

$$\lambda^2 = \frac{\langle \mathsf{M}\mathbf{\Psi}, \mathsf{M}\mathbf{\Psi} \rangle}{\langle \mathbf{\Psi}, \mathbf{\Psi} \rangle} = \frac{\left\langle \mathsf{M}^\dagger \mathsf{M}\mathbf{\Psi}, \mathbf{\Psi} \right\rangle}{\langle \mathbf{\Psi}, \mathbf{\Psi} \rangle}$$

where $\mathsf{M}^\dagger$ is the adjoint of M. The $\mathbf{\Psi}$ which minimize λ will be the eigenvectors $\mathbf{\Psi}_n$ of $\mathsf{M}^\dagger\mathsf{M}$ with minimum eigenvalue λ_n^2.

$$\lambda^2 = \frac{\left\langle \mathsf{M}^\dagger \mathsf{M}\mathbf{\Psi}_n, \mathbf{\Psi}_n \right\rangle}{\langle \mathbf{\Psi}_n, \mathbf{\Psi}_n \rangle} = \frac{\langle \lambda_n^2 \mathbf{\Psi}_n, \mathbf{\Psi}_n \rangle}{\langle \mathbf{\Psi}_n, \mathbf{\Psi}_n \rangle}$$

Marshall and Molteni call these smallest eigenvectors of $\mathsf{M}^\dagger\mathsf{M}$ the "neutral vectors" of the atmospheric model. They can also be defined as the right singular vectors of M with the smallest singular values. One of the most remarkable results of their study, which received only passing mention in the paper, is that at least one of the neutral vectors closely resembles one of the empirical orthogonal functions (EOFs) of the observed wintertime streamfunction fields (namely, the NAO) – the neutral vectors are among the most prominent modes of variability of the true atmosphere. We will demonstrate and elaborate upon this point in Chapter 4. That neutral vectors resemble EOFs is perhaps not surprising: the neutral vectors are, by design, the most stable and persistent wave patterns, so it makes sense that these patterns should be prevalent in observations.

Neutral vectors are important because they identify the most prominent patterns of variability in the system from a *dynamical* framework. EOFs identify the most prevalent patterns in the data, but do not explain why those patterns appear.

$\left\langle \frac{\partial}{\partial t}\mathbf{\Psi}, \frac{\partial}{\partial t}\mathbf{\Psi} \right\rangle / \langle \mathbf{\Psi}, \mathbf{\Psi} \rangle$. This has the advantage of allowing λ to be interpreted as an inverse timescale, but since modes with small streamfunction tendency must also have small PV tendency, the difference should be otherwise unimportant. The technique used here is computationally simpler and faster, and will make further developments more lucid.

What are the dynamics of a neutral vector? The matrix $\mathbf{M}$ encapsulates the Rossby wave propagation, downstream advection, and dissipation terms of the QGPV equation. For $\mathbf{M}\Psi$ to be small, dissipation must be weak (implying large-scale patterns), and there must be a near-balance between the propagative and advective terms.

The similarity between the dynamical balance that defines a neutral vector and the balance required to produce a growing mode in our coupled model leads us to ask: Is the atmospheric component of the coupled mode always a neutral vector, even in complicated geometry? If so, what is it about neutral vectors which makes them prone to coupling?

3.2.1 Coupled modes and neutral vectors

Using the same Arnoldi technique we employed to find the eigenvalues of the coupled system with largest positive real part, we can efficiently find the eigenvectors of $\mathbf{M}^\dagger\mathbf{M}$ (all of which are positive or zero, since the matrix is self-adjoint) which have smallest magnitude. We have computed the most neutral vectors of the constant zonal-flow atmosphere (not shown). The first five vary only meridionally, and have no zonal structure. As such, they are completely unaffected by zonal advection or Rossby wave propagation. Only frictional dissipation influences them: they are "neutral" in a rather trivial way.

The most neutral vectors with zonal structure are #6 and #7; they display wavenumber 3 structure zonally, and wavenumber 1 zonally, and are 90° out of phase with each other. This is exactly the structure of the coupled mode found in 3.1.4.

In Figure 3-8, we show the three most neutral modes for the atmosphere with a varicose background flow discussed in Section 3.1.6. The most neutral vector is a zonal mode analogous to the modes with no zonal structure found above; it also closely resembles the first EOF of the stochastically-excited coupled model of Section 3.1.7. The second and third neutral vectors display structures nearly identical to the structure of the coupled mode in Section 3.1.6. (The shape of the atmospheric pattern in Section 3.1.6 varies periodically in the time-evolving model run; it tends to

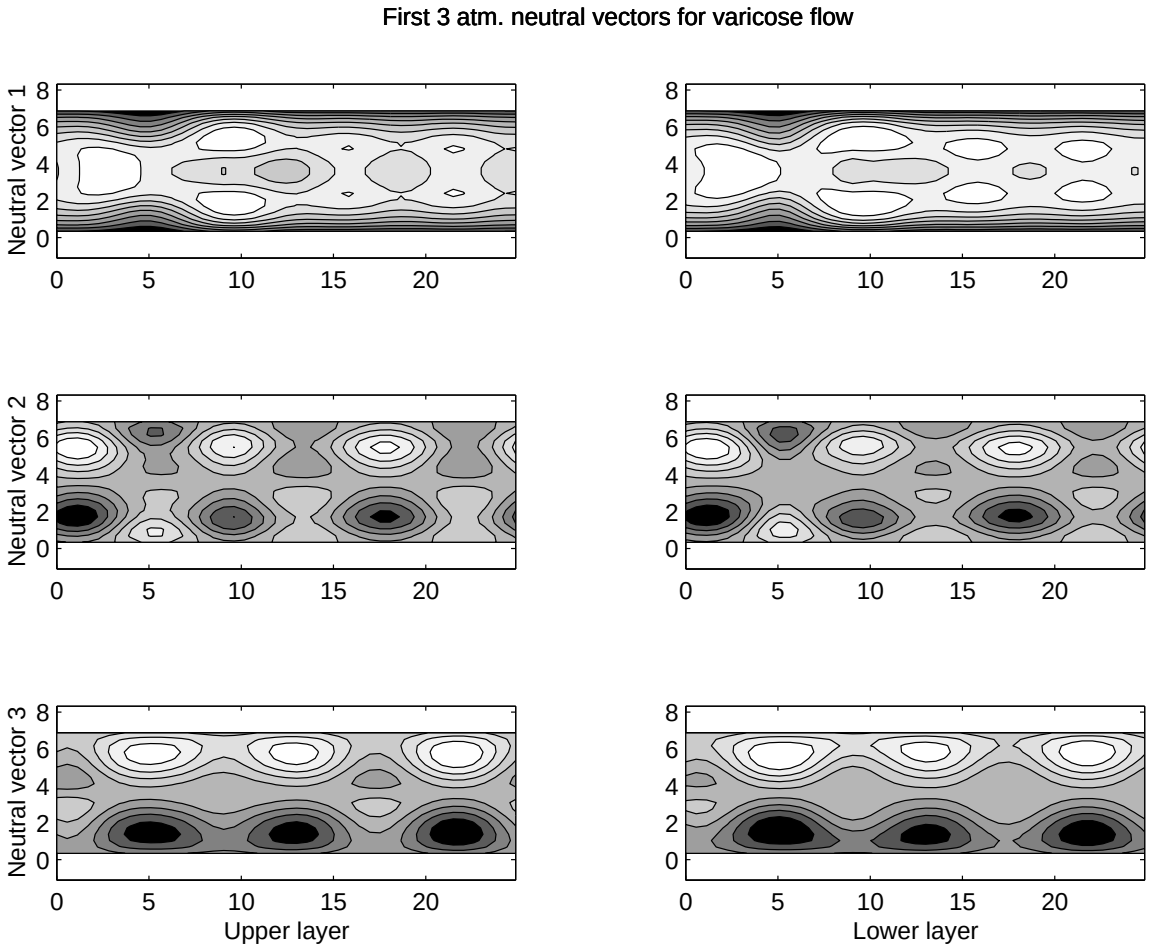

Figure 3-8: Maps of the first three neutral vectors of the atmospheric with a varicose background flow as pictured in Figure 3-4. From top to bottom, neutral vectors 1-3. Left column: upper-level streamfunction. Right column: lower-level streamfunction.

oscillate between a state resembling neutral vector 2 and a state resembling neutral vector 3.

This provides a demonstration that the neutral vectors continue to determine the behavior of the atmospheric component of the coupled system, even when the atmosphere has a complicated background flow.

3.2.2 Relevance of neutral vectors to coupled interaction

Why is it the neutral vectors which are so important to the coupled model? The magnitude of coupling in the model is determined, at least partly, by the size of the atmospheric response to SST anomalies. An SST pattern which does not significantly

excite the atmosphere cannot invoke coupling.

Suppose we took the model in (3.9) and looked at the forced, stationary response to a thermal forcing $\mathbf{f}$.

$$0 = \mathbf{M}\boldsymbol{\Psi} + \mathbf{f}$$

What pair of forcing and response will have the largest response per unit forcing? We want to find the $\boldsymbol{\Psi}$ and $\mathbf{f}$ will maximize

$$\lambda^{-2} = \langle \boldsymbol{\Psi}, \boldsymbol{\Psi} \rangle \,/\, \langle \mathbf{f}, \mathbf{f} \rangle$$

Since $\mathbf{f} = -\mathbf{M}\boldsymbol{\Psi}$, this is equivalent to *minimizing*

$$\lambda^2 = \frac{\langle \mathbf{M}\boldsymbol{\Psi}, \mathbf{M}\boldsymbol{\Psi} \rangle}{\langle \boldsymbol{\Psi}, \boldsymbol{\Psi} \rangle}$$

This is exactly the condition required for the neutral vectors. Thus, the neutral vectors are not only the most stationary modes in the unforced time-evolving model, they are also the forced, stationary modes which exhibit the largest response to external forcing. This is exactly the same sort of resonance behavior which makes a playground swing build up to large amplitude when the forcing matches the natural resonance of the swing, though in our case the resonance is spatial rather than temporal.

Interestingly, this means we can not only find the neutral vectors, $\boldsymbol{\Psi}_n$, but also the "optimal forcing patterns" $\mathbf{f}_n$ which maximally excite them, by solving $\mathbf{M}\boldsymbol{\Psi}_n + \mathbf{f}_n = 0$. The $\boldsymbol{\Psi}$ are the right singular vectors of $\mathbf{M}$; the $\mathbf{f}_n$ are the left singular vectors.

In our coupled model, which has a very simple atmospheric heating scheme, the connection between SST and baroclinic PV forcing is a simple linear relation. Thus, when the coupled model's SST has a strong projection onto the baroclinic part of an optimal forcing pattern $\mathbf{f}_n$, we see a corresponding strong atmospheric response of the corresponding neutral vector.

This is illustrated in Figure 3-9. At the top of the figure, we show the upper-level streamfunction of neutral vectors 2 and 3 for the wavy-background flow model; these

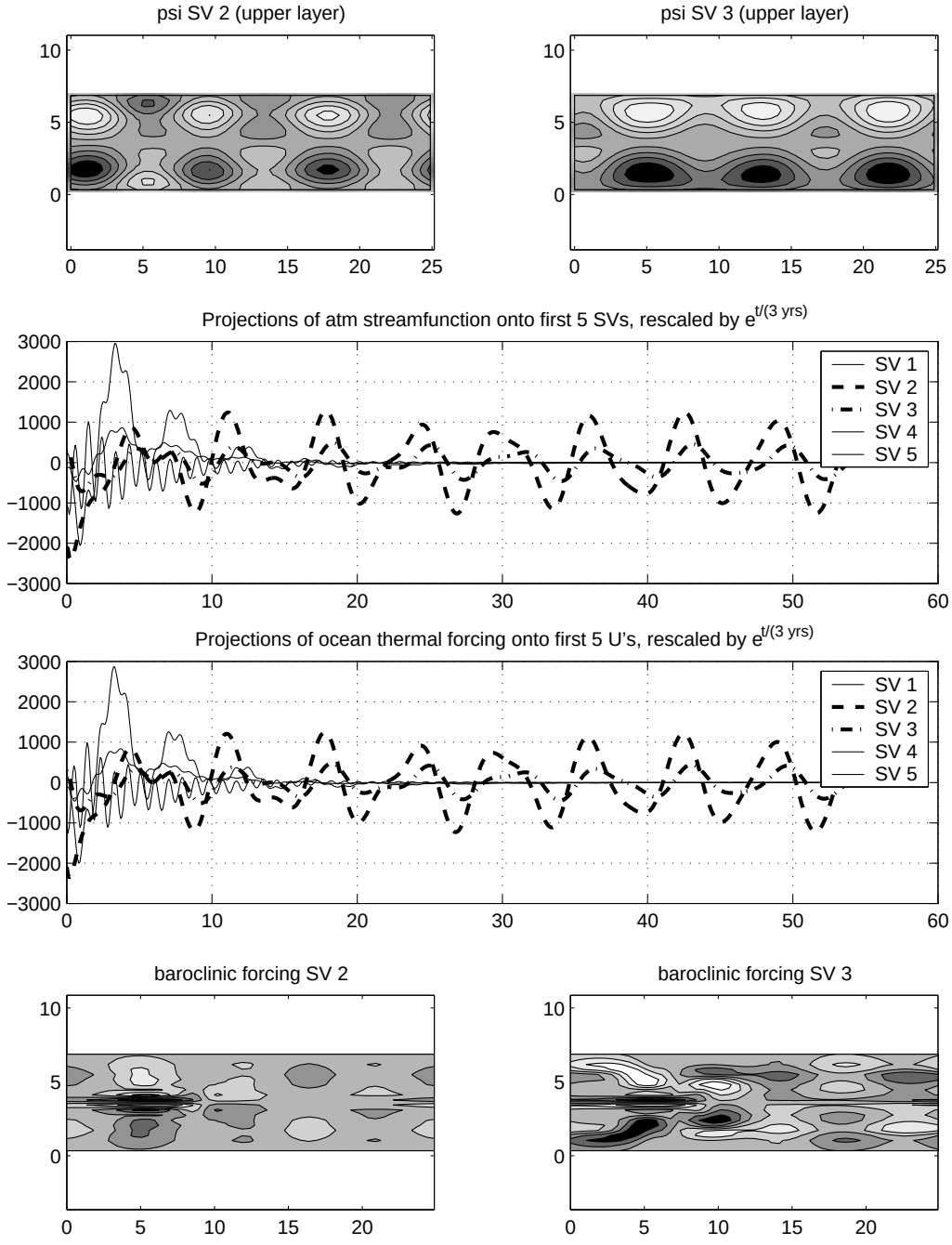

Figure 3-9: Projections of neutral vectors and optimal forcing patterns onto a forward model run. Top left, right: upper-layer streamfunction pattern for neutral vectors 2 and 3, respectively, of the atmospheric model with a varicose jet background flow. Below that, we show the projection of the time evolution of the coupled model's atmosphere onto singular vectors 1 through 5. Bottom left, right: The baroclinic part of the PV forcing which excites neutral vectors 2 and 3 ("optimal forcing patterns"; see text.). Above that, we show the projection of SST-induced atmospheric thermal forcing onto the first five optimal forcing patterns.

were the neutral vectors which resembled the coupled model's behavior. The upper timeseries shows the projection of the model's atmospheric state onto the first five neutral vectors. Since the model ocean has a western boundary, the model response is damped. We have thus multiplied the projection values by $e^{t/3\text{yrs}}$, to counteract the exponential decay and zoom in on the longer-term variations. We see clearly the oscillation of the model state between neutral vectors 2 and 3, as described in the previous section. The lower pair of contour plots show the baroclinic part of the optimal forcing pattern associated with these neutral vectors. The lower timeseries shows the projection of the thermal forcing anomalies generated by SST onto the first five optimal forcing patterns, rescaled as with the neutral-vector timeseries. The match is identical, as a consequence of the linearity of the atmospheric response operator.

From Figure 3-9, we can describe the behavior of the coupled mode. As the model's SST pattern evolves according to ocean dynamics, it projects alternately onto two different optimal forcing patterns. This projection excites a large atmospheric neutral vector response, which then provides a windstress to further modify the SST.

One point of concern regarding this description concerns the robustness of the optimal forcing patterns. In Figure 3-9, the optimal forcing patterns show complicated fine structure in some areas (particularly near x=5000 km, y=3200 km, in the "pinched" part of the background flow; there, we find an alternating positive/negative banded pattern at the gridscale level.) This may be due to the minimal eddy viscosity used in this model. If most of the SST forcing pattern's projection onto this pattern occurs in this fine-structure region, we should be concerned that the stability of the coupled mode is sensitive to small changes in the model domain. However, we find (figure not shown) that the bulk of the projection of SST onto the forcing pattern occurs in the broad "wings" to the north and south in forcing pattern 2, and to the northeast and southeast in pattern 3.

3.3 Conclusions

We have built a numerical model which obeys the coupled physics desribed in our earlier paper, but which allows for more complex geometry and non-uniform basic-state flows. The existence of a western boundary causes damping of the coupled mode due to oceanic Rossby-wave dissipation; however, this does not destroy the viability of our coupling mechanism. The use of a non-uniform background flow in the atmosphere does not present further problems: instead, by locking the atmospheric streamfunction anomalies to particular longitudes, it increases the resemblance to observed interannually-varying patterns, which do not propagate.

Our most generally-useful finding is that the coupled model's atmospheric response takes the form of "neutral vectors", patterns which exhibit a near-balance between mean-flow advection and Rossby wave propagation. The explanation for this is that neutral vectors are the modes most readily excited by thermal forcing provided by ocean SST anomalies. This strong response is thus able to imprint itself back upon the ocean.

Our model is extraordinarily crude, and so we should not expect the particular shapes and patterns of the coupled mode and the atmospheric neutral vectors to correspond in detail with observed patterns, although their rough agreement is promising. However, the physical mechanism of coupling (excitation of neutral vectors by SST forcing) can be applied in much more realistic situations, and our results suggest that neutral vectors are likely to be important for atmosphere-ocean interaction in a very general sense.

In particular, Marshal & Molteni's identification of an NAO-like pattern as the first singular vector of their 3-layer QG model (which has a very realistic climatology), combined with the implication of the NAO in long-term atmosphere-ocean coupling by a great many authors, hints strongly that neutral vectors can be useful in identifying and interpreting coupled atmosphere-ocean interactions.

In the next chapter, we return to Marshall & Molteni's 3-layer QG model, to look more closely at the connection between neutral vectors and EOFs, and to try to find

the optimal forcing pattern associated with their first neutral vector (the one which resembles the NAO). The ability to identify a forcing pattern which produces the NAO pattern would be a major step forward: we could use it to see whether the patterns of SST associated with a strong NAO pattern are those which are capable of exciting the NAO. If this is true, this strongly suggests (but does not prove) that SST plays an active role in driving the NAO pattern, and implies that interannual NAO variability may be a mutually coupled phenomenon.

The identification of neutral vectors is not limited to simple QG models with trivial model physics. The tendency matrix $\mathbf{M}$ can be arbitrarily complex: it could even represent an entire atmospheric general circulation model, linearized about some suitable basic state. The $\mathbf{M}^{\dagger}$ matrix is then the adjoint of this model. The Lanczos technique can find eigenvectors of an arbitrarily general linear algorithm; we can thus find the neutral vectors of an entire linearized GCM, along with the corresponding optimal forcing patterns. This is, as one might imagine, a computationally intensive task. However, the implementation could be made easier through the use of an automatic tangent linear / adjoint compiler (Marotzke *et al.* 1999) which can automatically generate adjoint model code from the forward source.

The neutral vector concept can be generalized to almost any model physics, and will be relevant to the investigation of atmosphere-ocean coupled modes whenever the atmosphere responds to SST forcing anomalies in an essentially linear way, and when a large atmospheric response will produce a large forcing of the ocean by the atmosphere.

The optimal forcing pattern / neutral vector pair can be viewed as a mechanism which accepts a small SST thermal forcing from the ocean and returns a large atmospheric response, which may translate into a large feedback onto the ocean. However, this is only half the story: the ocean must be able to accept the forcing provided by the atmosphere and return (some nontrivial projection onto) the neutral vector's optimal forcing pattern in order for a mutually coupled interaction to occur (see Figure 3-10). Optimal forcing pattern / neutral vector pairs can play a key role as pattern-selective amplifiers in a coupled atmosphere-ocean system.

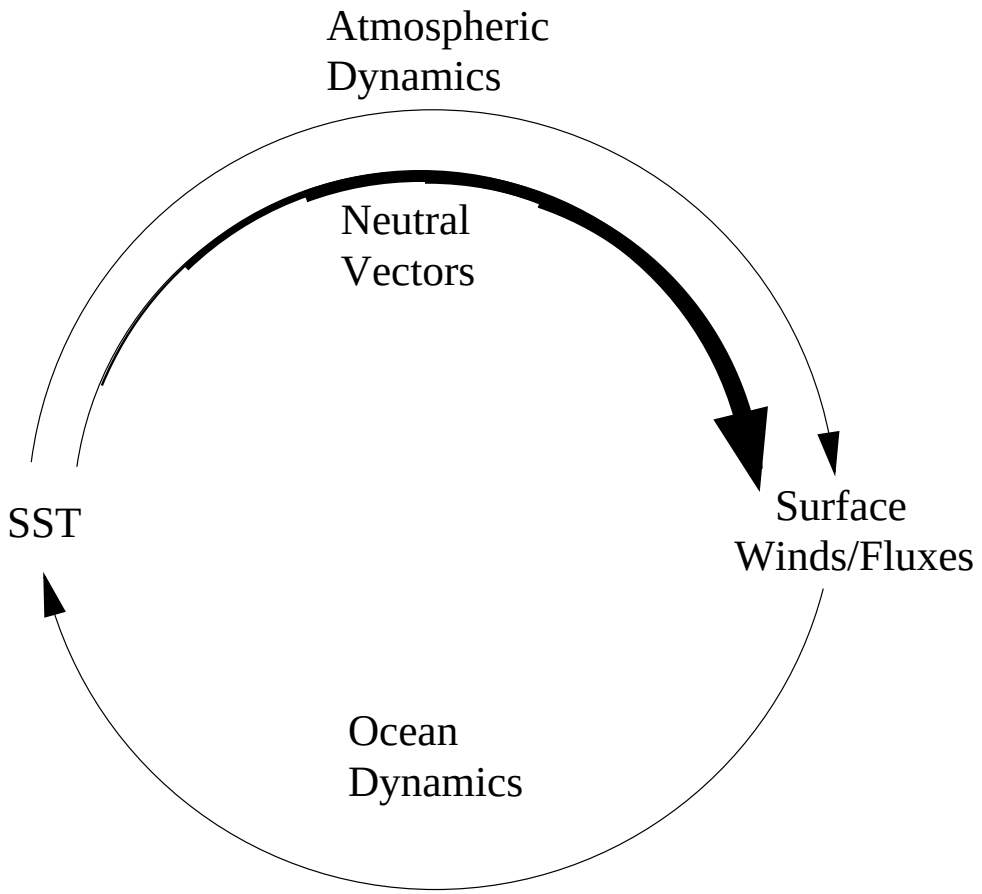

Figure 3-10: Schematic representation of the mutually-coupled atmosphere-ocean hypothesis of interannual climate variability. The role of neutral vectors is to translate specific patterns of small SST variations into large atmospheric response patterns. This provides pattern-selective amplification of ocean anomalies.

Chapter 4

Neutral vectors and optimal forcing patterns in a 3-layer quasigeostrophic model

In Chapter 2, we identified a potential mechanism of coupled atmosphere-ocean interaction which leads to interannual variability. In Chapter 3, found that the shape of this coupled mode is determined by nearly-resonant "neutral vector" patterns in the atmosphere. Neutral vector patterns provide the maximal atmospheric response to external forcing, thus providing an amplification mechanism. In this chapter, we take what we have learned about the role of neutral vectors in coupled air-sea interaction and attempt to apply it to a more realistic model of atmospheric dynamics – namely, the 3-layer quasigeostrophic model used by Marshall and Molteni (1993) (hereafter referred to as MM).

The model and neutral vector computation techniques are described in Section 4.1. We discuss the the model's empirical orthogonal functions in Section 4.2. The neutral vectors are discussed in Section 4.3, with some mathematical insight into the connection between neutral vectors and EOFs is given in Section 4.3.2. We consider the model's optimal forcing patterns in Section 4.4, including an attempt to discover whether the optimal forcing patterns remain optimal in the full nonlinear model in Section 4.4.3.

4.1 Molteni's 3-layer quasi-geostrophic model

Molteni's model is discussed in some detail in his thesis (1994), and in Marshall & Molteni (1993). The model is a 3-layer, global, spectral model at T21 resolution, with pressure as a vertical coordinate. The quasi-geostrophic potential vorticity equations are discretized at the three pressure levels (200, 500, 800 mb), giving prognostic equations for PV:

$$\begin{aligned}
\frac{\partial}{\partial t} q_1 &= -J(\psi_1, q_1) \quad -D_1(\psi_1, \psi_2) \quad +S_1 \\
\frac{\partial}{\partial t} q_2 &= -J(\psi_2, q_2) \quad -D_2(\psi_1, \psi_2, \psi_3) \quad +S_2 \\
\frac{\partial}{\partial t} q_3 &= -J(\psi_3, q_3) \quad -D_3(\psi_1, \psi_2) \quad +S_3
\end{aligned}$$

The ψ_n and q_n are the streamfunction and QGPV at each level, D_n encapsulate various dissipative processes (see Molteni, 1994), and the S_n are a constant PV source term. PV is defined as:

$$\begin{aligned}
q_1 &= \nabla^2 \psi_1 && -R_1^{-2}(\psi_1 - \psi_2) && +f \\
q_2 &= \nabla^2 \psi_2 && +R_1^{-2}(\psi_1 - \psi_2) - R_2^{-2}(\psi_2 - \psi_3) && +f \\
q_3 &= \nabla^2 \psi_3 && +R_2^{-2}(\psi_2 - \psi_3) && +f(1 + h/H_0)
\end{aligned}$$

where R_1 and R_2 are (spatially constant) Rossby radii of deformation, h is the height of topography, and H_0 is a topographic scaling factor.

The model covers the entire globe, so it does not have artificial "walls" at the equator or elsewhere which may spuriously reflect planetary waves. However, since QG dynamics is not really appropriate near the equator (and the constant values for the Rossby radii are certainly wrong there), the model's behavior in the tropics should not be taken too seriously.

In the mid-latitudes, however, the model's dynamics are reasonable, and it can be made to produce a very good mean flow field through careful specification of the

constant forcing fields S_n. This is done by setting the S_n equal to the opposite of the average PV tendencies obtained by inserting observed streamfunction fields into a version of the model equations from which the S_n are omitted. This forces the model to have a stable climatology which is near the observed fields used to generate the S_n. The technique is similar to the "flux correction" used to eliminate climate drift in coupled GCMs. See Molteni (1994) for more details. The S_n used for this study are computed from ECMWF streamfunction analyses, using data from December through March for 1983 through 1993 (Michelangeli and Vautard, 1998). As a result, the model attempts to simulate the northern wintertime climatology.

Figure 4-1 compares various model mean fields with observations; these fields are computed from a 5000-day integration of the model. Comparisons with observed wintertime mean streamfunction (not shown) show that the model does a very good job at reproducing the mean flow of the observations used to compute S. The mid-latitude jets have the correct magnitude and the correct confluence/diffluence as they pass over continents and oceans; generally, the model's mean state lies within a few percent of observations. Model eddy activity, as shown by streamfunction standard deviation in the lower panel, is less accurate, but the model does have the right amplitude of eddy activity; we do see storm tracks over the northern hemisphere oceans, at approximately the right longitudes. The Pacific storm track looks quite similar to observations; however, the Atlantic storm track does not have a sharp northern boundary, and eddy activity is generally somewhat stronger than observed over the pole.

We use this 5000-day run to compute empirical orthogonal functions of the model output. The EOFs shown in Section 4.2 are computed over the entire model domain, using monthly-mean data. EOFs computed over weekly-averaged data are quite similar.

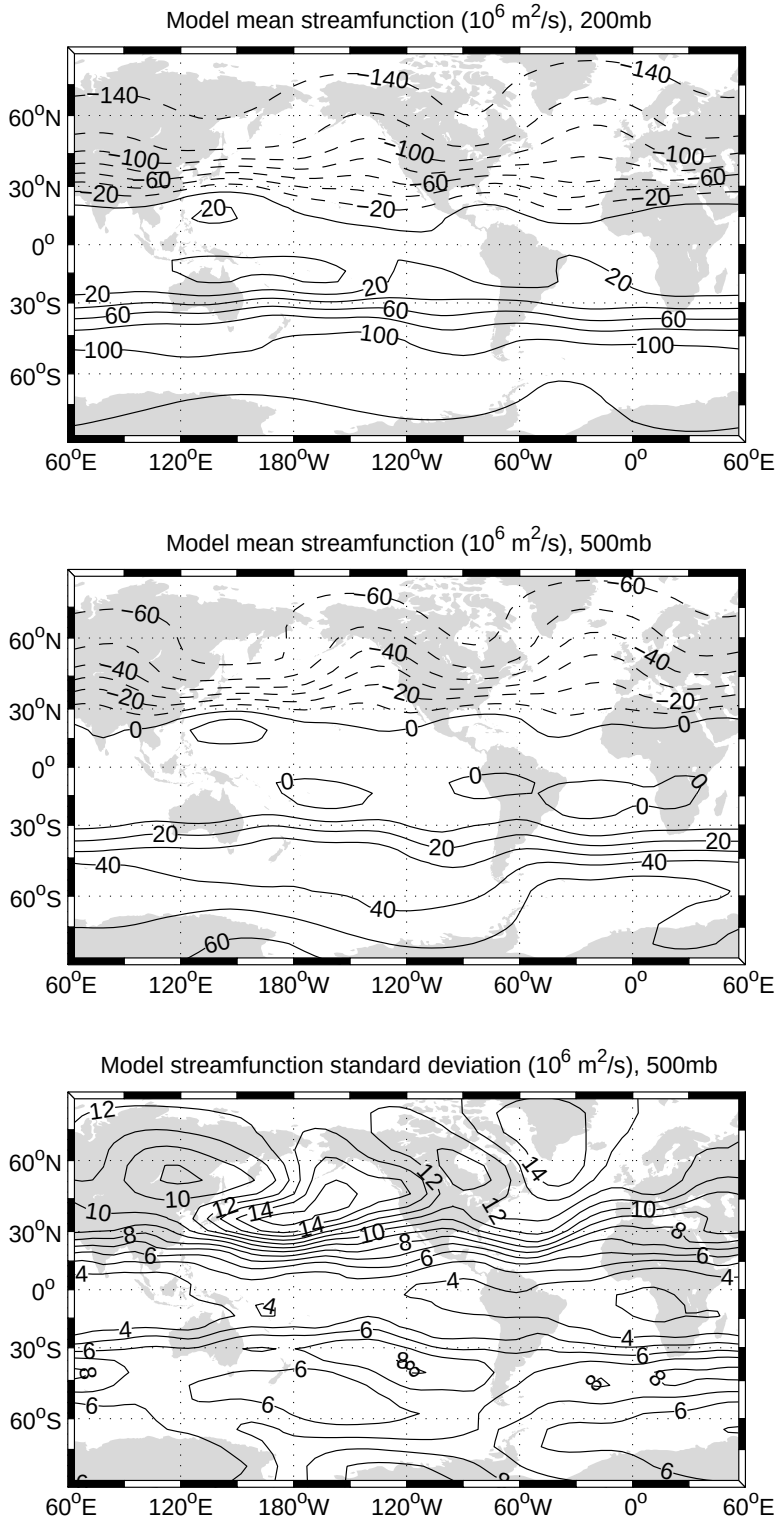

Figure 4-1: 3-layer QG model mean climatology, based on 5000 daily fields. Top panel: mean streamfunction, 200 mb, contour interval $20 \cdot 10^6$ m^2/s. Middle panel: mean streamfunction, 500 mb, contour interval $10 \cdot 10^6$ m^2/s. Lower panel: Model streamfunction standard deviation, 500 mb, contour interval 10^6 m^2/s.

4.1.1 Computing neutral vectors

We compute neutral vectors using the same general technique as introduced in Section 3.2. As before, the linearized system takes the form:

$$\frac{\partial}{\partial t}q = -J(\overline{\psi}, q) - J(\psi, \overline{q}) - D(\psi) + S \tag{4.1}$$

where overlined terms represent the basic state, and unmarked terms represent perturbation quantities. We discretize and write this in vectorized form as

$$\frac{\partial}{\partial t}\mathbf{q} = \mathbf{M}^*\mathbf{\Psi} + \mathbf{S} \tag{4.2}$$

For consistency with MM's analysis, we depart from the technique introduced in Section 3.2, by performing a PV inversion of both sides of this equation.

$$\frac{\partial}{\partial t}\mathbf{\Psi} = \mathbf{M}\mathbf{\Psi} + \mathbf{f} \tag{4.3}$$

Here, $\mathbf{M}$ is the streamfunction tendency operator, and $\mathbf{f}$ is the streamfunction forcing perturbation. We now minimize the tendency (for the unforced problem) or the forcing (for the steady problem)

$$\lambda^2 = \frac{\left\langle \frac{\partial}{\partial t}\mathbf{\Psi}, \frac{\partial}{\partial t}\mathbf{\Psi} \right\rangle}{\langle \mathbf{\Psi}, \mathbf{\Psi} \rangle} \qquad \text{unforced, time-evolving} \tag{4.4}$$

$$\lambda^2 = \frac{\langle \mathbf{f}, \mathbf{f} \rangle}{\langle \mathbf{\Psi}, \mathbf{\Psi} \rangle} \qquad \text{forced, steady} \tag{4.5}$$

by computing the left and right singular vectors of $\mathbf{M}$ as described in section 3.2. One advantage of the PV inversion is that it allows the eigenvalues λ to be interpreted as inverse timescales – a mode will remain relatively unchanged for a time λ^{-1}. One awkward aspect is that while the neutral vectors are still streamfunction anomalies, the optimal forcing patterns are now *streamfunction* forcing patterns rather than PV forcing patterns.

One can make various choices for the inner product in equation 3.11; This boils down to the question: "We want to find the patterns whose tendency is smallest...

but what do we mean by smallest?". To begin, we choose an inner product identical to that used by MM: the norm of a streamfunction vector is proportional to its kinetic energy. We refer to the is as the "KE norm"; a different choice will be considered in Section 4.4.1.

The only remaining difficulty is to construct the $\mathbf{M}$ matrix. This job is made much simpler by the existence of a linearized version of the Molteni model code, supplied to us by David Ferreira. We linearize about the mean state of the 5000-day run shown in Figure 4-1. Using this linearized code, we simply compute the tendencies of a complete set of orthonormal spectral Green's function perturbations, and use those tendencies to build up an explicit matrix $\mathbf{M}$ column-by-column. We then use Matlab's eigensolver to compute the smallest eigenvectors of $\mathbf{M}^\dagger\mathbf{M}$. We do not use the Arnoldi technique, because the tendency matrix is dense (but smaller) when expressed using a spectral basis. However, the eigenvalues can still be found fairly rapidly.

4.2 Empirical orthogonal functions

The first few EOFs of the model's monthly-mean streamfunction fields are shown in Figure 4-2. The EOFs are different from those described by Molteni *et al.* (1998); this is probably because Molteni *et al.* computed hemispheric EOFs of the *eddy* fields (i.e., zonal-mean components are removed), while we compute global EOFs of the full streamfunction. Also, Molteni's patterns are EOFs of observed fields, while we compute EOFs of the model output – and the model is, of course, not perfect.

Nonetheless, the model EOFs do resemble observations. The first EOF, explaining 35% of the variance of monthly means, has the dipolar nature of the NAO in the Atlantic, but is much more zonally extensive. It more closely resembles an "annular mode", or the "Arctic Oscillation" (AO) (Thomson & Wallace, 1998), which are commonly seen in full-hemisphere EOF analyses of observations and models.

Wallace (2000) makes a strong case that the NAO and the AO are really the same phenomenon: an "annular mode" which is somewhat stronger in the Atlantic than elsewhere. We have noted that papers which use EOFs localized to the Atlantic

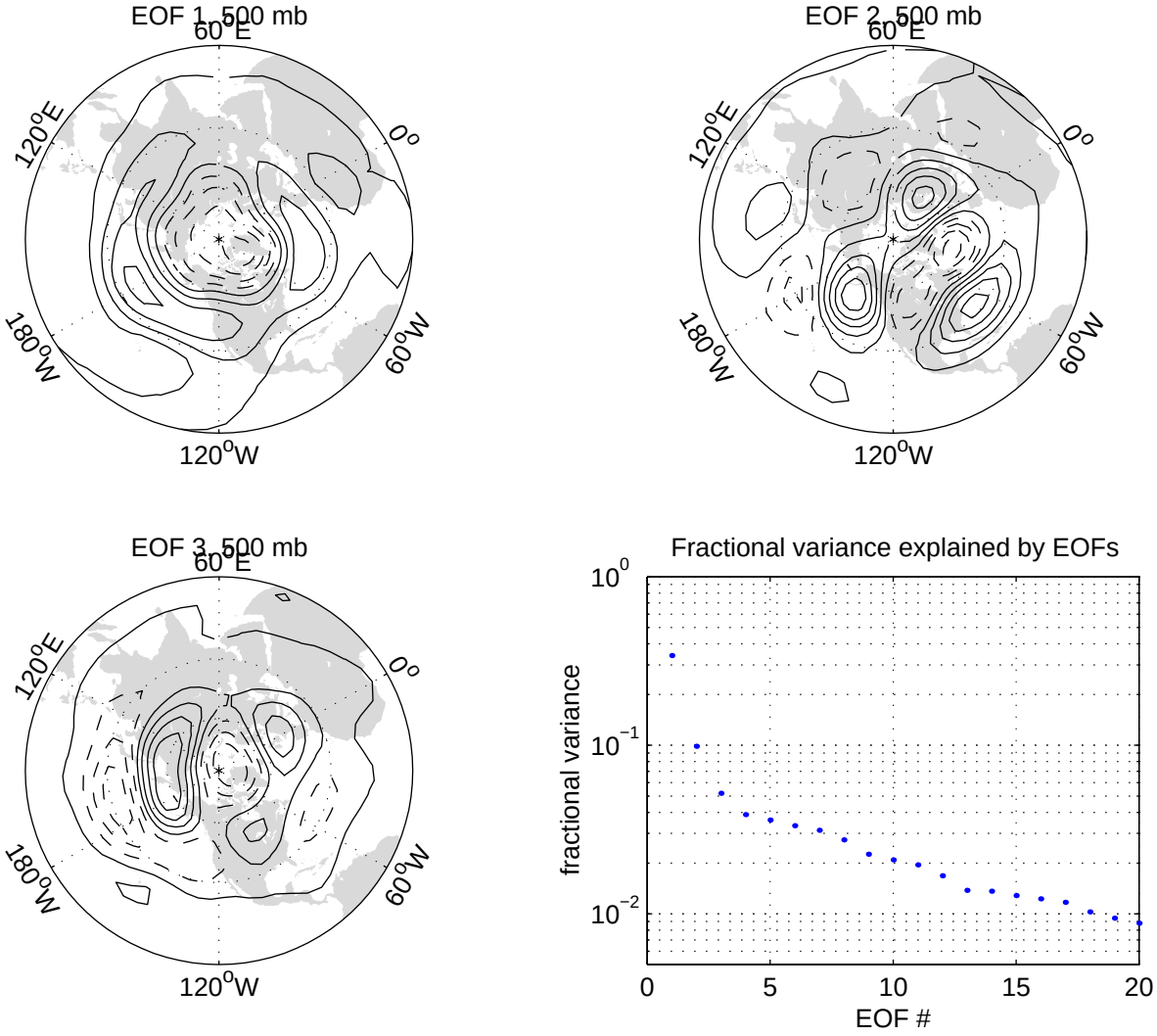

Figure 4-2: Empirical orthogonal functions computed from monthly means of a 5000-day integration of the Molteni QG model. EOFs are computed on global model output at all 3 levels; EOF amplitude at 500 mbar is shown here.

domain (Cayan, 1992 for example) tend to find a more localized NAO pattern, while hemispheric EOF calculations (Thompson & Wallace, 1998) tend to find the annular AO pattern. In Appendix B, we show why this might occur.

The second EOF of the model is essentially identical to the planetary wave pattern associated with the PNA (Pacific–North America) pattern (Wallace, 1995). We see a wave-train extending from the subtropical Pacific near the dateline over the Gulf of Alaska and Canada, and ending in the subtropical West Atlantic. Authors interested in ENSO teleconnections (for example, Keables, 1992) have suggested that the PNA is a response to tropical SST forcing anomalies; this cannot be complete answer, since our model produces a beautiful PNA pattern without any time-varying forcing.

The third EOF displays a wave train extending from the mid-latitude Pacific west of the dateline over the pole to Western Europe, and has wavelengths similar to the first two EOFs.

4.3 Neutral vectors

When we computed neutral vectors for the 3-layer model in the straightforward manner discussed in section 4.1.1, we discovered that while the EOFs were confined to the northern hemisphere, the neutral vectors were found in either or both hemispheres. The reason for this difference will be discussed in Section 4.3.2. We feel it is unlikely that a dynamical connection exists between wave patterns in alternate hemispheres; it is more likely that two separate neutral patterns in the two hemispheres share similar eigenvalues. The SVD analysis cannot distinguish two modes with similar eigenvalues, and will return two orthogonal linear superpositions of the two modes. A "rotated neutral vector analysis", along the lines of rotated EOFS (Richman, 1986), might help to separate the modes.

Instead of rotating the modes, we focus on the northern hemisphere by adding an artificial damping term to the $\mathbf{M}$ matrix. This term is proportional to $\sin(\phi/2-\pi/4)^6$ (where ϕ is latitude in radians), and damps PV anomalies with a timescale of 5 days at the south pole, 8 days at 45° S, 40 days at the equator, and 1500 days at 45° N.

Thus, any otherwise-neutral mode in the southern hemisphere will have a significant tendency due to this damping effect, making it less neutral. The general effect is to re-order the neutral mode patterns, giving preference to northern-hemisphere modes.

4.3.1 Neutral vector structure

In Figures 4-3 through 4-5, we show neutral vectors and optimal forcing patterns computed using the "kinetic energy" norm used by MM. We describe the neutral vectors (right-hand column) in detail in this section; the optimal forcing patterns are discussed in Section 4.4.1.

The first neutral vector (Figure 4-3, right column) shows a roughly zonally-symmetric pattern, with a negative center over the pole surrounded by a positive annulus in high middle latitudes. This annulus has enhanced energy over western Siberia and the North Atlantic. The whole pattern is equivalent barotropic, and broadly resembles the first model EOF, although its mid-latitude annulus is shifted farther to the north.

The second neutral vector resembles the first EOF quite closely; we see broad positive centers over the northern mid-latitude oceans, forming a nearly-complete annulus about the globe, with a polar negative center. Once again, the mode is barotropic, with amplitude increasing with height. The projection of this pattern onto the NAO pattern is quite strong.

The third neutral vector displays a pattern nearly identical to the PNA pattern. We see a barotropic wave train extending from the subtropical Pacific over the Gulf of Alaska, northern Canada, and into the subtropical east Atlantic. The subtropical Pacific maximum is shifted west across the dateline compared to the observed PNA, but elsewhere, the resemblance between neutral vector 3, EOF 2, and the PNA is very strong.

It should be quite obvious that these patterns strongly resembles the model EOFs and observed patterns of low-frequency variability. To emphasize this point, and to demonstrate that these resemblances are not the result of chance correlations in a low-dimensional system, we present Figure 4-6. This figure shows the cross-correlations

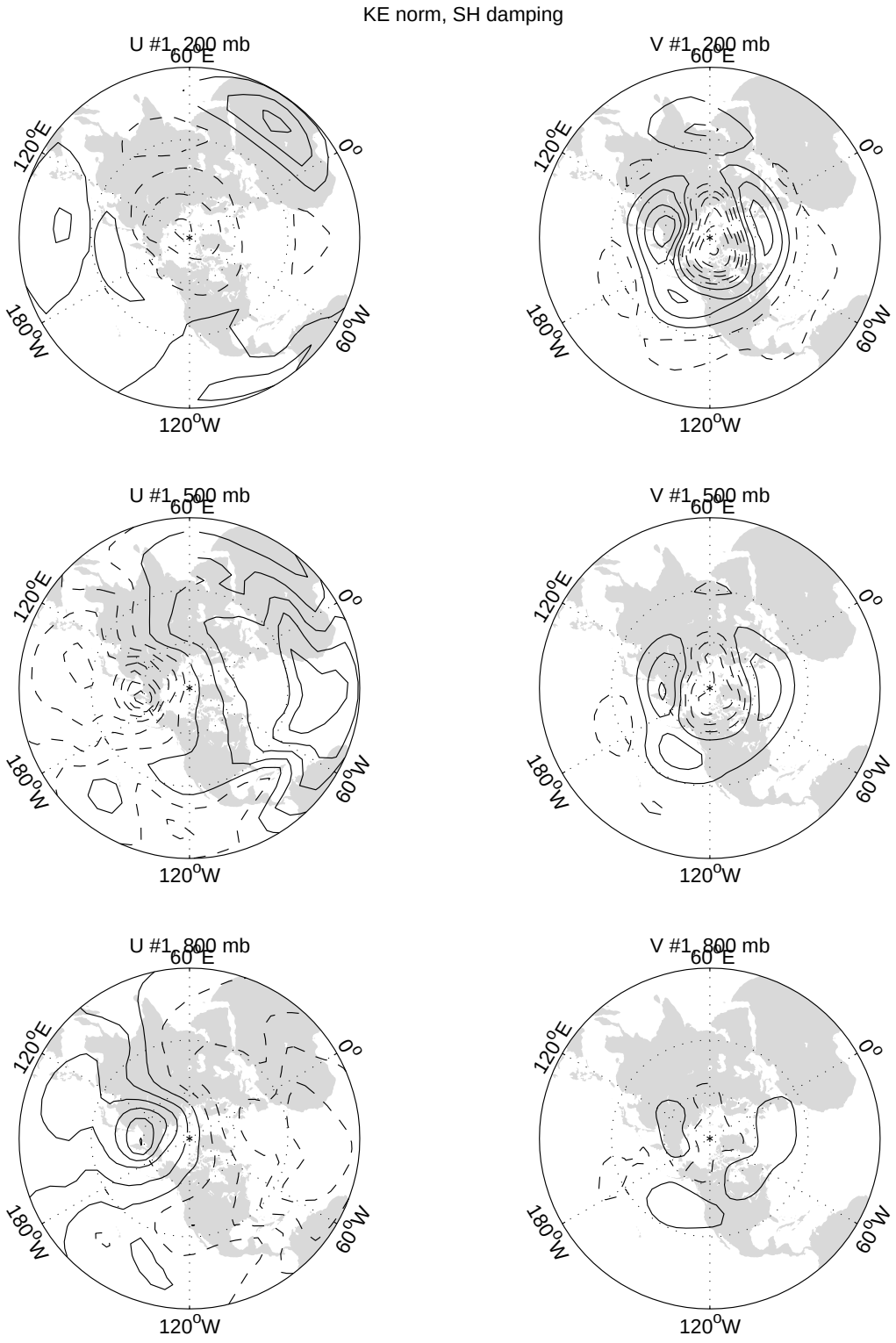

Figure 4-3: Right column: Neutral vector #1 for model climatology, KE inner product. Left column: corresponding optimal forcing pattern. Contour interval is arbitrary, but consistent from level to level.

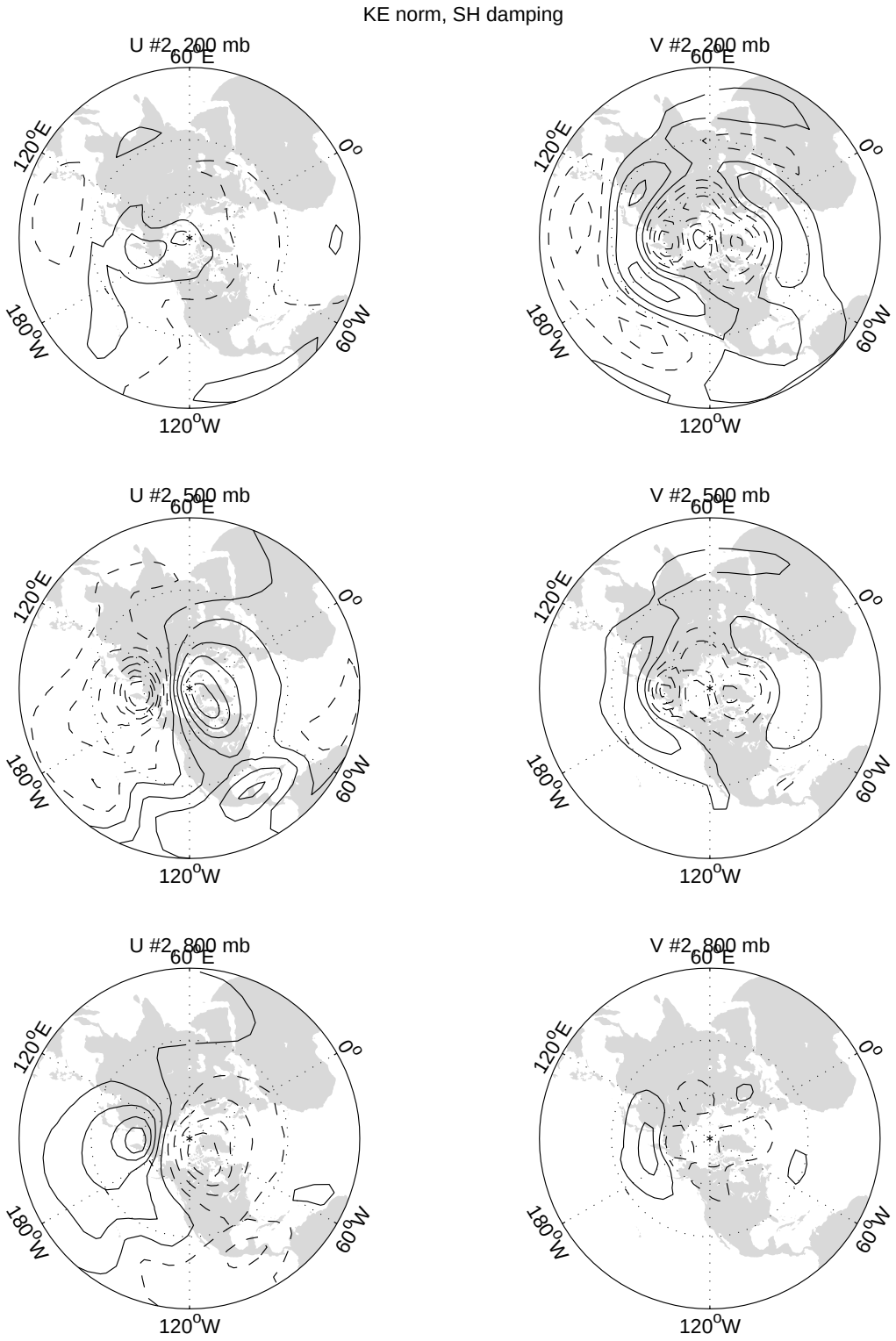

Figure 4-4: Right column: Neutral vector #2 for model climatology, KE inner product. Left column: corresponding optimal forcing pattern.

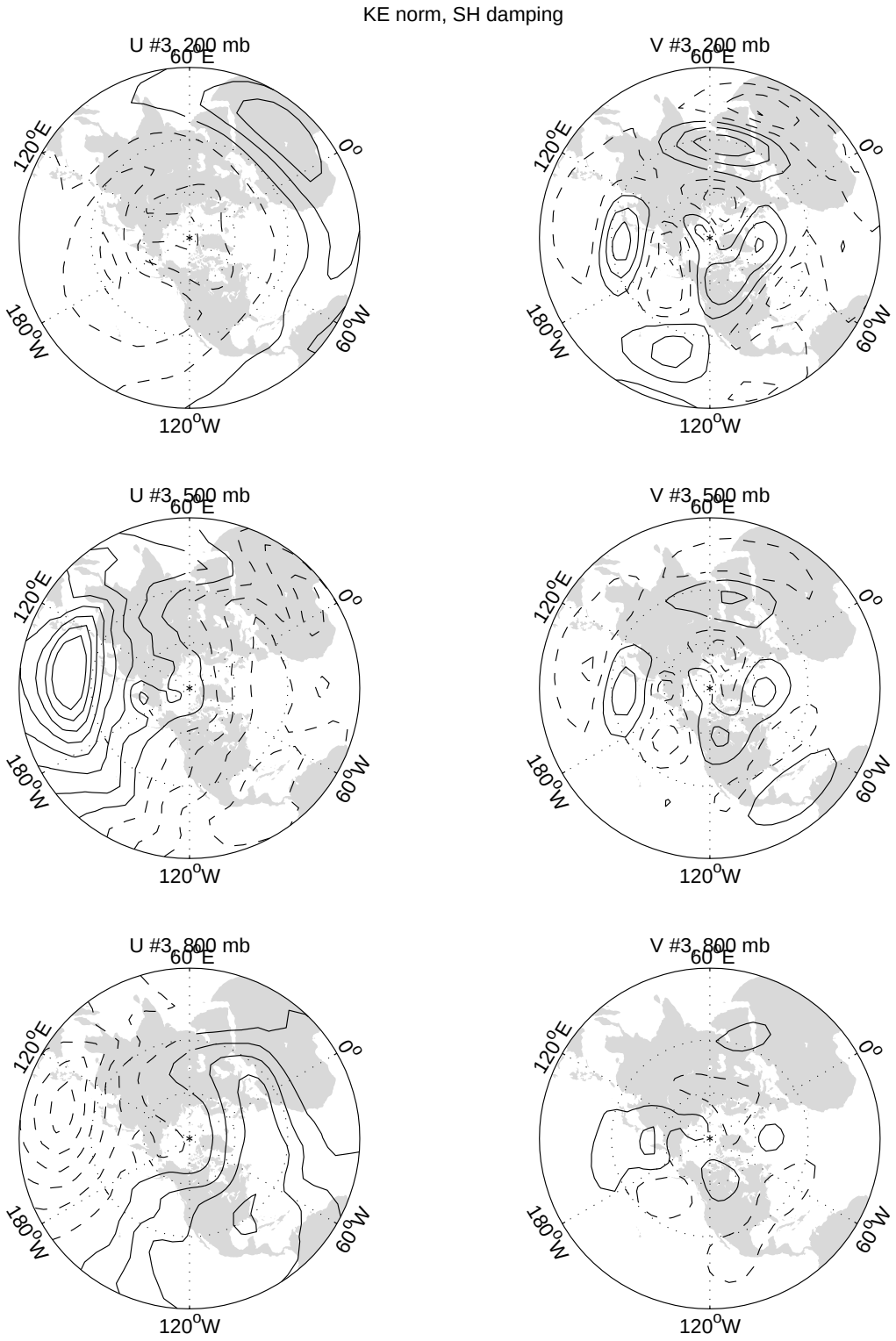

Figure 4-5: Right column: Neutral vector #3 for model climatology, KE inner product. Left column: corresponding optimal forcing pattern.

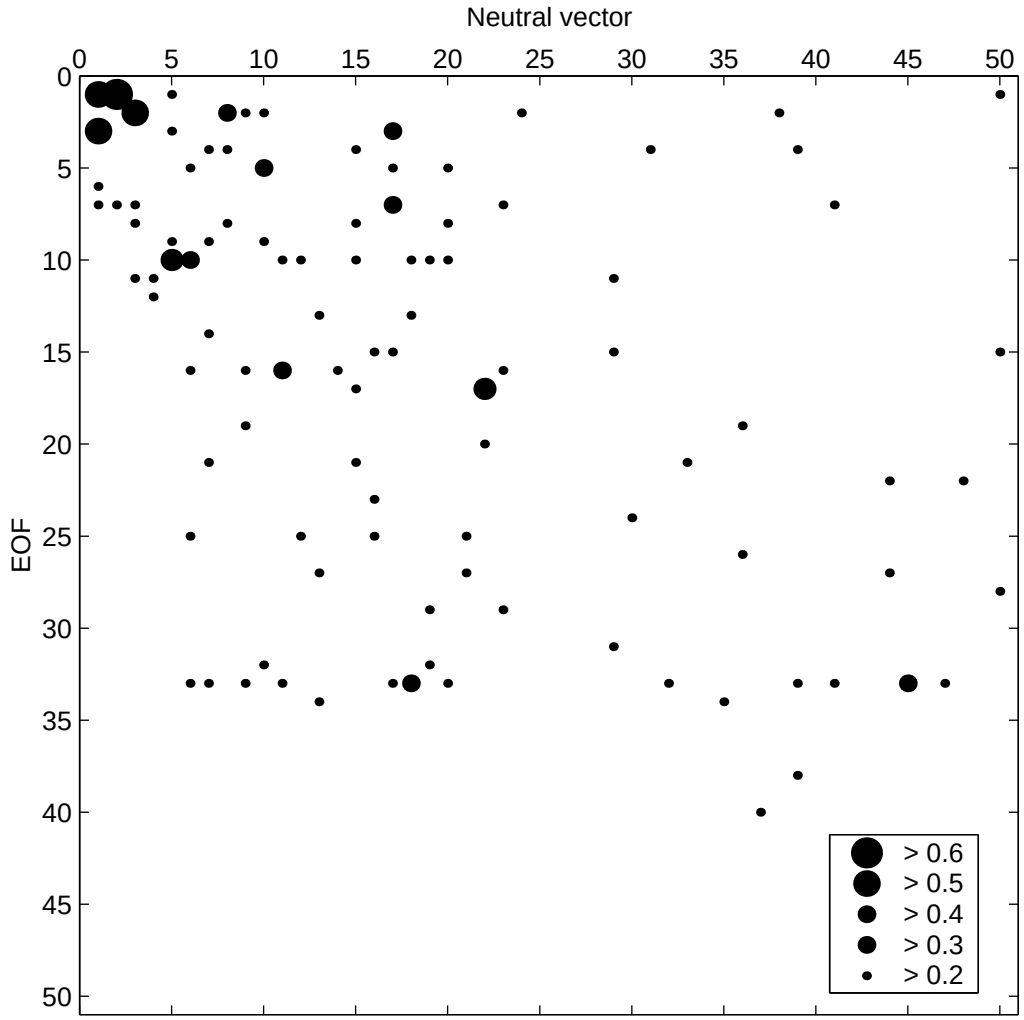

Figure 4-6: Cross-correlations between model EOFs (vertical axis) and neutral vectors computed using a KE norm (horizontal axis). The absolute value of the correlation is indicated by the size of the dots. Correlations less than 0.2 are not plotted.

between the shapes of the model EOFs (Figure 4-2) and the neutral vectors (horizontal axis). The absolute value of the correlation for each pair is indicated by the size of the dots. Correlations less than 0.2 are not plotted.

The observations discussed above are borne out in this figure: neutral vectors 1 and 2 project onto EOF 1, and neutral vector 3 projects onto EOF 2. We also see that and neutral vector 1 projects onto EOF 3. But more importantly, the strongest correlations are among the first few EOFs and neutral vectors (the large dots are clustered in the upper left corner). If the correlations arose by chance, we would

expect this figure to show a random scattering of small points throughout the domain.

We have done a rough comparison of these patterns with the results of d'Andrea (2000), who attempted to find the results which minimize the tendency of a *nonlinear* model, using a method of steepest descent. We find good agreement between some of the neutral vectors shown here and some of d'Andrea's patterns. Interestingly, in some cases, the neutrality of a mode in the nonlinear model is sign-dependent: the "positive" phase of a neutral vector may appear in d'Andrea's set of patterns with minimal tendency, while the "negative" phase may not.

Since the first few neutral vectors project strongly onto the EOFs, we should expect that a substantial amount of the model's natural variability resides in the subspace of the first few neutral vectors. Figure 4-7 demonstrates that this is the case. The three most neutral vectors explain more of the variance of a 5000-day model run than any other singular vector. The first three EOFs explain 50% of the variance of monthly means, while the first three neutral vectors explain 37% of the variance – almost as much.[1]

Many papers have been written which project observed variability onto the first few EOFs to study its statistics (Hannachi 1997; Haines & Hannachi 1995; Molteni *et al.* 1988), or which use EOFs to generate a reduced-subspace model which encapsulates most of the system's variability (Achatz & Branstator 1999; Kaplan *et al.* 2000; d'Andrea 2000). We find here that neutral vectors are almost equally good for these purposes. They also have the advantage over EOFs that they represent dynamically-important modes of the system, rather than being empirically selected.

4.3.2 Relationship between neutral vectors and EOFs

In the previous section, we observed a close connection between EOFs and neutral vector patterns. Here, we present a mathematical explanation for this connection.[2]

[1] Since EOFs, by definition, maximize explained variance, the variance explained by neutral vectors must be smaller.

[2] While writing, I found that most of the results presented in this section have been published by Navarro (1993). Since many readers will be unfamiliar with that work, and since my discussion of the importance of the $\mathbf{ff}^\dagger$ matrix goes beyond Navarro's study, I present the derivation in full here.

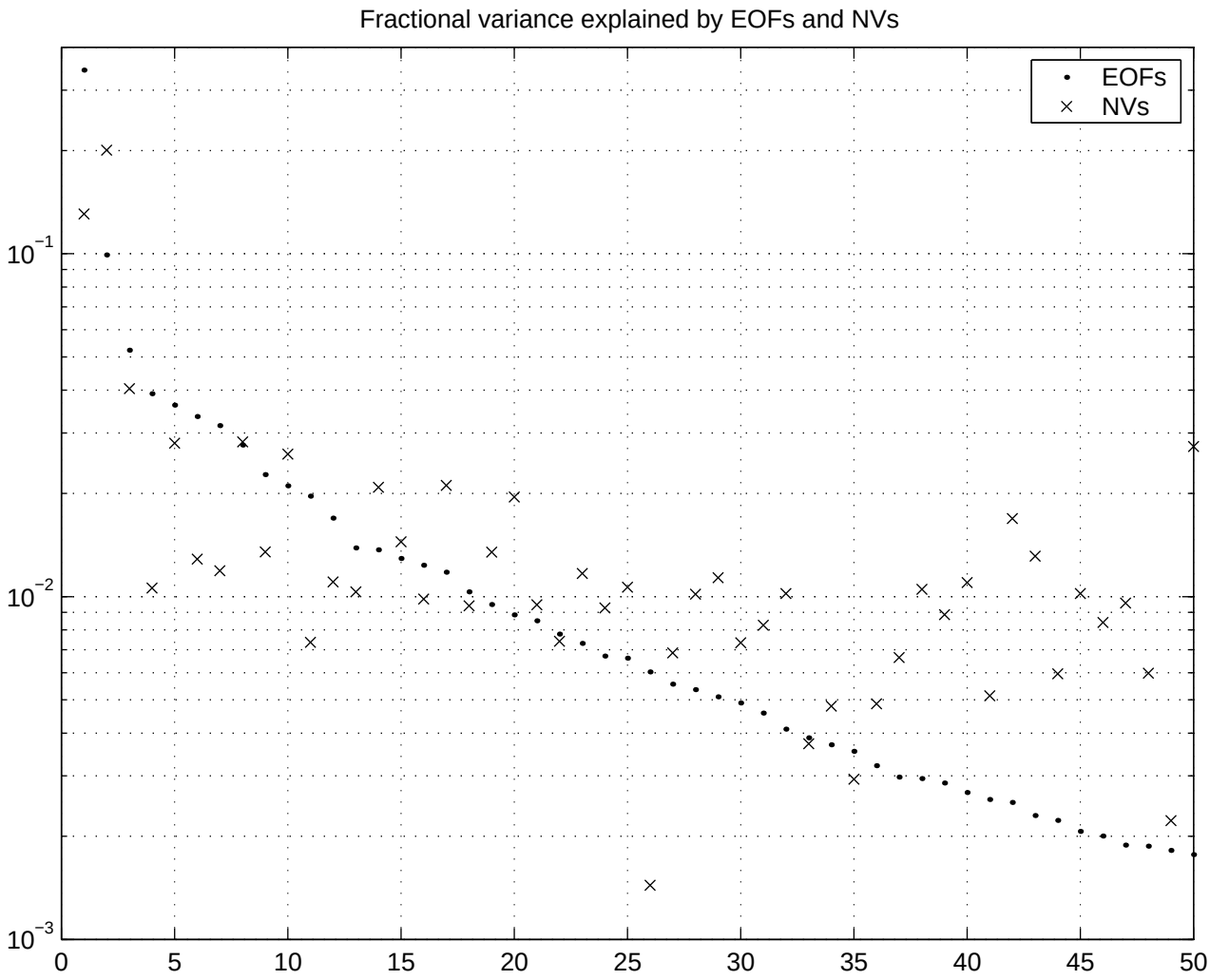

Figure 4-7: Comparison of fractional variance of monthly-mean model output explained by EOFs (dots) with variance explained by neutral vectors (x's).

Suppose the atmosphere consists of a number of "slow modes" (stationary planetary wave patterns like the NAO and PNA), which respond in a linear way to stochastic forcing generated by "fast modes" (transient eddy forcing), such that during any observation period n, the stochastic forcing $\mathbf{f}_n$ excites a planetary wave response $\mathbf{\Psi}_n$:

$$\mathbf{M}\mathbf{\Psi}_n = \mathbf{f}_n \rightarrow \mathbf{\Psi}_n = \mathbf{M}^{-1}\mathbf{f}_n$$

or, defining matrices $\mathbf{\Psi}$ and $\mathbf{f}$ whose columns are the $\mathbf{\Psi}_n$ and $\mathbf{f}_n$:

$$\mathbf{\Psi} = \mathbf{M}^{-1}\mathbf{f}$$

The EOFs are defined as the eigenvectors of the covariance matrix $\mathbf{\Psi}\mathbf{\Psi}^\dagger$:

$$\mathbf{\Psi}\mathbf{\Psi}^\dagger = \mathbf{M}^{-1}\mathbf{f}\mathbf{f}^\dagger\mathbf{M}^{-\dagger}$$

Consider for a moment the case where the eddy forcing is isotropic and spatially uncorrelated, and the equations are normalized so that $\mathbf{f}$ has unit amplitude: $\mathbf{f}\mathbf{f}^\dagger = \mathbf{I}$. Then

$$\mathbf{\Psi}\mathbf{\Psi}^\dagger = \mathbf{M}^{-1}\mathbf{M}^{-\dagger} \tag{4.6}$$

We may decompose the $\mathbf{M}$ matrix using its singular vectors thus:

$$\mathbf{M} = \mathbf{U}\mathbf{\Lambda}\mathbf{V}^\dagger \tag{4.7}$$

The columns of $\mathbf{V}$ are the right singular vectors (the neutral vectors); the columns of $\mathbf{U}$ are the left singular vectors (the optimal forcing patterns), and $\mathbf{\Lambda}$ is a diagonal matrix of singular values. Inserting this into (4.6), and using the fact that $\mathbf{V}^{-1} = \mathbf{V}^\dagger$ and $\mathbf{U}^{-1} = \mathbf{U}^\dagger$, we obtain:

$$\mathbf{\Psi}\mathbf{\Psi}^\dagger = \mathbf{V}^{-\dagger}\mathbf{\Lambda}^{-1}\mathbf{U}^{-1}\mathbf{U}^{-\dagger}\mathbf{\Lambda}^{-1}\mathbf{V}^{-1} = \mathbf{V}\mathbf{\Lambda}^{-2}\mathbf{V}^\dagger$$

Since $\mathbf{V}\mathbf{\Lambda}^{-2}\mathbf{V}^\dagger$ is in diagonalized form, its eigenvectors are $\mathbf{V}$ and its eigenvalues are

the diagonal elements of $\mathbf{\Lambda}^{-2}$. Thus, the EOFs (which are the eigenvectors of the covariance matrix $\mathbf{\Psi}\mathbf{\Psi}^\dagger$) are identical to the singular vectors of the tendency matrix. Since $\mathbf{\Lambda}$ is raised to the -2 power, the dominant EOFs correspond to the smallest singular vectors – that is, to the neutral vectors.

What happens when the transient eddy forcing covariance is *not* proportional to the identity matrix, as we assumed above? Then we have:

$$\mathbf{\Psi}\mathbf{\Psi}^\dagger = \left(\mathbf{M}^\dagger \left(\mathbf{f}\mathbf{f}^\dagger\right)^{-1} \mathbf{M}\right)^{-1} \tag{4.8}$$

The matrix $\left(\mathbf{f}\mathbf{f}^\dagger\right)^{-1}$ is the inverse of the eddy forcing covariance matrix. It is symmetric and positive definite (assuming the inverse exists). It thus has the structure and position of a weight matrix for an inner product between the $\mathbf{M}$ matrix with itself. Thus, in the presence of nonuniform stochastic forcing, we can compare the EOFs to the singular vectors of $\mathbf{M}$ computed using this unusual weight matrix $\left(\mathbf{f}\mathbf{f}^\dagger\right)^{-1}$. We demonstrate this by performing an SVD decomposition of $\mathbf{M}$ (equation (4.7)), where now the orthonormality of the $\mathbf{V}$ and $\mathbf{U}$ are defined using the inner products

$$\mathbf{V}^\dagger\mathbf{V} = \mathbf{I} \qquad \mathbf{U}^\dagger \left(\mathbf{f}\mathbf{f}^\dagger\right)^{-1} \mathbf{U} = \mathbf{I}$$

Then, using (4.7):

$$\mathbf{M}^\dagger \left(\mathbf{f}\mathbf{f}^\dagger\right)^{-1} \mathbf{M} = \mathbf{V}\mathbf{\Lambda}\mathbf{U}^\dagger \left(\mathbf{f}\mathbf{f}^\dagger\right)^{-1} \mathbf{U}\mathbf{\Lambda}\mathbf{V}^\dagger = \mathbf{V}\mathbf{\Lambda}^2\mathbf{V}^\dagger$$

And so, returning to (4.8):

$$\mathbf{\Psi}\mathbf{\Psi}^\dagger = \left(\mathbf{M}^\dagger \left(\mathbf{f}\mathbf{f}^\dagger\right)^{-1} \mathbf{M}\right)^{-1} = \mathbf{V}\mathbf{\Lambda}^{-2}\mathbf{V}$$

Thus, the principal EOFs of this system are the neutral vectors ($\mathbf{V}$), where the SVD analysis used to compute the neutral vectors uses the inverse of the stochastic forcing correlation matrix as a weight matrix to normalize the optimal forcing patterns ($\mathbf{U}$).

What is the significance of this odd weight matrix $\left(\mathbf{f}\mathbf{f}^\dagger\right)^{-1}$? Consider the simple

case where each vector element represents a location in space, and the stochastic forcing is spatially uncorrelated but inhomogeneous. Then the eddy forcing covariance matrix will be diagonal, with larger elements on the diagonal where forcing is strong. Thus the weight $\left(\mathbf{f}\mathbf{f}^{\dagger}\right)^{-1}$ is small where the eddy forcing is large. In computing neutral vectors, we want to minimize the forcing needed to excite them. A forcing pattern will be "small" with respect to this weighted norm when it has small amplitude where the weight is large, and vice versa. Thus, the SVD analysis selects neutral vectors whose forcing patterns are localized at the site of large eddy forcing.

This allows us to explain the observation made in Section 4.3.1 that the dominant EOFs all lie within the northern hemisphere, while the neutral vectors reside in both hemispheres, unless we force them into the north using an artificial hemispheric damping. High-frequency eddy activity, and thus eddy forcing, are far stronger in the northern hemisphere (where it's wintertime). Thus, neutral vector patterns sensitive to northern-hemisphere forcing will be driven more strongly, and so northern-hemisphere modes will be more prominently visible in the model output, even though they're no more "neutral" than southern-hemisphere modes.

To observe a closer connection between EOFs and neutral vectors, we should compute neutral vectors using a norm weighted with the inverse eddy forcing covariance, rather than any more traditional norm. It is not easy to build this forcing covariance matrix from observations alone, but since eddy flux is proportional to eddy strength, using the covariance of high-frequency eddy streamfunction instead might give good results.

4.4 Optimal forcing patterns

4.4.1 Optimal forcing pattern structure

The pattern which maximally excites neutral vector 1 (left column of Figure 4-3) shows two broad regions of sensitivity of opposite signs: one focused on Kamchatka and extending over the east Pacific and Siberia, and a second focused on the tropical

Pacific and covering Africa, Europe, the North Atlantic, and North America. The pattern is baroclinic, with an out-of-phase response in the lower two layers and nearly zero sensitivity at the upper level. This implies a sensitivity to low-level heating – which hints that this mode may be sensitive to forcing by SST anomalies.

The second optimal forcing pattern (left column of Figure 4-4) shows a sensitivity to low-level PV forcing over much of the North Pacific, particularly the Sea of Okhotsk, and to an opposite sign of forcing over the North Atlantic and the Arctic. Once again, the mode is sensitive to low-level heating.

The optimal forcing pattern for neutral vector 3 (Figure 4-5) also shows a global-scale dipole, with sensitivity to low-level baroclinic forcing. The forcing centers lie at the beginning and end of the PNA-like wave train.

If we stopped here, we would conclude that the optimal forcing patterns are most sensitive to broad-scale, low-level thermal forcing. In some cases (like Figure 4-5, in which forcing centers lie at the beginning and end of the wave train), the spatial relationship of forcing to response makes sense, while in others (like Figure 4-3, in which an east-west dipole pattern gives rise to a zonally symmetric structure), it's not so obvious.

However, this analysis has chosen to use an inner product in (4.4) in which the norm of a streamfunction vector is proportional to its kinetic energy. This is only one of a wide array of sensible choices of inner product. For example, we could choose an inner product where the norm of $\mathbf{\Psi}$ was proportional to the root-mean-square streamfunction rather than the kinetic energy. We could also attempt to minimize the PV tendency rather than the streamfunction tendency, or use an inner product which applied different weights to different geographical areas or vertical levels (see Appendix B).

We find that while the neutral vectors are relatively insensitive to the choice of inner product, the optimal forcing patterns look very different for different inner products. This is demonstrated in Figure 4-8, which shows the first neutral vector and optimal forcing pattern using an inner product in which $||\mathbf{\Psi}||$ is proportional to the root-mean-square streamfunction anomaly, which we call the "psi norm".

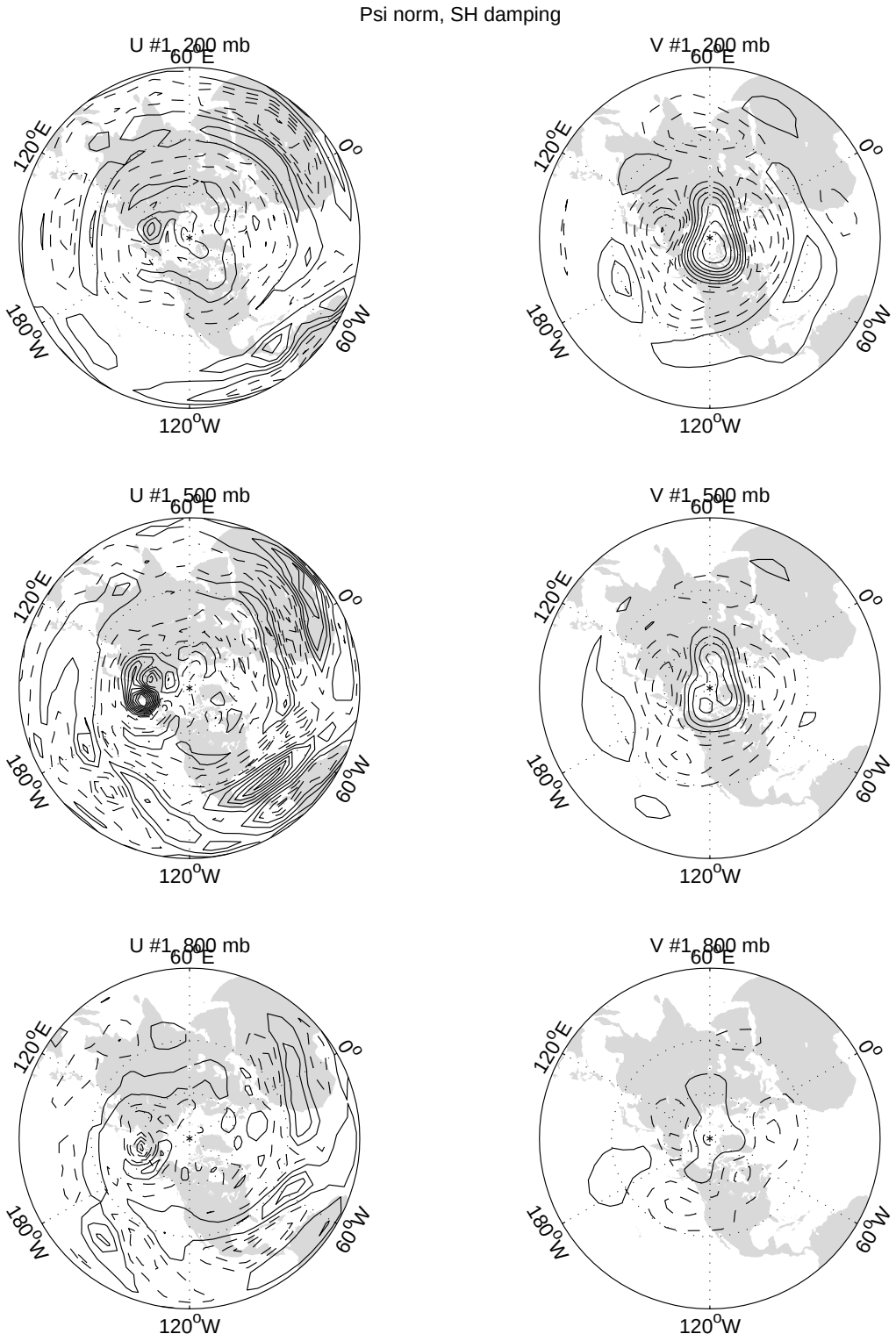

Figure 4-8: Right column: Neutral vector #1 for model climatology, Psi inner product. Left column: corresponding optimal forcing pattern. Compare with Figure 4-3

The first neutral vector for the psi norm looks virtually identical to the first neutral vector of the KE norm. However, the optimal forcing pattern looks radically different. Rather than being characterized by a planetary-sized dipole structure, we see many narrow, closely-spaced zones of positive and negative sensitivity. These tend to be strongest in the tropics, where, as we have already mentioned, the model's dynamics are the least believable; they also occur to some extent in the southern hemisphere (not shown in this polar projection). The tendency for the optimal forcing to be low-level heating remains, but is much less prominent. With the exception of a strong sensitivity to mid-layer forcing over eastern Siberia, the first optimal forcing patterns of the KE and psi norms look completely different.

We have tried several other choices of norm, including an attempt to minimize PV tendency (as done in (3.11)) rather than streamfunction tendency; we find very generally that neutral vectors are not strongly dependent on the norm we choose, while the optimal forcing patterns are highly norm-sensitive.

4.4.2 Norm-sensitivity of optimal forcing patterns

Why do the two norms display identical neutral vectors if their optimal forcing patterns so different? Consider the atmospheric response equation $\mathbf{M\Psi} = \mathbf{f}$. A neutral vector has small $\mathbf{f}$, so the neutral vector algorithm selects the components of $\mathbf{\Psi}$ to ensure the near-cancellation of the various terms in the $\mathbf{M}$ matrix. This cancellation is independent of the norm selected, so the neutral vector pattern is not norm-sensitive. However, relatively large changes in $\mathbf{f}$ can result from relatively small changes in $\mathbf{\Psi}$, since the left side of the equation is a difference of small terms. If the norm penalizes one sort of pattern more heavily, the amplitude of that pattern in $\mathbf{f}$ can be made small with only small changes to $\mathbf{\Psi}$.

The psi norm applies equal weight to all wavenumbers, while the KE norm penalizes high wavenumbers (for which $\nabla\psi$ is large) more heavily. As a result, the KE optimal forcing patterns are more broad-scale. However, this analysis cannot tell us whether one norm is "better" than another.

While I was in the process of performing these computations, the potential for

norm-sensitivity was pointed out by Grant Branstator (1999). However, the norm-sensitivity we found could not have been definitely predicted before attempting the experiment. A system in which less cancellation of terms within $\mathbf{M\Psi}$ was possible (for example, a heavily-damped system) would have less perfect neutral vectors, and would also be less norm-sensitive. A trade-off exists between the perfection of neutral vectors and the sensitivity of optimal forcing patterns. Unfortunately, it turns out that this system does not lie within a useful middle ground where both neutral vectors and optimal forcing patterns are well-defined. This is indicated by the value of eigenvalue λ_1 corresponding to the most neutral pattern. It corresponds to a timescale of about two years – incredibly long compared to the dominant timescales of the terms in the PV equation (a week or two), implying almost perfect cancellation of terms. This maximizes the importance of the neutral vectors in explaining model variability, but minimizes the utility of the optimal forcing patterns.

This phenomenon can also be explained in terms of the condition number of the $\mathbf{M}$ matrix (defined as the ratio of the largest and smallest singular values). When this number is large, the matrix is "poorly conditioned", and the response $\mathbf{\Psi}$ is sensitive to small perturbations in $\mathbf{f}$ or $\mathbf{M}$. A singular matrix has an infinite condition number. For our $\mathbf{M}$, the condition number is of the order 10^4, implying rather large sensitivity to forcing, but we must stress that the matrix is *not* close to being singular to within machine precision.

Navarro (1993) performed an essentially identical neutral vector analysis on a barotropic model, using the January 300-mb climatological flow. His neutral vector patterns look completely different from those found in this analysis, and are much less similar to observed patterns like the NAO, PNA, and AO. However, Navarro's work agrees that the neutral vectors strongly resemble the model's EOFs, and that the condition number of the $\mathbf{M}$ matrix is relatively large, leading to large sensitivity to forcing. Interestingly, Navarro's optimal forcing patterns show some similarity to those shown in Figure 4-8, particularly in their fine-scale, zonally-oriented bands of sensitivity in the tropics.

4.4.3 Response of the nonlinear model to "optimal" forcing

We have found in Section 4.4.1 that the optimal forcing patterns are difficult to define unambiguously, since they vary dramatically between different definitions of the inner product. Nevertheless, it is useful to find out whether these patterns, which are optimal in forcing the linearized stationary planetary wave model, are also optimal in forcing the full non-linear time-evolving model. If this model were quasi-linear, we would expect to see a large neutral vector response to optimal forcing. However, nonlinear effects may spoil this correspondence. If the optimal forcing patterns found using the linear model do not excite a strong response in the nonlinear model, we cannot expect them to tell us much about the sensitivity of the true atmosphere to PV forcing.

We want to find the time-mean perturbation response to a constant "optimal" forcing perturbation. We proceed by running three integrations of Molteni's model. First, we create a pair of control runs (runs 1 and 2), where S_n in (4.1) are unchanged from the specification described in Section 4.1. These two runs are initialized with very slightly different initial conditions, and so produce different instances of synoptic eddies. The difference between the mean state of these two runs will give us some idea of the uncertainty of the mean, with which we can compare the experimental run.

In the experimental run (run 3), we perturb S_n by a small amount in the direction of the first optimal forcing pattern for the KE norm (left column of Figure 4-3). Of course, we perform a PV inversion to convert the optimal forcing pattern from a streamfunction forcing to a PV forcing. The amplitude of this forcing amounts to about 4% of the basic-state value of S. We expect that the difference in the mean states of runs 1 and 3 should look like KE neutral vector 1 (right column of Figure 4-3).

All three runs are performed for 10,000 days of integration; the run length was increased in order to reduce the uncertainty of the sample mean fields.

The top panel of Figure 4-9 shows the difference in the means of the two unper-

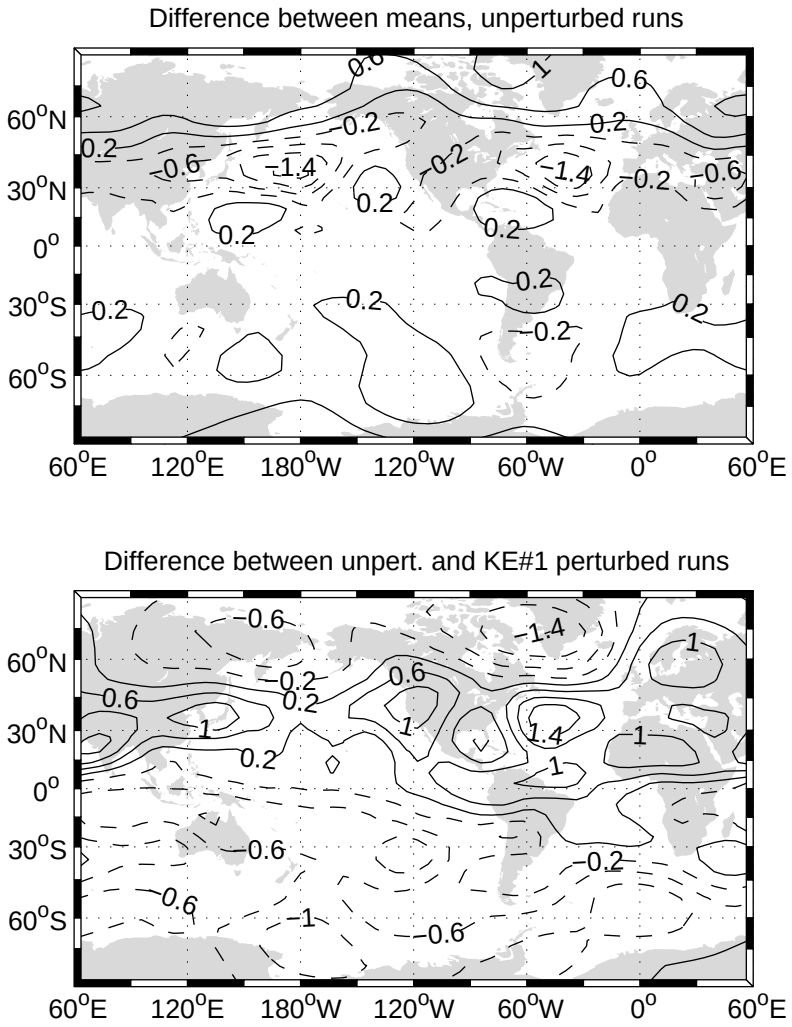

Figure 4-9: Response of the nonlinear model to "optimal" forcing. Top: Streamfunction difference between 10000-day means of two unperturbed model runs at 500 mbar is shown; contour interval is $.4 \cdot 10^5$ m^2/s. Bottom: 500-mbar streamfunction response to forcing with the KE optimal forcing pattern #1.

turbed runs. We see differences in the means of order 10^5 m^2/s. The bottom panel shows the difference between the means of perturbed and unperturbed runs. The differences are likewise of order 10^5 m^2/s. Thus, any response seen is indistinguishable from the noise. One might argue that while the amplitude is small, a structure reminiscent of neutral vector 1 is seen in the response. However, this same structure is seen in the top panel too[3], so that doesn't prove anything.

The the linearized model responds to the forcing with the first neutral vector pattern (right column of Figure 4-3), with an amplitude[4] of about $6 \cdot 10^7$ m^2/s. The upper limit on the nonlinear model's response to the forcing is less than 1% of this. Thus, we conclude that the "optimal" forcing patterns are ineffective at exciting the nonlinear model.

Why? Take the time-average of the PV equation solved by the model (4.1):

$$J(\overline{\psi}, \overline{q}) = -D(\overline{\psi}) + \overline{S} - \overline{J(\psi', q')} \tag{4.9}$$

Barred terms represent time means; primed terms represent time-fluctuating terms with zero time mean. Now, consider the time-average balance of PV when we apply a forcing perturbation, S_{nv}. We denote the streamfunction and PV of the response to forcing as ψ_{nv} and q_{nv}.

$$J(\overline{\psi} + \psi_{nv}, \overline{q} + q_{nv}) = -D(\overline{\psi} + \psi_{nv}) + \overline{S} + S_{nv} - \overline{J(\psi', q')} \tag{4.10}$$

We expand the terms in (4.10) and take the difference between it and 4.9. We assume

[3]Why does the difference between unperturbed runs show neutral vector structure? The uncertainty of the sample mean is $\sigma/\sqrt{N}$, where σ is the standard deviation and N is the number of independent observations. Most atmospheric patterns show little persistence on timescales longer than a week. But the neutral vectors evolve very slowly, persisting for months or longer. Thus the N appropriate for the neutral vectors is abnormally small; the sample mean amplitude of the "fast" modes converges more quickly than the sample mean amplitude of the neutral vectors as we integrate for longer. In the limit of very long integrations, the residual of sample means will have its structure dominated by the neutral vectors.

[4]This is more than 30% of the amplitude of the model's mean state. While the forcing perturbation is a small fraction of the basic-state forcing, the linear response is a large fraction of the basic-state streamfunction, precisely because the forcing perturbation is "optimal". We recognized that a response this large would not fully satisfy linearity conditions; the experiment shown here was a "first try", with an intentionally large forcing to make the response as obvious as possible.

the perturbation is small enough that the eddy forcing $\overline{J(\psi', q')}$ is unchanged.

$$J(\overline{\psi}, q_{nv}) + J(\psi_{nv}, \overline{q}) = -D(\psi_{nv}) - J(\psi_{nv}, q_{nv}) = S_{nv}$$

The terms which are linear in ψ_{nv} are just the terms which make up the linearized tendency operator $\mathbf{M}^*$ in (4.2):

$$\mathbf{M}^*(\psi_{nv}) - J(\psi_{nv}, q_{nv}) = S_{nv} \tag{4.11}$$

This equation differs from the linear forcing response equation by the presence of the term $J(\psi_{nv}, q_{nv})$. Generally, for small forcing perturbations, this term is small. However, we're supplying a forcing which excites a neutral vector. Therefore, both $\mathbf{M}^*(\psi_{nv})$ and S_{nv} are unusually small. In fact, if we assume the response is linear, and use $\mathbf{M}^*\psi_{nv} = S_{nv}$ to calculate ψ_{nv} and then check our assumption by plugging that ψ_{nv} into the nonlinear Jacobian term, we find that the Jacobian term is 600 times larger than the forcing! Since the amplitude of the forcing term is proportional to the streamfunction, while the amplitude of the Jacobian term is proportional to the square of the streamfunction, we must make the forcing (and thus the response) 600 times smaller to make $J(\psi_{nv}, q_{nv}) \sim S_{nv}$. This means that the nonlinear self-advection of the response dominates the forcing unless the response amplitude is smaller than 10^5 m^2/s. This amplitude is indistinguishable from the noise.

A possible solution to this problem was suggested by Franco Molteni (personal communication, 2000). One could add a quantity to the forcing perturbation S_{nv} which cancels out the contribution of the nonlinear Jacobian term in (4.11). Thus a large neutral-vector response could be excited which did not imbalance the PV equation. One difficulty here is that we carefully selected the optimal forcing pattern to maximally excite a response, but when we add this extra forcing term, the resulting pattern is no longer necessarily "optimal" in either its linear or nonlinear response. The correct solution to this problem is to perform a *nonlinear* optimization of the response to forcing.

4.5 Conclusions

The results of this chapter are mixed. We find that the neutral vectors of Molteni's 3-layer model closely resemble the EOFs of that model, even though the EOFs are computed from data generated by a nonlinear model integration, and the neutral vectors arise from singular vector decomposition of a linearized model. The neutral vectors explain almost as much of the nonlinear model's variance as the EOFs do; this indicates their importance in understanding model variability, and makes them useful in constructing reduced-subspace models of atmospheric variability. We have demonstrated that, if one assumes that the EOFs result from linear excitation of relatively slow modes by transient eddy PV forcing, then one can demonstrate that the patterns of EOFs and neutral vectors are mathematically identical. The caveat to this is that the neutral vectors must be computed using an inner product weighted by the inverse of the eddy forcing covariance.

Thus, neutral vectors appear to be a very useful concept in studying the low-frequency variability of the atmosphere. Their advantage over EOFs is that they have a simple physical interpretation – they are the most slowly-evolving patterns within the atmosphere, the patterns for which advection of PV anomalies nearly balances their tendency to propagate as Rossby waves.

These results lead to the following tempting, though speculative chain of logic: Fluctuations of EOF patterns like the NAO and PNA account for much of the atmosphere's interannual variability. The EOFs of the observed atmosphere look like this model's neutral vectors. Since the neutral vectors are, in the linear model, the patterns which most strongly respond to forcing, we are led to suspect that if any atmospheric modes are involved in interannual atmosphere-ocean coupled interactions of the sort discussed in Chapters 2 and 3, the NAO and its relatives should be. Even if the specific dynamics of those chapters are not active, the high linear sensitivity of the neutral vectors makes them a useful paradigm for the study of atmosphere-ocean interaction.

Observations (see Chapter 1) show that patterns like the NAO and its relatives

dominate both the intraseasonal and the interannual variability of the atmosphere. The neutral vector paradigm gives one of several possible explanations for this. Neutral vectors are the patterns which respond most strongly to forcing in the linear model. High-frequency forcing from transient eddies will generate short-term variability, while low-frequency forcing from SST anomalies or other processes will lead to interannual variability. The same pattern is easily excited by both intrinsic and extrinsic forcing of the atmosphere.

While neutral vectors are a powerful tool for understanding the atmosphere's variability, the optimal forcing patterns appear to be much less useful. While their structure suggests that the neutral vectors may be easily excited by low-level baroclinic forcing, such as would arise from heating generated by SST anomalies, their patterns are not robust. We can get wildly different "optimal" forcing patterns by using a different inner product in our singular vector decomposition. This is because the optimal forcing patterns are the small residual differences between large terms in the atmospheric response equation, so small differences in the analysis can make huge differences in the results. The neutral vectors do not display this sensitivity. Even worse, the optimal forcing patterns are ineffective in exciting a large response in the full nonlinear model. This is because the nonlinear self-interaction of the response to forcing dominates over the forcing itself, unless that response is immeasurably small.

This may make it difficult to generalize the coupled atmosphere-ocean interaction which was discussed in Chapters 2 and 3 to more complicated models of air-sea interaction. While the neutral vectors are the most sensitive to forcing (including forcing arising from SST anomalies) in linear models, they are not very responsive in the nonlinear model discussed in Section 4.4.3. In addition, our discussion of the interaction between neutral vectors and the ocean in Section 3.2.2 hinged on the idea that, as SST anomalies moved around, they projected onto first one, then another of the optimal forcing patterns. Each strong projection excited a neutral vector response, which fed back onto the ocean. Here, we find that the shape of the optimal forcing patterns is not robust. As a result, the regular alternation of projection necessary for the coupled wave will be difficult to identify, if it occurs at all.

Chapter 5

Summary and future projects

5.1 Summary

In Chapter 2, we discovered that, under favorable circumstances, the interaction of atmospheric and oceanic Rossby waves can lead to a coupled growing mode. Undulations of the ocean thermocline produce SST anomalies through advection and entrainment; these excite a stationary wave response to thermal forcing in the atmosphere, and the resulting wind-stress feeds back upon the ocean thermocline through Ekman pumping. The propagation of thermocline undulations as Rossby waves causes the entire pattern to move slowly westward. This mode is roughly as large as an ocean basin, has barotropic atmospheric structure, a roughly decadal period, and a growth rate corresponding to an e-folding time of several years. The wavelength and phase correspondence of the mode resembles the North Atlantic Oscillation and (to a lesser extent) the Antarctic Circumpolar Wave. Interestingly, enhanced interannual and decadal variability have been reported in both of these observed patterns.

The analytical model presented in Chapter 2 is oversimplified in many respects, including its use of an unbounded domain and a spatially-invariant atmospheric background flow. We addressed these simplifications in Chapter 3. There, by recomposing the coupled physics in a numerical model, we were able to consider the effect of a re-entrant channel atmosphere, a closed ocean basin, and a varicose atmospheric background flow. We found that the coupled dynamics remains important in all

these cases. When confined to an ocean basin, the coupled mode becomes damped. This occurs because westward-propagating oceanic Rossby waves are destroyed at the ocean's the western boundary. Nevertheless, the coupled mode is most easily excited by stochastic forcing. A varicose atmospheric background flow breaks the isotropy of the atmospheric equations: the atmospheric component of the pattern no longer propagates westward, but exhibits standing oscillations at preferred longitudes. This increases the resemblance of the coupled mode to the NAO and similar patterns. We concluded with the observation that the atmospheric dynamics of the coupled model are essentially identical to the "neutral vectors" (defined as the minimum singular vectors of the model tendency matrix) discussed by Marshall and Molteni (1993). This makes sense because, as we showed, the neutral vectors are the patterns which react most strongly to anomalous forcing.

In Chapter 4, we considered these neutral vectors in more detail, using Molteni's 3-layer quasigeostrophic atmospheric model. We found a strong similarity between the model's EOFs and its neutral vectors. Similarity between these patterns and EOFs of the observed atmosphere (such as the NAO and its relatives) is also strong, and the neutral vectors explain much of the atmosphere's variability. We showed mathematically that there is a strong mathematical connection between EOFs and neutral vectors. Since the neutral vectors react most strongly to forcing (including SST forcing), and since the neutral vectors strongly resemble dominant modes of the observed atmosphere such as the NAO and PNA, these observed patterns are the most likely to be involved in atmosphere-ocean interaction. However, we find that while the neutral vectors are clearly defined and very useful, the "optimal forcing patterns" which excite them are much less so. Solving for these patterns is not a well-posed problem, and the results vary greatly with small changed in technique. In addition, these patterns are *not* successful in exciting a strong response from a nonlinear model.

This work has made some progress in identifying atmospheric patterns which are likely to be involved in atmosphere-ocean coupled interaction, and in identifying mechanisms by which that interaction might occur. However, many uncertainties

remain, particularly in computing the sensitivity of these patterns to SST forcing. We now discuss ways to address some of these problems.

5.2 Future work

A moderate number of relatively small projects were suggested in the text of this paper, which could be easily performed in a relatively short time. We discuss these first, followed by some longer-term projects which expand upon the current work.

First, we could add a basic-state oceanic current to the numeric model of coupled interaction described in Chapter 3. A double-gyre configuration of currents is the obvious choice. Since the period of oceanic baroclinic Rossby waves (which currently sets the oscillation timescale of the model) is comparable to the gyre revolution time, we expect the coupled mode to be significantly modified by this addition. However, the basic interaction mechanism discussed in Chapter 3 (in which different atmospheric neutral vectors are excited as SST anomalies move around, the neutral vectors providing a feedback forcing to the ocean) can still occur, even if the SST anomalies are transported by the mean flow rather than moving in sync with Rossby waves. Whether a positive feedback is possible depends on the details of the interaction.

In Section 4.3.2, we predicted that the similarity of EOFs to neutral vectors would be improved if the neutral vectors were computed using the inverse of the eddy forcing covariance matrix as the weight matrix for the inner product. This prediction should be checked. The key difficulty lies in computing the covariance of the eddy forcing matrix. One could compute the covariance of monthly-average (say) values of $J(\psi', q')$. Alternately, one could simply suppose that the magnitude of eddy forcing is roughly proportional to the strength of the eddies, and use the covariance of eddy streamfunction itself. The similarity of EOFs and neutral vectors may still not be perfect because of our assumption in Section 4.3.2 that the "slow modes" respond in steady-state fashion to the eddy forcing.

In Section 4.4.3, we hypothesized that a large response to forcing could be produced by adding to the forcing a quantity which canceled out the nonlinear advection

term in 4.11. This is easy enough to check, even if its implications are unclear (see the last paragraph of 4.4.3).

The most obvious of the longer-term projects we contemplate is to look for evidence of the coupled mode described in Chapter 2 in a nonlinear coupled climate model or in observations. The simplest possible coupled model might be the Molteni QG model coupled to a simple ocean model, but the investigation could be done in a GCM of arbitrary complexity. We expect the difficulty in identifying the mode to increase with model complexity. The observation which will most unambiguously identify the coupled mode is a spatial covariance of warm SST, an atmospheric high, and a depressed thermocline. However, depending on what happens when we add a basic-state ocean current to our simple coupled model as discussed above, a coupled interaction might be possible without a strongly undulating thermocline.

The existence of a linearized version of the Molteni model makes it particularly easy to use to compute neutral vectors. However, there are some drawbacks to this model. It does not adequately simulate tropical dynamics, and it does not have a good representation of thermal forcing (surface heat fluxes, radiative-convective schemes, etc.). Most notably, few-layer QG models have been criticized by Lindzen *et al.* (1968), who claims that their vertical structure permits spurious resonances to occur. Since resonances are exactly what we're looking for in computing neutral vectors, this is cause for concern; however, Panetta *et al.* (1987) dispute the seriousness of this objection. In any case, many of these problems go away if we compute the neutral vectors of a primitive equation model of the atmosphere. While difficulties in interpretation may diminish, procedural difficulties in computing the neutral vectors increase dramatically. Since primitive equation models generally have many more variables than a QG model of similar resolution, the size of the matrix whose singular vectors must be computed increases dramatically. Unless we can restrict the domain of the problem (see Appendix B for a discussion of the difficulty in doing this), we may have to accept much longer computation times.

One issue which was avoided in the description of the Molteni model's linear response to thermal forcing was the change in synoptic eddy PV flux which arises as a

result of changes in the time-mean flow. That is, we tacitly assumed that $\overline{J(\psi', q')}^t$ was insensitive to changes in the time-mean flow $\overline{\psi}^t$. This is not the case: eddy activity depends on the mean flow. To the extent that this dependence is linear, it adds an additional contribution to the linearized tendency matrix $\mathbf{M}$. Such a linear model of the sensitivity of eddy forcing to changes in time-mean flow is called a "storm-track model" (Branstator, 1995). It would be interesting to see how the neutral vector patterns are influenced by the addition of a storm-track model to $\mathbf{M}$. One slight difficulty is that construction of storm-track models is computationally demanding, since it involves computing $\overline{J(\psi', q')}^t$ for every possible linearly independent perturbation of $\overline{\psi}^t$.

One of the conclusions of Chapter 4 is that nonlinear self-interaction is crucial to understanding the response of the atmosphere to PV forcing anomalies. D'Andrea (2000) has performed the equivalent of a "neutral vector" computation on the nonlinear steady-state response equation, using a method of steepest descent. Using the results of this study, and extending it to find the nonlinear equivalent of optimal forcing patterns, one could analyze the nonlinear sensitivity of the model to forcing in a manner analogous to the approach used here with a linear model.

Finally, if what one really wanted to do was to compute the sensitivity of the NAO (or one of its relatives) to SST forcing, one could do precisely that, without using neutral vectors as intermediaries. We can imagine setting up an adjoint problem using a large GCM, in which we directly computed the sensitivity of an NAO-like cost function to perturbations in SST. This is a very large project, and there are two difficulties here. First, this essentially an adjoint approach to the time-honored problem of determining the atmospheric response to a prescribed SST anomaly (see, for example, Palmer and Sun (1985), Kushnir and Held (1996)). Since the response in such experiments depends greatly on the choice of model used, it is possible that the adjoint problem we contemplate will be similarly sensitive. Secondly, Tom Haine (2000) has suggested that computing this sort of adjoint sensitivity experiment system with chaotic elements (such as synoptic eddies), which show sensitive dependence on boundary conditions, may be fundamentally ill-posed.

Broadly speaking, I feel that progress toward understanding the degree to which coupled interaction shapes interannual variability of the atmosphere and ocean depends on two factors. The first is robust determination, using a variety of atmospheric models and data, of how the atmosphere responds to SST forcing. The second is improved observations and analysis of atmosphere/ocean interaction on long timescales. At the moment, atmospheric models react to SST forcing anomalies in wildly different ways (Latif & Barnett, 1994, Kushnir & Held, 1996), and our observations of the atmosphere-ocean system are so incomplete and ambiguous that we do not know what the models *should* be doing. The neutral vector paradigm in particular can help us gain understanding of how and why atmospheric models differ in their response to forcing, and may eventually lead to better understanding of atmosphere-ocean interaction.

Appendix A

The effect of strong potential vorticity diffusion on the coupled model

Peter Stone (1999) and others have (quite rightly) been concerned about the magnitude of diffusion within the atmosphere of the coupled model. The atmosphere seethes with eddies, which play a large role in transporting PV within it. The simplest parameterization for the effect of transient eddies on the mean PV gradient is as a diffusive process. Dr. Stone suggested that an appropriate value for the eddy PV diffusivity κ in the atmosphere was roughly 10^6 m^2/s. The analytical model discussed in Chapter 2 has zero diffusion, while the numerical model discussed in Chapter 3 uses only enough diffusion to provide numerical stability, and has a diffusion constant $\chi \approx 1.4 \cdot 10^4$ m^2/s.

In this appendix, we discuss the effect of potential vorticity diffusion on the 2-layer atmospheric models used in Chapters 2 and 3. We present an analytical derivation of the changes to the analytical model of Chapter 2, and will briefly discuss extension of these results to the numerical model of Chapter 3.

A.1 Changes to the GM99 model equations

We parameterize the effects of transient eddies as a diffusive PV flux within the atmospheric PV equations (2.8):

$$\begin{aligned} J(\psi_2, q_2) &= \frac{gHS}{2fL_a^2} + \boxed{\chi_1 \nabla^2 q_1} \\ J(\psi_1, q_1) &= -\frac{gHS}{2fL_a^2} + \boxed{\chi_2 \nabla^2 q_2} \end{aligned}$$

For this derivation, we make the simple assumption that the diffusion constants χ_n are horizontally invariant. However, they cannot be the same in both layers, for reasons to be discussed in Section A.2. Taking sums and differences of the PV equations as was done in (2.9) and (2.10), and defining $\widehat{\chi} = \chi_1 + \chi_2$ and $\widetilde{\chi} = \chi_1 - \chi_2$:

$$\begin{aligned} J(\widehat{\psi}, \widehat{q}) + J(\widetilde{\psi}, \widetilde{q}) &= \boxed{\widehat{\chi}\nabla^2\widehat{q} + \widetilde{\chi}\nabla^2\widetilde{q}} \qquad \text{(barotropic)} \\ J(\widetilde{\psi}, \widehat{q}) + J(\widehat{\psi}, \widetilde{q}) &= -\tfrac{2gHS}{fL_a^2} + \boxed{\widehat{\chi}\nabla^2\widetilde{q} + \widetilde{\chi}\nabla^2\widehat{q}} \qquad \text{(baroclinic)} \end{aligned}$$

We now proceed to linearize the equations about a zonally-uniform basic state, as done on page 23. We find that equations (2.25) and (2.26) now become:

$$\widehat{U}\frac{\partial}{\partial x}\nabla^2\widehat{\psi} + \widehat{\beta}\frac{\partial}{\partial x}\widehat{\psi} + \widetilde{U}\frac{\partial}{\partial x}\nabla^2\widetilde{\psi} = \boxed{\widehat{\chi}\nabla^4\widehat{\psi} + \widetilde{\chi}\nabla^2(\nabla^2 - \tfrac{1}{L_a^2})\widetilde{\psi}}$$

$$\widetilde{U}\frac{\partial}{\partial x}\nabla^2\widehat{\psi} + \widetilde{\beta}\frac{\partial}{\partial x}\widehat{\psi} + \widehat{U}\frac{\partial}{\partial x}(\nabla^2\widetilde{\psi} - \frac{2}{L_a^2}\widetilde{\psi}) + \widehat{\beta}\frac{\partial}{\partial x}\widetilde{\psi} = \frac{4}{L_a^2}\gamma_a(\widetilde{\psi} - \frac{1}{r_a}\mathrm{SST}') + \boxed{\widetilde{\chi}\nabla^4\widehat{\psi} + \widehat{\chi}\nabla^2(\nabla^2 - \tfrac{1}{L_a^2})\widetilde{\psi}}$$

Looking for plane wave solutions as in Section 2.2.1, we obtain

$$-\widehat{U}ik\kappa^2\widehat{\psi} + \widehat{\beta}ik\widehat{\psi} - \widetilde{U}ik\kappa^2\widetilde{\psi} = \boxed{\widehat{\chi}\kappa^4\widehat{\psi} + \widetilde{\chi}\kappa^2\kappa_a^2\widetilde{\psi}} \tag{A.1}$$

$$-\widetilde{U}ik\kappa^2\widehat{\psi} + \widetilde{\beta}ik\widehat{\psi} - \widehat{U}ik\kappa_a^2\widetilde{\psi} + \widehat{\beta}ik\widetilde{\psi} = \frac{4}{L_a^2}\gamma_a(\widetilde{\psi} - \frac{1}{r_a}\mathrm{SST}) + \boxed{\widehat{\chi}\kappa^2\kappa_a^2\widetilde{\psi} + \widetilde{\chi}\kappa^4\widehat{\psi}} \tag{A.2}$$

As a result this change, when we use (A.1) to solve for μ (the ratio of barotropic to

baroclinic streamfunction), we obtain

$$\mu \equiv \frac{\widetilde{U} - \boxed{i\kappa_a^2 \widetilde{\chi}/k}}{\widehat{U} - \widehat{\beta}/\kappa^2 - \boxed{i\kappa^2 \widehat{\chi}/k}} \tag{A.3}$$

instead of (2.32). Notice that μ now has an imaginary component, rather than being purely real as in Chapter 2. As a result, the modes will have a difference in phase between the upper and lower layers. This phase tilt allows the Rossby waves to carry PV to balance the diffusive PV transport.

As before, we now use μ to eliminate $\widehat{\psi}$ from (A.2). Equation (2.35) now becomes:

$$\left(1 + i\frac{\nu}{\Gamma} + \boxed{\frac{\kappa_a^2 \widehat{\chi}}{\Gamma} - \frac{\kappa^2 \widetilde{\chi}\mu}{\Gamma}}\right) \widetilde{\psi} = \frac{1}{r_a}\mathrm{SST}$$

This change can be interpreted as follows: The maximum response to SST forcing still occurs when ν is small, but since (as it turns out) the quantity in parentheses above is now greater than 1, the $\widetilde{\psi}$ response will be weaker than in the no-diffusion case. This makes sense, for we expect PV diffusion to weaken the response to forcing. However, and more importantly, since the expression for ν (2.34) contains the complex factor μ, ν contains an imaginary part as well, greatly complicating the analysis.

We now combine this expression with the oceanic response equations, as discussed in Section 2.2.1.2. The dispersion relations (2.42), (2.44), *et cetera* are modified such that the term

$$\frac{\frac{\nu}{\Gamma} + i}{\left(\frac{\nu}{\Gamma}\right)^2 + 1}$$

is transformed into

$$\frac{\frac{\nu}{\Gamma} + i\left(1 + \boxed{\kappa_a^2 \widehat{\chi}/\Gamma - \kappa^2 \widetilde{\chi}\mu/\Gamma}\right)}{\left(\frac{\nu}{\Gamma}\right)^2 + \left(1 + \boxed{\kappa_a^2 \widehat{\chi}/\Gamma - \kappa^2 \widetilde{\chi}\mu/\Gamma}\right)^2}$$

So that, for example, the entrainment-only dispersion relation (2.44) is now

$$\sigma = \omega_r - r\left[\alpha\kappa^2 L_o^2 \left(\frac{\mu}{2} + 1\right) \frac{\frac{\nu}{\Gamma} + i\left(1 + \boxed{\kappa_a^2 \widehat{\chi}/\Gamma - \kappa^2 \widetilde{\chi}\mu/\Gamma}\right)}{\left(\frac{\nu}{\Gamma}\right)^2 + \left(1 + \boxed{\kappa_a^2 \widehat{\chi}/\Gamma - \kappa^2 \widetilde{\chi}\mu/\Gamma}\right)^2}\right] \tag{A.4}$$

One must also remember to use the new definition of μ from equation (A.3). This equation is too complicated to understand intuitively; however, we can still measure the effect of the diffusion parameter by plotting the dispersion relation as in figure 2-8, once we have chosen appropriate values for $\widetilde{\chi}$ and $\widehat{\chi}$.

A.2 Constraints on the values of the diffusion constants

The diffusion constants χ_1 and χ_2 are not arbitrary. Marshall (1981) showed that since eddies only redistribute PV rather than creating or destroying it, the eddy diffusion constants χ_n in a zonally-symmetric, 2-layer QG channel ocean model must obey the relation

$$\int_0^L \left(H_1 \chi_1 \frac{\partial \overline{q}_1}{\partial y} + H_2 \chi_2 \frac{\partial \overline{q}_2}{\partial y} \right) dy = 0 \tag{A.5}$$

where the H_n are the thicknesses of the layers, and $\overline{q}_n$ are the basic-state PV gradients. This relation can be adapted to our 2-level atmospheric pressure-coordinate model: assuming χ_n are uniform within a level, we find that

$$\frac{\chi_1}{\chi_2} = -\frac{\left(\overline{\frac{\partial \overline{q}_2}{\partial y}}^y\right)}{\left(\overline{\frac{\partial \overline{q}_1}{\partial y}}^y\right)}$$

It is clear that both diffusion constants may be chosen to be positive only if the basic-state PV gradients are of different signs in the two layers – that is, if the necessary condition for baroclinic instability in this model (Pedlosky, 1987) is met. This is the case for the model parameters used here (Table 2.1).

We may transform this equation from layer variables to modal variables:

$$\frac{\widehat{\chi}}{\widetilde{\chi}} = -\frac{\widetilde{\beta}}{\widehat{\beta}}$$

where $\widetilde{\beta}$ and $\widehat{\beta}$ are defined in (2.13) and (2.14). For the parameters used in Chapter 2, $\widehat{\chi}/\widetilde{\chi} = -1.15$. We choose $\widehat{\chi}$ positive, which makes χ_n positive in both layers.

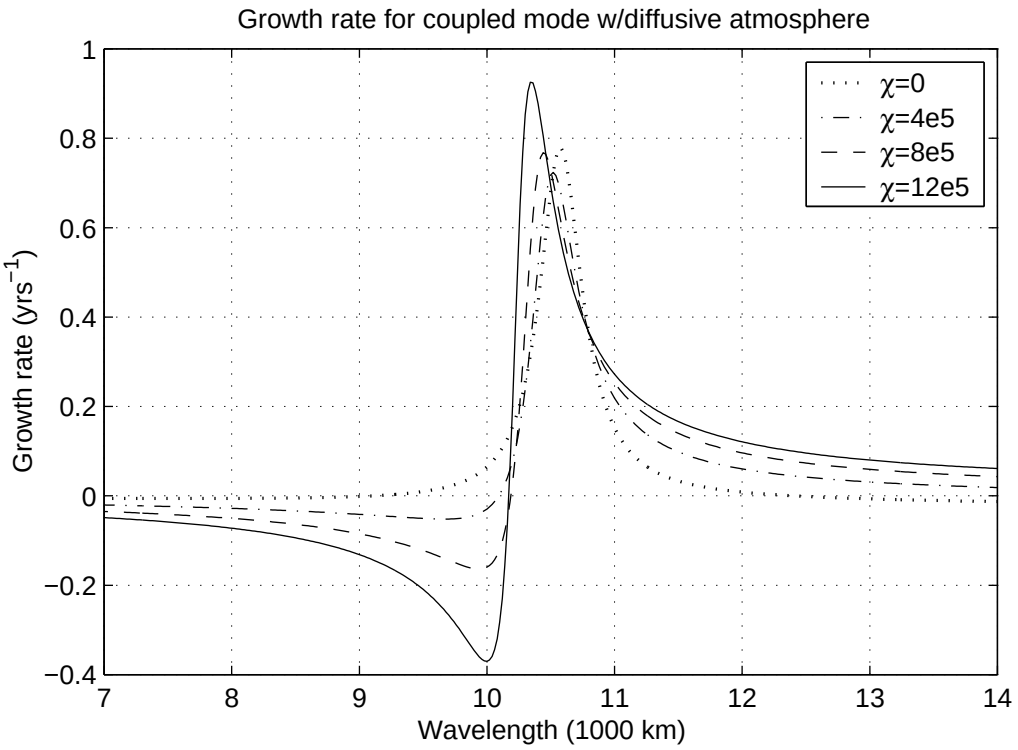

Figure A-1: Growth rate ($Im(\sigma)$) as a function of wavelength for the coupled dispersion relation (A.4), which adds PV diffusion to the model in Chapter 2. Dotted line: barotropic diffusion constant $\widehat{\chi} = 0$; Dash-dotted: $\widehat{\chi} = 4 \cdot 10^5$ m^2/s; Dashed: $\widehat{\chi} = 8 \cdot 10^5$ m^2/s; Solid: $\widehat{\chi} = 1.2 \cdot 10^6$ m^2/s. In all cases, $\widetilde{\chi} = -0.87\widehat{\chi}$.

A.3 Results

Figure A-1 shows the imaginary part of the dispersion relation with PV diffusion included, for the simple "entrainment-only" SST parameterization (A.4). This figure is to be compared with Figure 2-8c. We show the growth rate for values of the barotropic diffusion constant $\widehat{\chi}$ ranging from 0 to $1.2{\cdot}10^6$ m^2/s, and with $\widetilde{\chi} = -0.87\widehat{\chi}$ as constrained by the analysis in Section A.2.

We observe, firstly, that the presence of a diffusive term does not destroy the coupled growing mode. When diffusion is small, the peak in Figure A-1 is shorter and slightly broader, so the coupled mode grows less rapidly, but a wider range of wavelengths will be amplified. Growth is reduced simply because diffusion, as a dissipative process, reduces the atmospheric wave amplitude. Why is the peak broader? We saw in Chapter 2 that coupled growth requires an equilibrated mode

in the atmosphere, for which the advective tendency is smaller than the damping tendency. Diffusion increases the damping tendency, making it easier to satisfy this criterion.

When diffusion is large, the shape of the growth curve changes. The peak growth rate shifts to slightly smaller wavelengths, and wavelengths shorter than 10,000 km undergo coupled damping. Concurrent with this change is a tendency for the coupled mode's atmospheric response to lie upstream of the forcing SST anomaly. For wavelengths smaller than 10,000 km, the atmospheric response is more than 90° out of phase: this leads to negative feedback (see Figure 2-4) and a damped mode. The fact that the fastest-growing mode differs in wavelength by only a few hundred km from a highly damped mode is cause for some concern about the sensitivity of growth rate to small changes in the parameters.

A.4 Conclusion

Generally, we see that the model's coupled behavior is not vastly changed by the addition of eddy PV diffusion. The coupled mode still exhibits a rough phase match between SST forcing and atmospheric response, we still need a nearly-equilibrated atmospheric mode to achieve this phase match, and the wavelength of such a mode is quite similar to the nondiffusive case. The response of a diffusive atmosphere may be somewhat more sensitive to model parameters, but the bulk features of the model described in Chapter 2 still hold.

We have also experimented with adding diffusion to the numerical model of chapter 3. A slight difficulty is presented by the fact that Marshall's relation between the layer diffusion constants (A.5) was derived on the assumption that the mean PV field was zonally-symmetric – this is not always true in our numerical coupled model. However, Marshall's results can be extended to cover zonally-asymmetric flows in our situation, producing a constraint on the χ_n essentially identical to (A.5), allowing the results of this section to be applied to the numerical model.

Appendix B

On the merits of computing EOFs and neutral vectors in restricted domains

In several contexts throughout this thesis, and in conversations with other scientists about preferred atmospheric modes, the subject of the size of the domain of analysis has come up. For example, when computing EOFs, some workers (Cayan, 1992) have chosen to restrict the analyzed data to a single ocean basin, while others (Thomson and Wallace, 1998, Molteni *et al.* , 1988) compute EOFs over hemispheric or global domains. In computing neutral vectors, one could also choose to find patterns which respond most strongly to forcing located over a single ocean basin, or to forcing with a particular vertical structure. In this appendix, we consider the merits of this type of restricted domain.

B.1 EOFs in restricted domains

EOFs of atmospheric variability are very commonly computed over the domain of the North Atlantic or North Pacific (Walker & Bliss, 1932[1], Cayan, 1992). This tends to

[1]Walker and Bliss do not call their technique a regional EOF analysis, but Wallace (2000) shows that it is equivalent to one.

produce traditional features like the NAO and PNA patterns. On the other hand, EOF analyses of the entire northern hemisphere (Wallace and Thomson (1998)) tend to produce the roughly zonally-symmetric, hemisphere-spanning Arctic Oscillation as the leading mode.

Which of these styles of analysis is better? A strong case can be made for either. A global or hemispheric EOF analysis attempts to produce a pattern which maximizes the explained variance over the entire globe or hemisphere. As a result, a globally-computed EOF is at risk of combining several dynamically-unconnected patterns from around the globe, erroneously lumping them together. On the other hand, computing EOFs over a single basin might produce an apparently-local pattern, even if the "true" dynamical mode is global in extent. The standard remedy for this is to regress the locally-computed EOF timeseries over the global domain, to detect global teleconnections if they exist. However, as we will show below, this technique is not always effective in the presence of eddy "noise".

As a demonstration, we construct two mock datasets and perform EOF analyses on them. These datasets are a superposition of one or more well-structured "signals" (analogous to some dynamical mode of the atmosphere) plus some background "noise" (which mimics atmospheric eddies). Both datasets are 300 time units long, and contain 30 spatial points. Both have an identical amount of background noise. This noise is Gaussian in time, but locally correlated in space: the noise is generated by spatial cubic interpolation of 10 independent Gaussian random variables. This is intended to mimic weekly samples of synoptic eddies.

The first dataset contains a signal whose shape is a two-hump "global pattern" given by the dashed line in the first panel of figure B-1. We multiply this pattern by a Gaussian-random amplitude at every time point, and add the noise timeseries. The amplitude of the signal is half that of the noise.

The second dataset consists of two uncorrelated "local" signals, shown as the dashed and dash-dotted lines in the second panel of B-1. The "left signal" has a single hump on the left side of the domain, and is zero on the right, and vice versa for the "right signal". We multiply each by an independent Gaussian-random amplitude,

and add the noise timeseries. Again, each signal has half the amplitude of the noise.

Now we perform two kinds of EOF analysis on each dataset, attempting to extract the signals from the noise. First, we perform a global EOF analysis, in which we find patterns which maximize covariance over the whole domain. Second, we perform a pair of "local" EOF analyses, finding patterns which maximize covariance over the left half and the right half of the domain separately. We regress the amplitude of these patterns upon the whole-domain dataset to recover any teleconnections with areas outside the region where the EOF was computed.

Figure B-1 shows the results. In the top panel, we see that the global EOF analysis easily extracts the global signal from its noisy dataset. Similarly, in the bottom panel, the local EOF analyses easily extracts the local signals from their dataset.

The second panel shows the results of a global EOF analysis on the dataset which contains two uncorrelated local signals. The first two EOFs of the analysis consist of orthogonal superpositions of the two local signals. These two EOFs are global in extent: looking solely at them, one might conclude that there were a pair of global patterns in the data, rather than two local signals.

The third panel shows the results of local EOF analyses on a dataset which contains one global signal. Each EOF analysis picks up the part of the signal within its sector, and indicates almost no correlation with the other half of the domain. Looking at these EOFs, one might conclude that the dataset consisted of a pair of local signals, rather than a single global signal.

So, global EOF analysis can indicate global correlations where none exist, and local EOF analysis can indicate that global correlations do not exist, when they do. It's a paradox reminiscent of the wave-particle duality in quantum mechanics: the behavior observed depends on the measurement technique.

Why does the global EOF analysis indicate global patterns when none exist? When two signals of equal strength are present, the EOF analysis produces a pair of identical eigenvalues λ_1, λ_2. In this situation, there is an ambiguity in the choice of eigenvectors v_1, v_2: any linear superposition of v_1 and v_2 is also an eigenvector. Thus, the EOF analysis finds a mixture of the two true signals. If you believe that

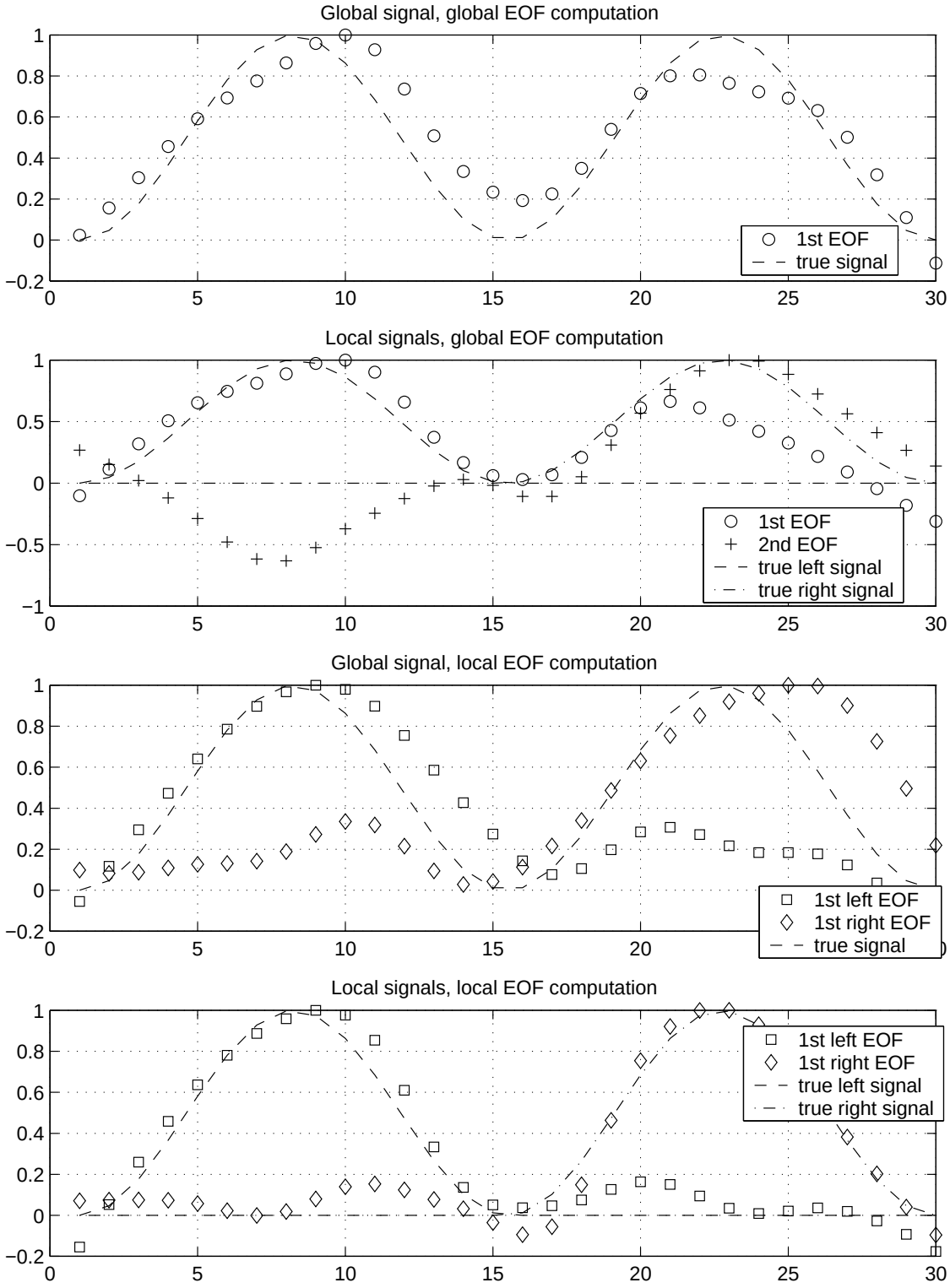

Figure B-1: Results of global and local EOF analyses, performed on noisy artificial datasets containing either one global or two local signals. See text for full explanation.

the patterns are truly local, you can use a "rotated EOF analysis" (Richman, 1986) to separate the signals. (However, note that if you're wrong, and the two signals *are* globally-correlated, rotating the EOFs to produce local patterns is still possible, but misleading.)

Why does the local EOF analysis indicate local patterns when the true signal is global? When the double-bump global signal produces a bump on (say) the left side, there will a bump on the right side too. But when the dataset is noisy, many of the cases where the data has a bump on the left side will be due to the noise, and no bump will occur on the right. These cases tend to reduce the correlation of the left bump with the right bump, lowering the apparent strength of the teleconnection. This effect increases as the signal-to-noise ratio goes down.

Both global and local EOF analyses can mislead one about the existence of teleconnections. But the crucial point is this: with global EOF analyses, *you can tell when you're being misled*. Spurious apparent global teleconnections only occur when the analysis produces two nearly-equal eigenvalues. This indicates that a technique like rotated EOF analysis (Richman, 1986) is called for. In contrast, there's no way to tell when local EOF analysis is spuriously indicating no global teleconnection.[2]

B.2 Neutral vectors in restricted domains

Difficulties also arise in computing neutral vectors within a restricted domain, but for a rather different reason. The following shows what happens if we restrict the computation to a particular vertical mode.

Consider the equation for atmospheric response in the 2-layer model (3.8). For clarity in the following discussion, we take the sum and difference of the upper and lower-layer PV equations, rewriting the system in terms of the barotropic and baroclinic streamfunction, as was done in (2.9) and (2.10). With appropriate changes to the elements of $\mathbf{M}$, the system can be written:

[2]This isn't quite true. One can analyze the correlation between the amplitude timeseries of the left and right EOFs; if a statistically significant correlation exists, the patterns may be dynamically connected. However, this is not generally done.

$$\mathbf{M\Psi} = \left\{ \begin{array}{cc} \mathbf{A} & \mathbf{B} \\ \mathbf{C} & \mathbf{D} \end{array} \right\} \left[\begin{array}{c} \widetilde{\Psi} \\ \widehat{\Psi} \end{array} \right] = \left[\begin{array}{c} \widetilde{\mathbf{f}} \\ \widehat{\mathbf{f}} \end{array} \right]$$

where $\widehat{\mathbf{f}}$ and $\widetilde{\mathbf{f}}$ represent barotropic and baroclinic PV forcing, and the submatrices $\mathbf{A}$, $\mathbf{B}$, $\mathbf{C}$, and $\mathbf{D}$ encapsulate the dependence of each of $\widetilde{\Psi}$ and $\widehat{\Psi}$ on each of $\widetilde{\mathbf{f}}$ and $\widehat{\mathbf{f}}$. If forcing is thermal (from SST), then $\widehat{\mathbf{f}} = 0$.

In section 3.2.2, we looked for the patterns which responded most strongly to *any* forcing, be it barotropic or baroclinic. But since the thermal forcing provided by the model's ocean is purely baroclinic, perhaps it makes sense to maximize the response to *baroclinic only* forcing. That is, perhaps we should minimize

$$\lambda^2 = \frac{\left\langle \widetilde{\mathbf{f}}, \widetilde{\mathbf{f}} \right\rangle}{\langle \mathbf{\Psi}, \mathbf{\Psi} \rangle}$$

It turns out that this is a bad idea. Since $\widetilde{\mathbf{f}} = [\mathbf{AB}]\mathbf{\Psi}$, (B.2) can be rewritten

$$\lambda^2 = \frac{\langle [\mathbf{AB}]\mathbf{\Psi}, [\mathbf{AB}]\mathbf{\Psi} \rangle}{\langle \mathbf{\Psi}, \mathbf{\Psi} \rangle} = \frac{\left\langle \left\{ \begin{array}{cc} \mathbf{A}^2 & \mathbf{AB} \\ \mathbf{BA} & \mathbf{B}^2 \end{array} \right\} \mathbf{\Psi}, \mathbf{\Psi} \right\rangle}{\langle \mathbf{\Psi}, \mathbf{\Psi} \rangle} \tag{B.1}$$

But look what's happened! $\mathbf{C}$ and $\mathbf{D}$ encapsulate the barotropic PV tendency terms of the equation, but they have been eliminated. In choosing to be sensitive only to baroclinic forcing, *we have thrown away the entire barotropic PV equation!* Since the barotropic PV equation is crucial to the coupled mode (most notably in determining the value of μ in (2.32)), the "neutral vectors" of this system are completely unlike the patterns important to atmosphere-ocean coupling. In fact, since the rows and columns of $\left\{ \begin{array}{cc} \mathbf{A}^2 & \mathbf{AB} \\ \mathbf{BA} & \mathbf{B}^2 \end{array} \right\}$ are not linearly independent, half of its eigenvalues are identically zero – the matrix is singular. Even if one throws away the zero singular vectors, the remaining "neutral vectors" are simply the largest modes which fit in the

domain, and do not show the nearly-resonant dynamics discussed earlier.[3]

A different way of looking at this is to say that, since we're sensitive only to baroclinic forcing, we are specifying an particular inner product which gives zero weight to the barotropic forcing component. That is, we minimize

$$\lambda^2 = \frac{\langle \mathbf{M\Psi}, \mathbf{M\Psi} \rangle_S}{\langle \mathbf{\Psi}, \mathbf{\Psi} \rangle} = \frac{\mathbf{\Psi}^\dagger \mathbf{M}^\dagger \mathbf{S} \mathbf{M} \mathbf{\Psi}}{\mathbf{\Psi}^\dagger \mathbf{\Psi}} \tag{B.2}$$

where the weight matrix $\mathbf{S}$ is

$$\mathbf{S} = \left\{ \begin{array}{cc} \mathbf{I} & \mathbf{0} \\ \mathbf{0} & \mathbf{0} \end{array} \right\}$$

You can verify that $\mathbf{M}^\dagger \mathbf{S} \mathbf{M} = [\mathbf{AB}][\mathbf{AB}]^\dagger$, and thus that (B.1) and (B.2) are the same.

But if we choose an inner product which gives the barotropic PV tendency zero weight, then the model can have as large a barotropic tendency as it likes without affecting the tendency norm. Thus, any mode with zero baroclinic tendency and arbitrary barotropic tendency is perfectly "neutral" according to this norm.

The correct way to approach this problem is to treat the barotropic PV equation as a side constraint which restricts the minimization to a certain subspace, rather than as part of the minimization problem itself. However, this is somewhat involved mathematically, and as the point of this appendix is to call attention to problems with restricted analysis rather than to provide complete solutions, we do not present the derivation here.

Similar problems arise when we restrict the neutral vectors geographically. Attempting compute the patterns which respond most strongly to, say, forcing over the Atlantic in Molteni's 3-layer QG model means that we are throwing away all dynamics occurring outside the region of interest. It also means choosing a norm with zero weight outside the Atlantic, so the resulting "neutral vectors" have identically zero tendency/forcing over the Atlantic and arbitrary patterns elsewhere. The "cor-

[3]There are two ways to compute the singular vectors of an N-by-M matrix: by finding the eigenvectors of $\mathbf{M}^\dagger \mathbf{M}$ or of $\mathbf{M}\mathbf{M}^\dagger$. The larger of these matrices will always have $N - M$ identically zero singular values, with the remainder being identical to those of the smaller matrix. Instead of "throwing out" the zero singular vectors, one can just solve the smaller problem. However, this doesn't change the result.

rect way" described in the previous paragraph is now more difficult, because of the more complicated structure of the $\mathbf{M}$ matrix. In addition, since the 3-layer model is spectral, it is difficult to define a geographically-localized inner product. In gridpoint space, we can multiply ψ at each point by a geographically-variable weight, but such a multiplication in gridpoint space equates to a *convolution* in spectral space. The appropriate weight matrix is thus quite complicated.

We have not investigated it in detail, but there are indications that restricting the domain of the *neutral vectors themselves*, rather than their forcing, may also pose problems. If we ask for the forcing pattern which maximizes the response over, say, the Atlantic basin, the problem is not singular in the same way as before. Instead of having modes with $\lambda^2 = 0$ in (3.10) because they have zero tendency except where the weight of the upper inner product is zero, we will have some modes with $\lambda^2 = \infty$ because they have nonzero tendency but zero amplitude where the weight of the lower inner product is nonzero. Another way to look at it is that rather than deleting rows of $\mathbf{M}$, we're deleting columns. The presence of patterns with infinite singular values doesn't mean the problem is impossible (after all, these modes will have *zero* response in the domain of interest to forcing), but the problem is rather difficult.

B.3 Conclusion

We see that computing EOFs or neutral vectors in restricted domains poses many difficulties. When local EOFs are computed, one is at risk of mistaking a truly global pattern for a local phenomenon. When local neutral vectors are computed, problems with singular matrices and deleting important model dynamics arise.

These difficulties may warrant the use of EOF and neutral vector computations on global domains, even when that isn't quite what you want. Globally-computed EOFs risk mistaking two local patterns for two global ones, but this error can easily be detected by noticing the equality of eigenvalues. Globally-computed neutral vectors seem to pose no problems in practice.

Bibliography

[1] U. Achatz and G. Branstator. A two-layer model with empirical linear corrections and reduced order for studies of internal climate variability. *J. Atmos. Sci.*, 56(17):3140–3160, 1999.

[2] T. P. Barnett. Variations in near-global sea level pressure. *J. Atmos. Sci.*, 42:478–501, 1985.

[3] J. J. Barsugli and D. S. Battisti. The basic effects of atmosphere-ocean thermal coupling on midlatitude variability. Submitted to *J. Atmos. Sci.*, 1996.

[4] D. S. Battisti, U. S. Bhatt, and M. A. Alexander. A modeling study of the interannual variability in the wintertime North Atlantic ocean. *J. Climate*, 8:3067–3083, 1995.

[5] G. Branstator. Organization of storm track anomalies by recurring low-frequency circulation anomalies. *J. Atmos. Sci.*, 52(2):207–226, 1995.

[6] G. Branstator. personal communication, 1999.

[7] C.S. Bretherton and D.S. Battisti. An interpretation of the results from atmospheric general circulation models forced by the time history of the observed sea surface temperature distribution. *Geophys. Research Lett.*, 27(6):767–770, 2000.

[8] M. A. Cane, M. Munnich, and S. E. Zebiak. A study of self-excited oscillations of the tropical ocean-atmosphere system, part I: Linear analysis. *J. Atmos. Sci.*, 47(13):1562–1577, 1990.

[9] D. Cayan. (a) latent and sensible heat flux anomalies over the northern oceans: the connection to monthly atmospheric circulation. *J. Climate*, 5:354–369, 1992.

[10] D. Cayan. (b) Latent and sensible heat flux anomalies over the northern oceans: Driving the sea surface temperature. *J. Phys. Oceanog.*, 22:1743–1753, 1992.

[11] J. G. Charney and A. Eliassen. A numerical method for predicting the perturbations of middle latitude westerlies. *Tellus*, 1:38–54, 1949.

[12] M. Christoph and T. P. Barnett. personal communication, 1996.

[13] R. G. Curry and M. S. McCartney. Labrador sea water carries northern climate signal south. *Oceanus*, 39(2):24–28, 1997.

[14] A. Czaja and C. Frankignoul. Influence of the North Atlantic SST on the atmospheric circulation. *Geophys. Research Lett.*, 26(19):2969–2972, 1999.

[15] A. Czaja and J. Marshall. (a) On the interpretation of AGCMs response to prescribed time-varying SST anomalies. *Geophys. Research Lett.*, 27(13):1927–1930, 2000.

[16] A. Czaja and J. Marshall. (b) Observations of atmosphere-ocean coupling in the North Atlantic. *J. Climate*, 2000. Submitted.

[17] F. d'Andrea. personal communication, December 2000.

[18] C. Deser and M. Blackmon. Surface climate variations over the North atlantic ocean during winter: 1900–1989. *J. Climate*, 6:1743–1753, 1993.

[19] R. Dickson, J. Lazier, J. Meincke, and P. Rhines. Long-term coordinated changes in the convective activity of the North Atlantic. In *Decadal climate variability: dynamics and predictability*, volume 44 of *NATO ASI series, Series I: Global Environmental Change*. Springer, 1996.

[20] C. Frankignoul. Sea surface temperature anomalies, planetary waves, and air-sea feedback in the middle latitudes. *Rev. of Geophysics*, 23(4):357–390, 1985.

[21] C. Frankignoul, A. Czaja, and B. L'Heveder. Air-sea feedback in the North Atlantic and surface boundary conditions for ocean models. *J. Climate*, 11:2310–2324, 1998.

[22] C. Frankignoul and K. Hasselman. Stochastic climate models. part II: Applicationto sea surface temperature variability and thermocline variability. *Tellus*, 298(284-305), 1977.

[23] C. Frankignoul, P. Muller, and E. Zorita. A simple model of the decadal response of the ocean to stochastic wind forcing. *J. Phys. Oceanog.*, 27:1533–1546, 1996.

[24] B. Gallego and P. Cessi. Exchange of heat and momentum between the atmosphere and ocean: a minimal model of decadal oscillations. *Climate Dynamics*, 2000. In press.

[25] A. Gill. *Atmosphere-Ocean Dynamics*. Academic Press, 1982.

[26] J. Goodman and J. Marshall. A model of decadal middle-latitude atmosphere-ocean coupled modes. *J. Climate*, 12(2):621–641, 1999.

[27] S. M. Griffies and E. Tziperman. A linear thermohaline oscillator driven by stochastic atmospheric forcing. *J. Climate*, 8:2440–2453, 1995.

[28] T. Haine. Sensitivity analysis of the climate of a chaotic system. *Tellus A*, 52(5):523–532, 2000.

[29] K. Haines and A. Hannachi. Weather regimes in the Pacific from a GCM. *J. Atmos. Sci.*, 52(13):2444–2462, 1995.

[30] N. Hall and S. Manabe. Can local linear stochastic theory explain sea surface temperature and salinity variability? *Climate Dynamics*, 13, 1997.

[31] A. Hannachi. Low-frequency variability in a GCM: Three-dimensional flow regimes and their dynamics. *J. Climate*, 10(6):1357–1379, 1997.

[32] K. Hasselmann. Stochastic climate models. part I: Theory. *Tellus*, 28:473–485, 1976.

[33] J. W. Hurrell. Decadal trends in the North Atlantic Oscillation: Regional temperatures and precipitation. *Science*, 269:676–679, 1995.

[34] J. W. Hurrell and H. van Loon. Decadal variations in climate associated with the North Atlantic oscillation. *Climatic Change*, 36:301–326, 1997.

[35] G. A. Jacobs and J. L. Mitchell. Ocean circulation variations associated with the Antarctic Circumpolar Wave. *Geophys. Research Lett.*, 23(21):2947–2950, 1996.

[36] I. N. James and P. M. James. Ultra-low frequency variability in a simple atmospheric model. *Nature*, pages 53–55, 1989.

[37] A. Kaplan, Y. Kushnir, and M. A. Cane. Reduced space optimal interpolation of historical marine sea level pressure: 1854-1992. *J. Climate*, 13(16):2987–3002, 2000.

[38] M. Keables. Spatial variability of midtropospheric circulation patterns and associated surface climate in the United States during ENSO winters. *Phys. Geography*, 13(4):331–348, 1992.

[39] Y. Kushnir. Interdecadal variations in North Atlantic sea surface temperature and associated atmospheric conditions. *J. Climate*, 7:141–157, 1994.

[40] Y. Kushnir and I. Held. Equilibrium atmospheric response to North Atlantic SST anomalies. *J. Climate*, 9:1208–1219, 1996.

[41] M. Latif. Tropical pacific/atlantic ocean interactions at multi-decadal time scales. *Geophysical Research Letters*, 28:539, 2001.

[42] M. Latif and T. P. Barnett. Causes of decadal climate variability over the North Pacific and North America. *Science*, 266:634–637, 1994.

[43] M. Latif and T. P. Barnett. Decadal climate variability over the North Pacific and North America: dynamics and predictability. *J. Climate*, 9:2407–2423, 1996.

[44] M.A. Latif et al. A mechanism for decadal climate variaility. In *Decadal Climate Variability: Dynamics & Variability*, volume 44 of *NATO ASI series, Series I: Global Environmental Change*, pages 263–292. Springer, 1996.

[45] R.B. Lehoucq, D.C. Sorensen, and C. Yang. *ARPACK Users' Guide: Solution of Large-Scale Eigenvalue Problems with Implicitly Restarted Arnoldi Methods.* SIAM Publications, Philadelphia, 1998.

[46] R. S. Lindzen, E. S. Batten, and J-W. Kim. Oscillation in atmospheres with tops. *Mon. Weather Rev.*, 96:133–140, 1968.

[47] E. N. Lorenz. Climate predictability: The physical basis of climate modeling. In *GARP Pub. Ser.*, volume 16, pages 132–136. WMO, 1975.

[48] J. Marotzke, R. Giering, K. Q. Zang, D. Stammer, and T. Lee. Construction of the adjoint MIT ocean general circulation model and application to Atlantic heat transport sensitivity. *J. Geophysical Research*, 1999.

[49] J. Marshall. On the parameterization of geostrophic eddies in the ocean. *J. Phys. Oceanography*, 11(2):257–271, 1981.

[50] J. Marshall, H. Johnson, and J. Goodman. A study of the interaction of the North Atlantic Oscillation with ocean circulation. *J. Climate*, 2000. In Press.

[51] J Marshall and F. Molteni. Toward a dynamical understanding of planetary-scale flow regimes. *J. Atmos. Sci.*, 50(12):1792–1818, 1993.

[52] J. Marshall and D. K. So. Thermal equilibration of planetary waves. *J. Atmos. Sci.*, 47(8):963–978, 1990.

[53] M. S. McCartney, R. G. Curry, and H. F. Bezdek. North Atlantic's transformation pipeline chills and redistributes subtropical water. *Oceanus*, 39(2):19–23, 1997.

[54] G. Meehl, J. Arblaster, and W. Strand. Global scale decadal climate variability. *Geophys. Research Lett.*, 25:3983–3986, 1998.

[55] P.-R. Michelangeli and R. Vautard. The dynamics of Euro-Atlantic blocking onsets. *Quart. J. Royal Met. Society*, 124:1045–1070, 1998.

[56] F. Molteni. *Towards a dynamical understanding of planetary-scale flow regimes*. PhD thesis, Imperial College, University of London, 1994.

[57] F. Molteni. personal communication, 2000.

[58] F. Molteni, A. Sutera, and N. Tronci. The EOFs of the geopotential eddies at 500 mb in winter and their probability density distributions. *J. Atmos. Sci.*, 45(21):3063–3080, 1988.

[59] J. D. Neelin, M. Latif, and F.-F. Jin. Dynamics of coupled ocean-atmosphere models: the tropical problem. *Ann. Rev. Fluid Mechanics*, 26:617–659, 1994.

[60] T. N. Palmer. Predictability of the atmosphere and oceans: from days to decades. In *Decadal Climate Variability: Dynamics and Predictability*, volume 44 of *NATO ASI series, Series I: Global Environmental Change*. Springer, 1996.

[61] T.N. Palmer and Z. Sun. A modelling and observational study of the relationship between sea surface temperature in the north-west Atlantic and the atmospheric general circulation. *Quart. J. Royal Met. Society*, 111:947–975, 1985.

[62] R. L. Panetta, I. M. Held, and R. T. Pierrehumbert. External Rossby waves in the 2-layer model. *J. Atmos. Sci.*, 44(20):2924–2933, 1987.

[63] J. Pedlosky. The development of thermal anomalies in a coupled ocean-atmospheric model. *J. Atmos. Sci.*, 32:1501–1514, 1975.

[64] J. Pedlosky. *Geophysical Fluid Dynamics*. Springer-Verlag, 1987.

[65] B. Qiu and F.-F. Jin. Antarctic Circumpolar Waves: an indication of ocean-atmosphere coupling in the extratropics. *Geophys. Research Lett.*, 24(21):2585–2588, 1997.

[66] M. B. Richman. Rotation of principal components. *J. Climatology*, 6(3):293–335, 1986.

[67] M. J. Rodwell, D. P. Rowell, and C. K. Folland. Oceanic forcing of the wintertime North Atlantic Oscillation and European climate. *Nature*, 398(6725):320–323, 1999.

[68] R. Saravanan and J. C. McWilliams. Stochasticity and spatial resonance in interdecadal climate fluctuations. *J. Climate*, 10:2299–2320, 1997.

[69] R. Saravanan and J. C. McWilliams. Advective ocean-atmosphere interaction: an analytical stochastic model with implications for decadal variability. *J. Climate*, 11(2):165–188, 1998.

[70] G. Shutts. Some comments on the concept of thermal forcing. *Quart. J. Royal Met. Society*, 113:1387–1394, 1987.

[71] J. Smagorinsky. The dynamical influence of large-scale heat sources and sinks on the quasi-stationary mean motion of the atmosphere. *Quart. J. Royal Met. Society*, 97:342–366, 1953.

[72] H. Stommel. The westward intensification of wind-driven ocean currents. *Transactions of the American Geophysical Union*, 99:202–206, 1948.

[73] R. T. Sutton and M. R. Allen. Decadal predictability of North Atlantic sea surface tempe rature and climate. *Nature*, 338:563–566, 1997.

[74] D. W. J. Thompson and J. M. Wallace. The Arctic Oscillation signature in the wintertime geopotential height and temperature fields. *Geophys. Research Lett.*, 25(9):1297–1300, 1998.

[75] G. Walker and E. Bliss. World weather v. *Mem. R. Meteorol. Soc.*, 4:53–83, 1932.

[76] J. M. Wallace. North Atlantic Oscillation/annular mode: Two paradigms – one phenomenon. *Quart. J. Royal Met. Society*, 126(564):791–805, 2000.

[77] J. M. Wallace and D. S. Gutzler. Teleconnections in the geopotential height field during the northern hemisphere winter. *Mon. Weather Rev.*, 109:784–812, 1981.

[78] W. Weng and J. D. Neelin. On the role of ocean-atmosphere interaction in midlatitude interdecadal variability. *Geophys. Research Lett.*, 25:167–170, 1998.

[79] W. White and D. Cayan. Quasi-periodic and global symmetries in interdecadal upper ocean temperature variability. *J. Geophysical Research*, 103:21335–21354, 1998.

[80] W. B. White and T. P. Barnett. A servomechanism in the ocean/atmosphere system of the mid-latitude North Pacific. *J. Phys. Oceanog.*, pages 372–381, 1972.

[81] W. B. White and R. G. Peterson. An Antarctic circumpolar wave in surface pressure, wind, temperature and sea-ice extent. *Nature*, 380:699–702, 1996.